Theses and Dissertations   Student Graduate Works

3-24-2016

Position and Volume Estimation of Atmospheric Nuclear Detonations from Video Reconstruction

Daniel T. Schmitt

POSITION AND VOLUME ESTIMATION
OF
ATMOSPHERIC NUCLEAR DETONATIONS
FROM
VIDEO RECONSTRUCTION

DISSERTATION

Daniel T. Schmitt, Lt Col, USAF

AFIT-ENG-DS-16-M-254

DEPARTMENT OF THE AIR FORCE
AIR UNIVERSITY

AIR FORCE INSTITUTE OF TECHNOLOGY

Wright-Patterson Air Force Base, Ohio

DISTRIBUTION STATEMENT A
APPROVED FOR PUBLIC RELEASE; DISTRIBUTION UNLIMITED.

AFIT-ENG-DS-16-M-254

POSITION AND VOLUME ESTIMATION OF ATMOSPHERIC NUCLEAR
DETONATIONS FROM VIDEO RECONSTRUCTION

DISSERTATION

Presented to the Faculty

Graduate School of Engineering and Management

Air Force Institute of Technology

Air University

Air Education and Training Command

in Partial Fulfillment of the Requirements for the

Degree of Doctor of Philosophy

Daniel T. Schmitt, B.S.C.S., M.S.C.S.

Lt Col, USAF

24 March 2016

AFIT-ENG-DS-16-M-254

POSITION AND VOLUME ESTIMATION OF ATMOSPHERIC NUCLEAR

DETONATIONS FROM VIDEO RECONSTRUCTION

DISSERTATION

Daniel T. Schmitt, B.S.C.S., M.S.C.S.
Lt Col, USAF

Committee Membership:

Prof. Gilbert L. Peterson, PhD
Chairman

John W. McClory, PhD
Member

Maj Brian G. Woolley, PhD
Member

Adedeji B. Badiru, PhD
Dean, Graduate School of Engineering and Management

AFIT-ENG-DS-16-M-254

Abstract

Recent work in digitizing films of foundational atmospheric nuclear detonations from the 1950s provides an opportunity to perform deeper analysis on these historical tests. This work leverages multi-view geometry and computer vision techniques to provide an automated means to perform three-dimensional analysis of the blasts for several points in time. The accomplishment of this requires careful alignment of the films in time, detection of features in the images, matching of features, and multi-view reconstruction. Sub-explosion features can be detected with a 67% hit rate and 22% false alarm rate. Hotspot features can be detected with a 71.95% hit rate, 86.03% precision and a 0.015% false positive rate. Detected hotspots are matched across 57-109° viewpoints with 76.63% average correct matching by defining their location relative to the center of the explosion, rotating them to the alternative viewpoint, and matching them collectively. When 3D reconstruction is applied to the hotspot matching it completes an automated process that has been used to create 168 3D point clouds with 31.6 points per reconstruction with each point having an accuracy of 0.62 meters with 0.35, 0.24, and 0.34 meters of accuracy in the x-, y- and z-direction respectively. As a demonstration of using the point clouds for analysis, volumes are estimated and shown to be consistent with radius-based models and in some cases improve on the level of uncertainty in the yield calculation.

iv

Acknowledgements

I would like to thank my advisor Dr. Bert Peterson for his insight and advice. I would like to thank my co-worker Capt Rob Slaughter for his willingness to answer endless questions on the nuclear domain. I would also like to thank my committee, Dr. McClory and Maj Woolley for their help, influence and guidance. Lastly, I would like to thank my wife for her ability to understand and cope with having a husband that has so many demands on his time.

Daniel T. Schmitt

Table of Contents

List of Figures

List of Tables

POSITION AND VOLUME ESTIMATION OF ATMOSPHERIC NUCLEAR DETONATIONS FROM VIDEO RECONSTRUCTION

I. Introduction

From 1945-1962 the United States conducted a total of 216 atmospheric, underwater, and space nuclear detonation tests (Table 1). Atmospheric testing was then banned following the signing of the Limited Test Ban Treaty. As a result much of the data on atmospheric nuclear weapons effects was produced during this 17 year period of testing.

During testing approximately 9,000 scientific films were recorded of the atmospheric nuclear tests. The films were captured using several cameras by Edgerton, Germeshausen & Grier, Inc. (EG&G) using 8mm, 16mm, and 35mm film. The focus of the filming was to capture early fireball growth, early plume rise, and the late plume following detonation.

Each explosion site was carefully documented (Fig. 1) with multiple film collection sites at defined locations around the explosion. Fig. 2 shows an example of one detonation to demonstrate the relationship between the collection sites and the explosion sites. In this example, there was also a third collection site not pictured that was about 7° off the angle of the 7-357 station about three times the distance away. Each collection site was outfitted with multiple film reels to record the explosions (Fig. 3). For each explosion, the number of collection sites ranged from three to ten. The end result was that there were about 20 high-speed videos recorded for each explosion, some from the same point of view, some with small angular differences of around 10° and others of larger angular differences greater than 60°.

Table 1.   Overview of U.S. Atmospheric Nuclear Testing.

Test Series	Year	Number of Tests
Project Trinity	1945	1
Operation Crossroads	1946	2
Operation Sandstone	1948	3
Operation Ranger	1951	5
Operation Greenhouse	1951	4
Operation Buster-Jangle	1951	7
Operation Tumbler-Snapper	1952	8
Operation Ivy	1952	2
Operation Upshot-Knothole	1953	11
Operation Castle	1954	6
Operation Teapot	1955	14
Operation Wigwam	1955	1
Operation Redwing	1956	17
Operation Plumbbob	1957	24
Operation Hardtack I	1958	34
Operation Argus	1958	3
Operation Hardtack II	1958	19
Operation Dominic I	1962	36
Operation Dominic II	1962	4
Plowshare Program	1961-1962	27

The cameras that were used for the fireball films were the Eastman High Speed Camera and the Fastax [32] shown in Fig. 4. These cameras used a rotating prism (Fig. 5) in order to capture the images on film. Rotating prism cameras have film that moves through the shutter at the same rate that the prism rotates. The film reel and the rotating prism are mechanically linked so that the image moves with the film regardless of the film speed. The result is that one frame of film is produced during each one-half prism rotation creating an exposure time per frame that is the reciprocal of the frame per second rate of the camera [32]. The main disadvantages of using the rotating prism camera is that the camera was not synchronized to the time of detonation which makes the exact time of detonation difficult to determine from analyzing the films. Any process that analyzes the films must be able to synchronize the different films together.

SURVEY DATA

STA.	COORDINATES			FROM T-9B			DIST. HOR.		TANGENTS		ANGLES	
	N	E	Z	ΔN	ΔE	ΔZ*	FT.	M.	ΔN/ΔE	ΔZ/DIST.*	BRG	TILT*
T-9B	865221	680506	4210 +308									
2-365 Truck I / 7-357	863879	668771	4287 +3	-1342	-11755	-228	11811	3600	0.114360	-0.01930	263°18'34"	-1°-06'
7-357 Trailer II / 7-357	853109	677969	4149 +3	-12112	-2537	-366	12375	3772	4.77414	-0.02958	191-49-49	-0-42
6x6 III	853101	677981	4149 +3	-12120	-2525	-366	12380	3773	4.80000	-0.02956	191-46-10	-0-42
372	795955	674471	4798 +3	-69266	-6535	+283	69487	21180	12.51418	+0.00407	184-34-07	+0-14
9.4a CHR's	572728	821735	8084 +4	-292493	+141229	+4370	324800	99000	-2.07105	+0.01345	154-13-36	+0-46
9.4b AM'G'A	594671	566126	2158 +4	-270550	-114380	-2356	293730	89530	2.36536	-0.003021	202-55-02	-0-28
* FROM HEIGHT OF BURST												

FORM E17(1-55 500) NAME BJB EDGERTON, GERMESHAUSEN & GRIER INC.

Figure 1. An example of survey data collected for Tesla [30].

Furthermore, the filming reels that captured the explosions had a variety of collection speeds. One type of camera that was focused on photographing the fireball's growth over time was set at a nominal 2,500 frames per second, however its actual speed varies from 2,100-3,300 frames per second throughout the explosion. To assist the analysis of the videos, a timing system was used that pulsed a small element of light on the film exposing a portion of the film at 5 ms intervals producing a small, circular exposure in the edge of the video frame that are referred to as timing marks. These timing marks occur at regular time intervals, resulting in a varying number of frames between timing marks, and different locations where the marks appear on the film caused by the varying speed of the camera. An example of a timing mark is shown in Fig. 6. These timing marks can be used to correlate an image's actual speed during the frames in question. Unfortunately, however the timing marks are
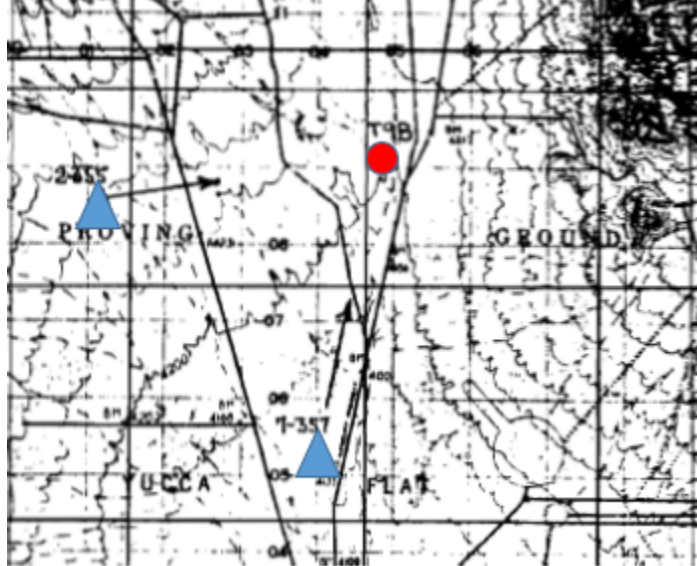
Figure 2. Map of Tesla explosion [30]. The red circle is the detonation site and the blue triangles are film collection sites.

not correlated from one film to another.

Dr. Greg Springs of Lawrence Livermore National Laboratories (LLNL) has digitally scanned many of the films with the goal of making exact digital copies of the original negatives. To accomplish this LLNL uses a Goldeneye Film Scanner developed by Image Systems AB and Digital Vision (Fig. 7). This scanning process is a key enabler that allows us to interact with the films and analyze them using computers.

1.1 Motivation

One motivation for studying the three-dimensional interaction of nuclear detonations is to improve upon the ability to estimate the yield. The detonation's yield corresponds to weapon design and fissile material constituents, and further relates the material to known enrichment capabilities of nations. Accurate yield determination of a detonation potentially helps to determine the nuclear material's source.

Estimating the yield solely from a one-dimensional radius suffers from the ability
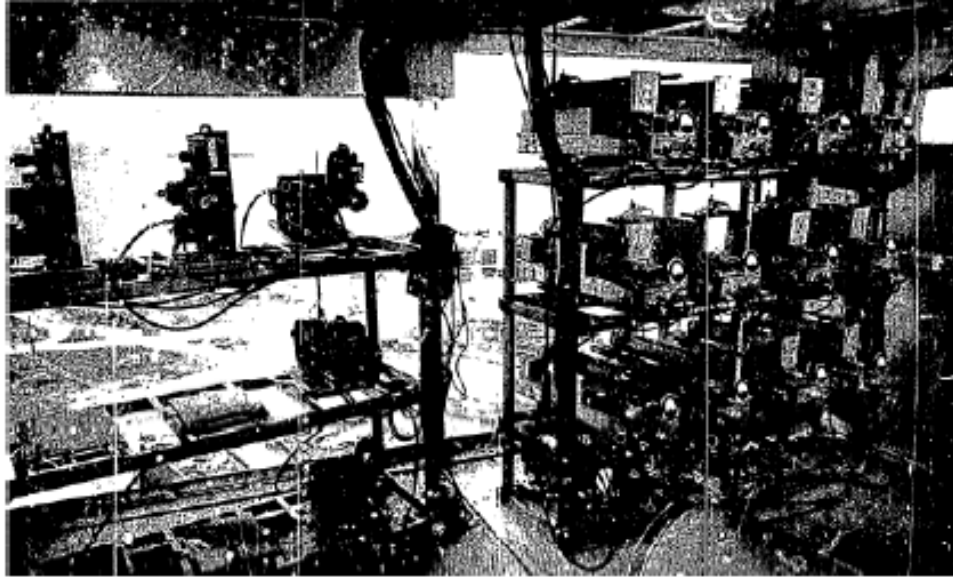
Figure 3. A typical arrangement of cameras within a collection site [30].
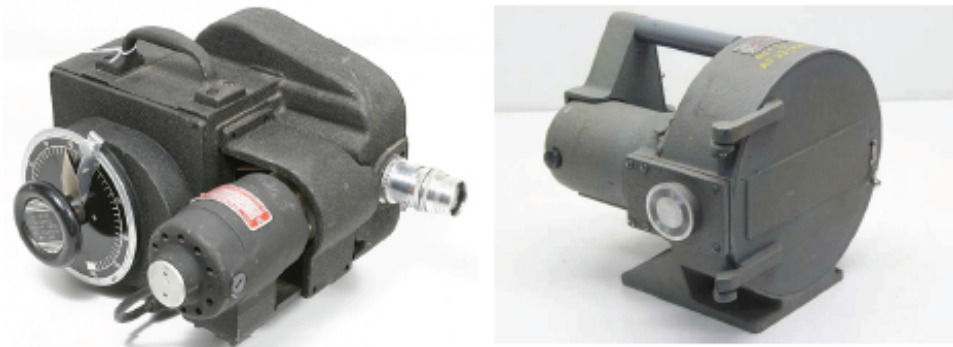
Figure 4. On left is the Eastman High Speed Camera. On right is the Fastax camera [32].

to accurately determine the radius of a non-uniform expansion, thus resulting in high uncertainty. Eq. 1 shows Taylor's equation [36] where R represents the radius, t is the time since detonation, and ρ_0 is the density of the medium. Any uncertainty in measuring R will compound by a factor of 5 when estimating the yield. Substituting the equation of the volume of a sphere $V = \frac{4\pi}{3}r^3$ and solving for r builds Eq. 2. Presuming that a volume could be generated with similar uncertainty to that of a radius, Eq. 2 demonstrates that uncertainty in the volume of the equation lead to an uncertainty of yield by a factor of 5/3 instead of one generated from a radius with

5
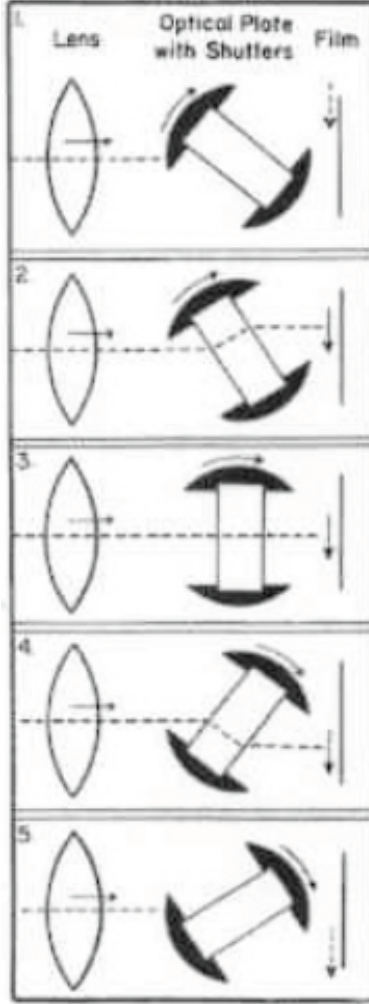
Figure 5. The operation of a rotating prism camera [32].

an uncertainty factor of 5. The error in estimating the yield of a nuclear detonation can be reduced significantly by transitioning from a radius-based model [36] to a volume-based model.

$$Yield \sim \frac{R^5 \rho_0}{t^2} \qquad (1)$$

$$Yield \sim \frac{V^{\frac{5}{3}} \rho_0}{t^2} \qquad (2)$$

In addition to yield estimation, modeling nuclear detonations with 3D representations opens the door to studies that could improve weapons effects, and contribute
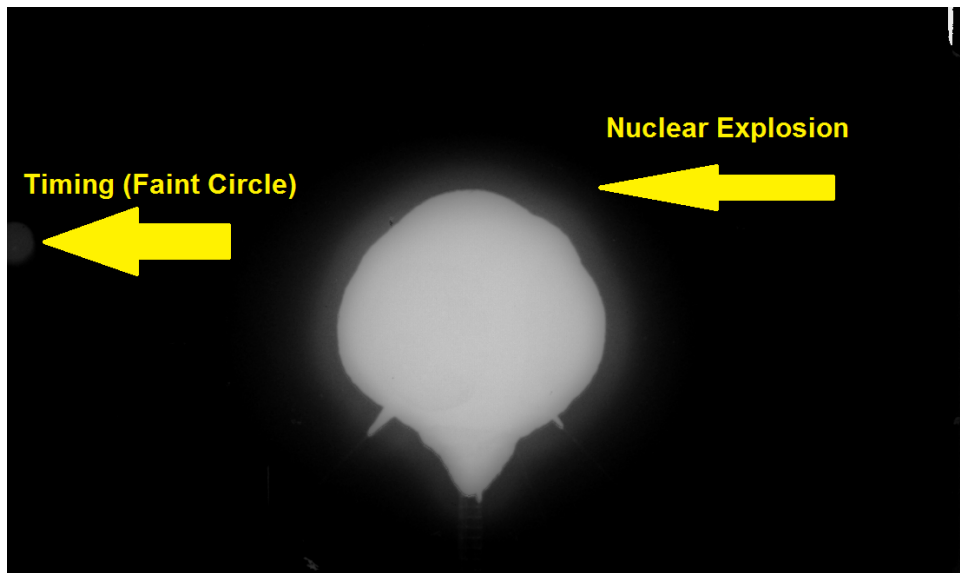
Figure 6. An example timing mark.

Figure 7. The Goldeneye scanner that is used by LLNL to digitize the NUDET films [30].

to defenses against asymmetric nuclear threats.

1.2   Hypothesis

The hypothesis of this work is that multi-view geometry and computer vision techniques can be used to determine 3D points on the NUDETs over time and improve the dimensionality of data available for study. Evaluation of the hypothesis will require the discovery and detection of NUDET image features and a means to perform wide-baseline viewpoint computer vision matching. The result will be an automated, repeatable process that generates 3D point clouds for multiple detonations at multiple points in time with a known accuracy. The 3D point clouds, and other computer vision techniques will then be used to estimate NUDET volumes and demonstrate if the uncertainty of radius-based yield estimates can be improved with 3D reconstruction.

1.3   Research Goal

The primary goal of this research is to provide an automated means to perform three-dimensional analysis for the nuclear detonation (NUDET) films. Almost all nuclear diagnostic information has depended on single-dimensional, radius-based analysis [40] as the basis for its scientific guidance towards the capabilities of the nuclear Department of Defense (DoD) mission. As warfare evolves and the United States looks to address the threat of terrorism, an improvement in the dimensionality of data available can answer questions that analysis to date has been unable to address.

This work aims to accomplish this through careful alignment of the films in time, detection of features in the images, matching of features, and multi-view reconstruction.

1.4   Challenges

There are several challenges to creating a three-dimensional reconstruction of a nuclear detonation. There are challenges in timing, detecting features, matching features, and determining the accuracy of 3D reconstructions. Each of these are discussed in turn.

Timing.

The films have uncertainty with regard to timing as a result of the mechanical nature of the cameras. While the time between timing marks is consistent at 5 msec, each frame is recorded every 0.25 - 0.5 msec. The resulting gaps of 10-15 frames between timing marks leave room for error than is not measurable. Analyzing the changing speed of the camera enables the determination of how the speed of the camera changes over several timing marks, but is unable to determine what happens between timing marks. This means that frame-to-frame there are potential timing inaccuracies relating to the mechanical cameras that cannot be modeled perfectly. These timing inconsistencies compound when frames from multiple films are compared. Ideally, for three-dimensional reconstructions to be accurate, they need to be derived from frames at exactly the same time, or the error in time will translate into a positional error.

To create a three-dimensional reconstruction requires at least two points of view of the object at the same point in time. Unfortunately, in the case of the NUDET domain, the object's shape is changing rapidly, and the timing is not accurate enough to align multiple films together. Furthermore, with the relative speeds of cameras being different, frames within a film fall in and out of time alignment when compared one to another. The end result is that some frame-to-frame comparisons across viewpoints are better than others with respect to time alignment. The process to address

these timing challenges is discussed in Chapter II.

Feature Detection.

Another challenge with the films is the detection of features that could be correlated across films and used either for 3D reconstruction or volume estimation. There are variations of the manner of which films reacted to the detonations causing a variety of brightness and contrast from film to film. Also, within a given film, the light level changes as the detonation develops. Despite these lighting changes, the naked eye can detect areas of interest that can be correlated across viewpoints. Two features are notable by the naked eye that will be referred to as 'subspheres' and 'hotspots.'

Subspheres (Fig. 8) are features that are present in detonations that have obstructions that interact with the shockwave of the detonation. Improvements in volume estimation could be achieved by detecting and estimating the size of these larger deformities. Chapter III discusses the automated detection of subsphere features.

Hotspots are features that are visible in most detonations during a stage in the detonation when the light emitted by the fireball is relatively low. Shown in Fig. 9, they exist all over the outside boundary of the detonation and are visible from different viewpoints. Hotspot features have the potential to be matched from alternate viewpoints in order to enable 3D reconstruction. The detection of hotspots is discussed in Chapter IV.

Algorithm viewpoint matching limitations.

Another challenge is that the best feature descriptors and algorithms are limited on how repeatable their matching algorithms are from wide viewpoints. For example, one popular multi-view geometry (MVG) method uses Scale-Invariant Feature Transform (SIFT) [15] feature detection and matching [29]. These algorithms perform well when
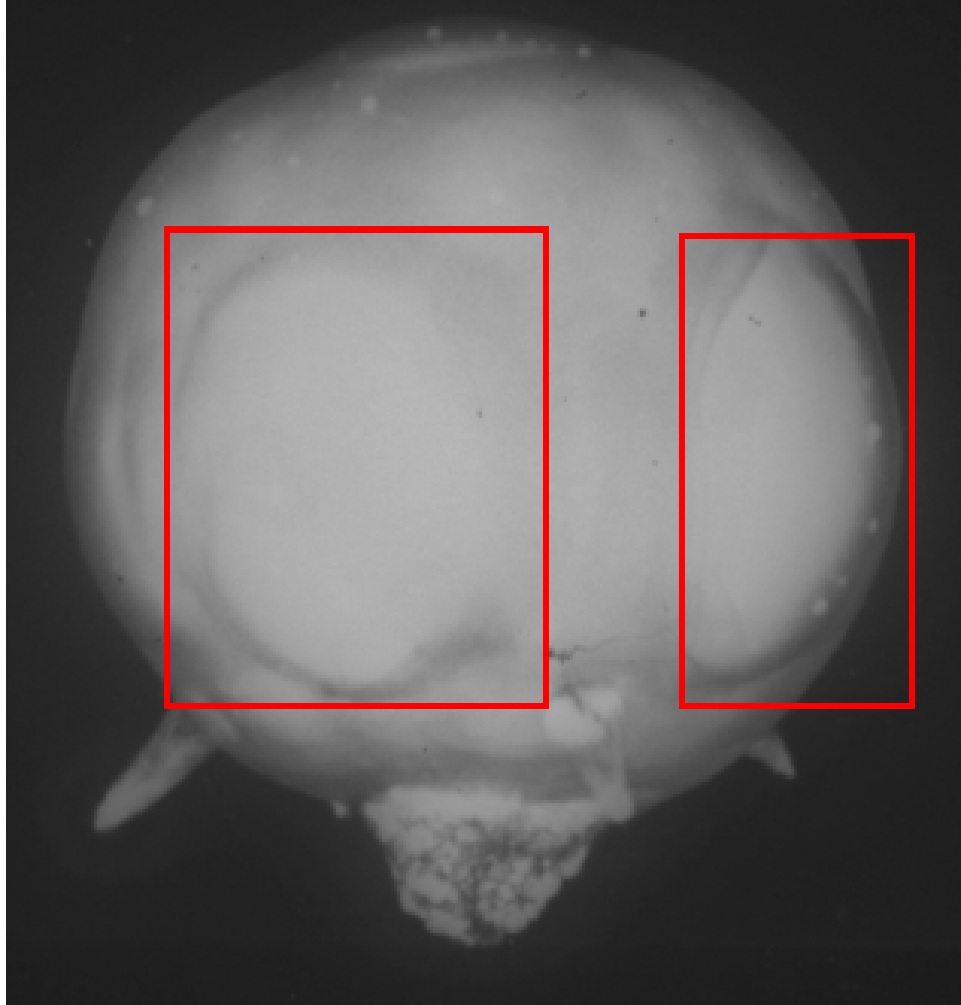
Figure 8. Tesla explosion [30] with two subspheres identified.

viewpoint angles are less than 45°, and preferably less than 20°. Unfortunately, in the NUDET films only a few viewpoints were recorded for each detonation and the viewpoints have wide viewpoint angles of greater than 45° that are outside the documented capabilities of SIFT's match repeatability) [15]. This means that features either need to be matched manually, or an automated technique needs to be developed that works effectively with wide viewpoint angles. Chapter V deals with this challenge by defining an automated feature descriptor and matching algorithm that works at larger viewpoint angles.
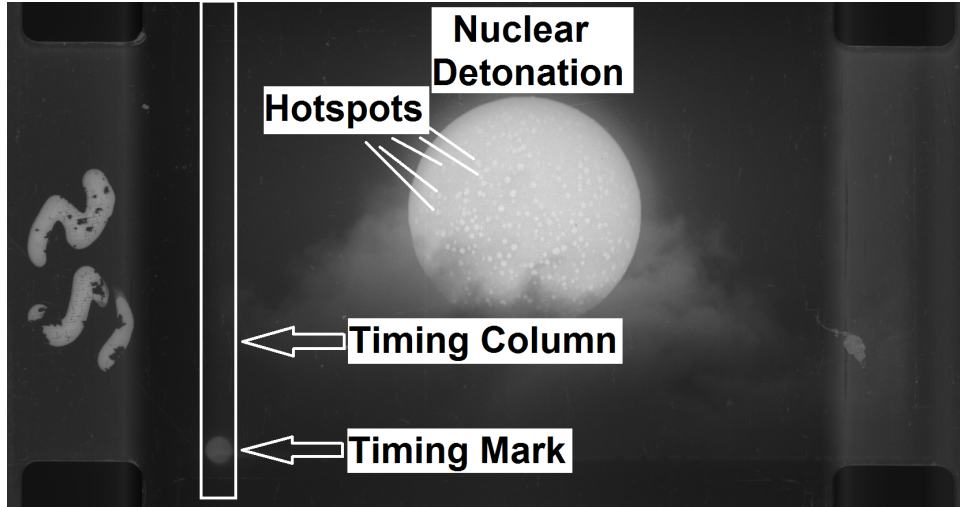
Figure 9. Grable nuclear detonation [30] with some "hotspots" identified. Also identified is a timing mark used to measure time in the variable high-speed cameras.

Determining the accuracy of reconstructions.

Another challenge is there is no positional ground truth information for the detonations for any point in time during the detonation. There was no global positioning system. Locations were manually recorded using Universal Transverse Mercator (UTM) System within a foot's accuracy based on human interpretation of maps. In addition, locations of film collection sites did not have specifics on where specific cameras were located within a collection site. Locations of cameras within a collection site can only be guessed at based on available information like the camera arrangement photo shown in Fig. 3. As far as the subjects within the films, the best ground truth is derived from fixed structures within the view of cameras when those structures exist. This challenge is addressed in Chapter VI by using fixed structures to estimate the accuracy of reconstruction and applying it to points on the detonation.

1.5   Contributions

This document proposes the following contributions to the scientific community.

- The production of 3D sparse point clouds to track and study features of detonations over time.

- An automated process to detect and match hotspot features across wide viewpoints.

The novelty of the first contribution is that there are currently no scale 3D reconstructions of NUDETs. Understanding the second contribution, hotspot matching, requires some background on the state-of-the-art computer vision techniques.

Scale 3D reconstructions require either calibrated cameras as in the case with multi-view stereo (MVS) [27] or require matched correspondences on features between multiple viewpoints to generate 3D point clouds. The NUDET films do not provide camera calibration models, thus making direct use of MVS unreliable. Hence, novel methods will be required to successfully evaluate this problem domain.

SIFT [15] feature matching ,and likewise Speeded-Up Robust Features (SURF) [2], have been used for uncalibrated images [29] however, it has challenges for feature matching with the NUDET films. Only a few viewpoints were recorded for each detonation and the viewpoints have wide viewpoint angles ranging from 58° to 110°, which are outside the documented capabilities of SIFT's viewpoint match repeatability [15]. Methods such as Affine-Invariant SIFT (ASIFT) [18] that extend the viewpoint angles for SIFT up to 90° exist, but ASIFT requires planar surfaces with detectable Harris corners [7] that do not exist in the NUDET films, thus making the algorithm inappropriate for this domain. Manual matching is a viable option and is demonstrated in Chapter VI, but it is cumbersome for such an extensive data set. Because of these issues, a feature descriptor and matching algorithm capable of matching features with wide viewpoint angles (i.e 58° to 110°) without the use of Harris corners is a contribution not only to the physics community, but the computer vision community as well.

1.6 System Overview

The overall goal is to create a reliable and repeatable process to generate 3D point clouds of NUDET features and use those features as a basis for volumetric reconstructionss of detonations using the films. Fig. 10 shows a flow of the information as it is processed from images to 3D reconstruction and volume estimation. The process begins at the left with a sequence of images for each camera. Using the sequence and timing mark detection (Chapter II) images are tagged with the time and possible timing error. They are organized and matched by point of view identifying complete sets of cameras that cover all possible points of view that are also best aligned in time. Because each camera film speed is different and changes over time, there are periods that the time overlap is better than others. Once images are time aligned, subsphere (Chapter III) and hotspot features (Chapter IV) are detected. Hotspot features are used to create correspondence matches between images that form the basis for 3D reconstruction (Chapter V). Accuracy of approximation can be determined by the method used to generate the 3D reconstruction (Chapter VI). Lastly, the subspheres and 3D sparse point clouds can be used to estimate the volume of the detonation (Chapter VII).
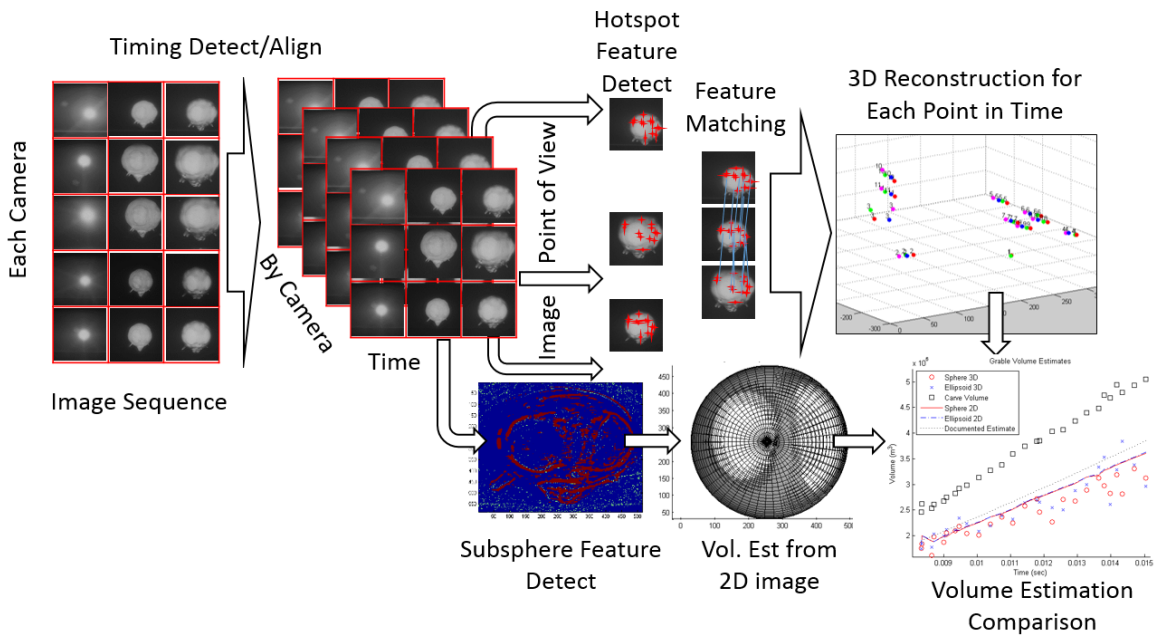
Figure 10. An flow diagram of processing NUDET images into volume estimation.

II. Timing Detection and Timestamp Estimation

Processing images toward 3D reconstruction requires images that have been captured close in time or of a static environment [8]. It is essential that timing is done correctly so that the images can be compared at the same points in time. If images were compared at different points in time, results would induce unrealistic and inaccurate reconstructions.

Timing detection begins with a sequence of images that are known to have timing marks as shown in Fig. 6. With the knowledge that each timing mark is 5 msec apart, the timing marks can be automatically detected in the images and their location within the films can be modeled mathematically to determine their time relative to the start of the detonation. This material appears in the Institute of Electrical and Electronics Engineers (IEEE) Computer Society's Proceedings for the 43rd Applied Imagery Pattern Recognition Workshop [24].

This chapter is organized as follows. First, a block diagram of a Nuclear Video Timing Detector is discussed in Sec. 2.1. Next, the image processing approaches that were applied are discussed in Sec. 2.2. The results of detecting timing marks are presented in Sec. 2.3 and those results are applied to determine timestamps for images in the films in Sec. 2.4. The chapter closes with conclusions regarding timing in Sec. 2.5.

2.1   Block diagram of NUDET Timing detector

Fig. 11 shows the block diagram for the Nuclear Video Timing Detector. Along the left is the input of the sequence of images representing the video. Inside is a computer running the detection algorithm. Along the top are the parameters that are discussed in Section 2.2. The outputs coming out of the right side of the diagram include
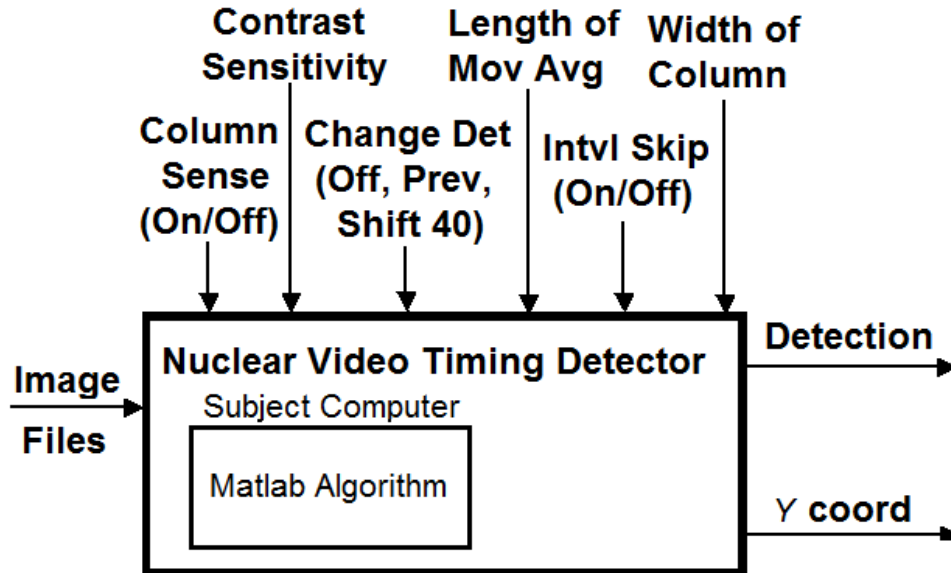
Figure 11. NUDET Timing detector Block Diagram.

whether a detection has occurred on a particular frame, the y-coordinate location of where that detection is in the frame, and the interval from the last successful detection.

2.2   Description of approaches

To accomplish the timing detection, two major approaches are used which are called Column Sum and Circle Detection. Some algorithms also used a Change Detection approach to maximize the detection rate. Some features were also added including sensing the timing column and skipping images based on predicted intervals. Each of these approaches and subapproaches will be described in detail.

Column Sum.

The column sum approach takes advantage of the fact that the timing marks are expected to be repeated in the same vertical column. The existence of a timing mark in the column should raise the overall pixel values of that column. The difference in

17

the amount of additional pixel value could be used as the discriminator to distinguish frames that have timing marks from frames that do not. Timing marks are about 40-60 pixels wide and need to be reduced to one number that is used to determine if it is in the acceptable range (a timing mark without a frame), or out of the acceptable range (a timing mark in a frame). Equation 3 shows how to arrive at the overall pixel indicator value (V) from an M row, for a column that is assumed to be 40 pixels wide that has a pixel value at row m, column n of $\mathbf{S}(m, n)$.

$$V = \frac{1}{40} \times \sum_{n=1}^{40} \sum_{m=1}^{M} \mathbf{S}(m, n) \tag{3}$$

With an pictorial example of a timing mark and column in Fig. 9, the results of Eq. (3) are the sum total of all the pixel values in the timing column divided by the width of the column. One shortfall of this approach is that the timing lane needs to be determined ahead of time. Initially this was done with human intervention, however column sensing discusses an automated approach to this. Now that we have a value to measure the overall light in a column, an approach must be defined for a threshold to determine if that value is a detection of a timing mark or not.

Relative vs Global Thresholds.

Initially it was believed that an average of all the pixel sums could be used as a baseline for a non-detection, and a certain distance (i.e. 2 standard deviations) away from it might indicate a detection. This global threshold worked well for the first few detections, but once the explosion occurred, the explosion influenced the pixel values in the timing lane. Additionally, the light from the explosion would go up and down throughout the explosion further complicating detection. A local average needed to be established that could improve detection rates.

A relative threshold would be a moving average that "forgets" information that

18

is too far away from it. It might be an average and standard deviation of the last 25 frames. This would allow the overall baseline to adjust more quickly while still being representative of the overall average pixel sum.

Circle Detection.

The second major approach for detecting the timing marks is to leverage the fact that their expected shape is a circle. A Hough transform [4] might be able to detect the circles. Sometimes the circles are faint and the image contrast can be adjusted so that the boundaries of the circle are more pronounced. Furthermore, once the region of the timing column is detected, the region that circles are searched for can be reduced from the entire image to just the timing column.

Through preliminary testing, it was discovered that the width of the timing column has an impact on the sensitivity of the circle detection. It might be thought that restricting the image to the smallest column possible would be most beneficial as to avoid false detections out of the column. However, the timing column needs to be wide enough to contain enough of the edges of the circle for the Hough transform [4] to detect. Through testing it was determined that the sweet spot for the 40 pixel diameter timing marks was between 40 and 60 pixels.

Column Sensing.

The column sensing feature uses a Hough transform [4] to detect the circle of expected size and restricts the search region based on that detection rather than requiring human intervention. This feature is sensitive to false detections. If the first circle of correct size is not a timing mark, then the region is restricted incorrectly resulting in the processing missing detections in the entire video.

Change Image.

Another approach that can be combined with either Circle Detection or Column Sum is to use a change image. By subtracting two images pixel by pixel, the changes are more pronounced with the hope being that they are easier to detect.

Change from previous image.

Deriving a change image using the previous image is one change image approach. At the slowest executed frame rates for the high-speed films the timing marks are never less than 5 frames away, so a change image will still preserve the timing mark. The change image will also reduce the effect that gradual ambient light has on the overall bias of pixel sum. Lastly, a change from the previous image can help reduce occlusions if they are slow moving occlusions (e.g. clouds of smoke). The downside is that they can magnify undesired changes like scratches or imperfections in the film.

Change from shift image.

A change image can also be derived from the same image if the image is shifted by a certain number of pixels. A change image derived from the same image would subtract out most of the ambient light. To retain the presence of the timing mark the image can be shifted the length of the diameter of the timing mark so that the timing mark is shifted such that it no longer overlaps itself. This would result in a change image that highlights the timing mark to the maximum extent possible, while still removing a fair amount of the ambient light. This would occur at about 40 pixels, which is the anticipated diameter of the timing marks.

This change approach is not as beneficial as changing from the previous image in the situation of occlusions. Shifting the image also shifts the occlusions resulting in the occlusions still existing in the change image. This is potentially helpful when an image

is washed out because of overexposure. In the overexposure case, the overexposure is subtracted out, making the timing mark more pronounced because the overexposure noise is reduced.

Interval sensing and interval skipping.

Once an approach can effectively detect most of the timing marks, it is possible to speed up the processing by skipping over images that are likely not to have timing marks because they are too close to the previous timing mark. One simple example might be taking advantage of the fact that there are at least 5 frames between timing marks. If a mark is detected, then the processing can jump forward at least 5 frames before resuming. This would speed up the processing considerably because the image processing is the largest consumer of processing resources in the algorithm. It also reduces the potential for a false detection because images that are known to not have marks are not checked.

This basic case can be adapted to increase the timing interval over time to fit the film interval better. The timings marks gradually spread out in frames as time passes. That's because the timing interval is consistent, but the film spins faster as the weight on the spool of film decreases. While the nominal speed of the film is 2500 frames per second, this acceleration effect can result in a film speed over 3000 frames per second.

Consider an approach that calculates the previous timing interval based on the two most recent timing detections and applies this interval to the future. This allows the timing interval to adapt but it is also sensitive to the effect of missed detections and false detections. There are some cases where the interval decreases by one because of where the detections fall within the frames. For example, when detections are occurring from the middle of one frame to the middle of another the interval might

21

be eight. But if the detection occurs late in the first frame and early in the later frame, that same interval would be seven frames apart.

A missed detection would be catastrophic for the procedure. If a detection were missed that would mean that the interval would double. The result of a doubled interval would skip over every other timing mark. Successive missed timing marks would increase the timing interval further compounding the problem. Thus, being conservative, the interval is reduced by one to ensure detections are not missed. Fortunately, the spreading out of timing marks is gradual. Intervals should never double immediately and if they do, it can be assumed that a detection was missed and the interval reduced appropriately.

Combining approaches.

It is intuitive that combining some approaches would be beneficial when the approaches dovetail, while other approaches do not combine well. For example, interval skipping would not work well with an approach that only detects 50% of timing marks. However, interval skipping works well at reducing false positives when combined with a detection scheme that finds 90% of timing marks. It is also apparent, that if change images are used, that they are mutually exclusive so only one of the change image approaches can be used, not both of them. Rather than subtracting out unwanted light and exposure, a double change image would add more differencing back into the final result.

The two major approaches (column sum and circle detect) were tried as **AND** combinations and **OR** in attempt to create one superior model. While the **AND** case had fewer false positive detections, it was at the expense of missing good detections (i.e true positives). The **OR** case was similar, except while it maximized true positive detections, it also increased false positive detections.

Table 2. Workload of videos.

Type	Videos
Normal	Wasp Prime videos 2, 3, 4, 6, 9, 10, 17, 18
Occluded	Tesla videos 6, 7, 9
Washed Out	Wasp Prime video 12

2.3 Timing Results

The NUDET films tested were the Wasp Prime and Tesla nuclear detonations recorded and digitized by LLNL [30]. They were split into three groups (see Table 2) to cover the cases of 1) videos with occlusions, 2) videos that are washed out, and 3) videos that do not have occlusions or are washed out (i.e. normal).

Overall, twelve different combinations of approaches were tested with parameter tuning (Table 3). Preliminary testing was accomplished on a subset of the data to determine the best parameters for the width of the column and the best length of moving average to use with a relative threshold. Moving average lengths were tested between 10 and 40 with the best length of moving average found to be 15. This result makes sense because most of the videos have a largest interval of about 15 because with a moving average equal to 15, there is a relative low in the average pixel value right about the point in time where a detection is about to occur making it slightly more likely to detect the change in pixel values. The column width generally performed best when the width of the column was 60, the exception was with algorithm number 11 which performed best with the column width set at 40.

Algorithm 8 was a previous algorithm that used strictly circle detect in previous smaller scale study on the same topic [17] which was repeated in this test with the expanded data set for comparison. The results in Table 4 show the results of algorithm 8 compared with the other top performing algorithms for each type of video with the best overall values listed in boldface. Referring to the table, Algorithm 12 improves on algorithm 8 in the normal video by only 0.1% in the probability of detection,

Table 3. Combinations of approaches used.

Alg	Column Sum				Circle Detect			
	Gbl Avg	Mov Avg	Chg Prev	Chg Shift 40	Col Sense	No Col Sense	Chg Prev	Intvl Skip
1	X							
2	X		X					
3		25	X					
4		25		X				
5		15		X				
6		15		X	OR			
7		15		X	AND			
8						X		
9					60			
10					60		X	
11					40		X	X
12					60			X

Table 4. Combinations of approaches used.

Alg.	Video Type					
	Normal		Occlusion		Washed Out	
	P_D	P_{FA}	P_D	P_{FA}	P_D	P_{FA}
5	95.3%	2.1%	59.1%	58.3%	**88.6%**	**5.9%**
8	99.2%	28.7%	78.8%	90.1%	87.7%	4.2%
11	34.6%	18.8%	**77.3%**	**11.3%**	44.9%	0.9%
12	**99.3%**	**2.6%**	60.6%	61.4%	19.5%	2.1%

but improves the probability of false alarm by 26.1%. Algorithm 11 improves on algorithm 8 in the occlusion case by reducing the false alarm rate by 78.8% although the probability of detection decreases by 1.5%. For the washed out case, algorithm 6 is similar to algorithm 8 by improving detection probability by 0.9%, however the probability of false alarm increases by 1.7%. Algorithm 12 is superior in the most common case and provides a baseline for timing mark detection that was used in the remainder of this research.

Table 5 shows the time performance results of the algorithm. The circle detection algorithms take longer than the column sum algorithms because the Hough transform

Table 5. Execution time of algorithms.

	Algorithm Num			
	5	8	11	12
Avg Time/video (sec)	65	320	118	122
Avg Time/detection (sec)	0.39	1.76	0.71	0.73

is more computing intensive. The fact that the column sum takes 1/5th the amount of time than the original circle detection algorithm is significant. The reason why the other circle detection algorithms run faster than the original is attributed to the interval skipping.

2.4 Time Alignment of Films

Once the location of timing marks are determined, the time stamp of each frame needs to be determined. The process of extracting timing is to analyze each frame of a film in sequence to detect the locations of timing marks [16] [20] [24] [31]. The frame rate is found by relating the film marks to their 5 msec timing interval. A series of frame rates is then fit to a cubic spline [22] (Fig. 12). Lastly, the time between frames, Δt, is found as an inverse of the frame rate estimated at each frame on the cubic spline.
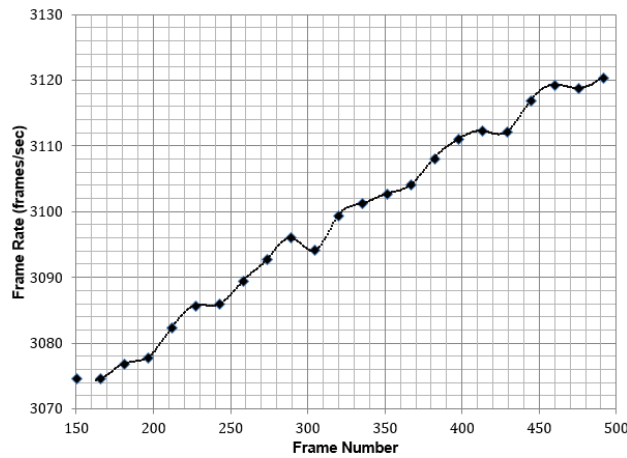
Figure 12. A cubic spline fit to the frame rate of the Climax detonation.

25

Next, the timestamps need to be adjusted for when the start of the detonation occured within the first frame. For a film with nominal speed of 2,500 frames per second, that results in an exposure time of 0.4ms, meaning that the time of detonation (t=0) could occur at any point within the 0.4ms exposure time. This time of detonation uncertainty is propagated throughout the film if not corrected.

To correct for the time of detonation, the point at which time zero occurred (when the detonation began) in the film needs to be determined. For purposes of discussion the frame that has the first visible exposure of the detonation will be referred to as the *frame-of-first-light*. The size of the fireball in the frame-of-first-light, relative to the size of the fireball in the next frame is an indicator of when the detonation occurred relative to the frame-of-first-light. The smaller the ratio of the fireball radii, the later the detonation occurred in the frame-of-first-light [31]. Notationally calling the frame-of-first-light F_0, and the next frame F_1, the time difference, Δt_0 is defined to be the time elapsed between F_0 and F_1. The duration δ is defined to represent the period of time between the start of F_0 and the point at which $t = 0$ actually occurred during the frame's exposure (Fig. 13). Absolute time is then given by

$$t_n = \sum_{i=1}^{n} \Delta t_i + (1 - \delta_f)\Delta t_0 = (F_n - F_0)\Delta t_0 + (1 - \delta_f)\Delta t_0$$

where $\Delta t_0 = \frac{1}{(fps)_0}$ and $\delta_f = \frac{\delta}{\Delta t_0}$. The ratio of radii can be established from Taylor's equation [36] for the radial growth of a nuclear detonation over time as

$$\frac{R_{n=1}}{R_{n=0}} = \frac{R_1(2\Delta t - \delta_f \Delta t)^{0.4}}{R_1(\Delta t - \delta_f \Delta t)^{0.4}}.$$

Solving for δ_f then generates

$$\delta_f = \frac{2 - [\frac{R_{n=1}}{R_{n=0}}]^{2.5}}{1 - [\frac{R_{n=1}}{R_{n=0}}]^{2.5}}.$$

26

Finally, the time $\delta = \delta_f \Delta t$. To validate that the timing was correct, the radius of a
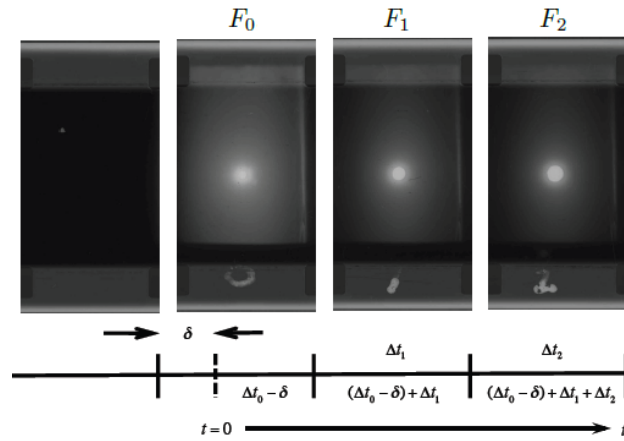
Figure 13. The methodology to align the timing of films with time $t = 0$ [**31**].

detonation from collection sites with multiple cameras were compared to each other with their radii plotted over time. With nearly identical focal lengths, the expectation was that frames of the same time would have the same radius in the nuclear detonation regardless of whether they were captured by fast or slow camera rates. This fact was verified in each film where there were multiple cameras from the same collection site. Fig. 14 shows an example output of the time analyzed from a collection site of the Tesla detonation that had six cameras. Other than the outliers caused by errors in the radius detection, the prevailing trend of radius growth over time is confirmed.

2.5 Timing Conclusions

This experiment explored several approaches to detecting timing marks in nuclear detection video. It was determined that the previous best method of basic circle detection can be improved upon by adding interval skipping which reduces the false positive rate by 26.1% and reduces the processing time by a factor of 2.5. When detection in occluded videos is required, an approach that includes both a change detection from the previous image and interval skipping reduces the false positive
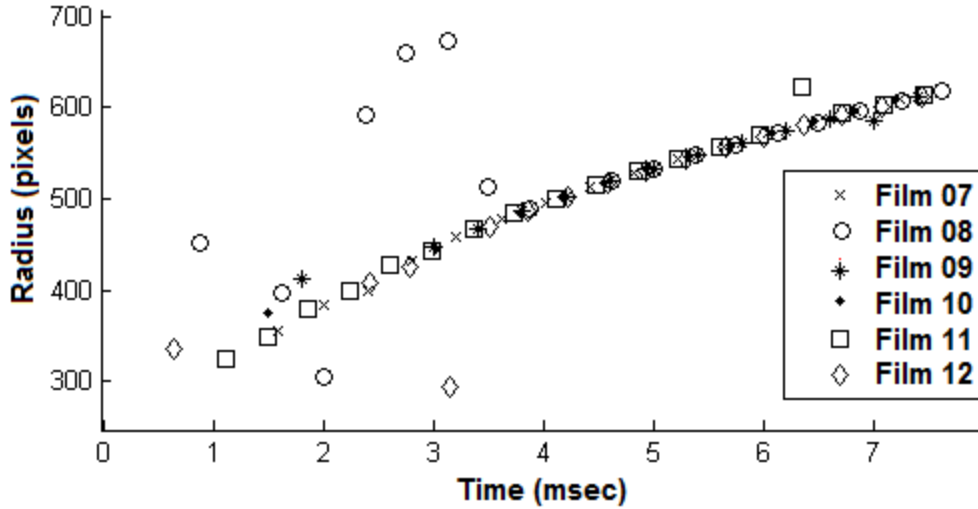
Figure 14. A plot of radius growth over time based on time estimates from multiple cameras from Tesla Truck 7. A few outliers exist that were a result of errors in the automated detection of the radius of the detonation.

rate by 78.8% and cuts processing time by a factor of 2.5. When detection in washed out or overexposed videos is required, the processing time can be cut significantly with similar detection results.

With timing marks detected accurately, the timestamp of each frame can be estimated by fitting the frame rates to a cubic spline. Timestamps are adjusted based on applying Taylor's equation [36] to the radius of the fireball in the frame-of-firstlight. The end result is that each frame is timestamped relative to the start of the detonation.

28

III.   Subsphere Detection

With the videos temporally aligned, the focus shifts to detecting features on the NUDETS that can be used to estimate volume or be matched across wide viewpoints. The first feature to be detected are subspheres (Fig. 8). These features are visible areas of deformity in the detonation likely caused by obstructions that degrade the spherical uniformity of the detonation shock wave. This chapter summarizes an experiment set up to determine whether dimensionality reduction with classification is effective in detecting subspheres in the NUDETs. Furthermore, it helps determine what combinations of parameters and dimensions help produce the best results to detect subspheres in the films.

The chapter is organized beginning with a block diagram in Sec. 3.1. The results of applying the nuclear subsphere detection approaches are discussed in Sec. 3.2. Lastly, conclusions are drawn in Sec. 3.3.

3.1   Block diagram

Fig. 15 shows a block diagram for the system that is designed to detect subspheres in a NUDET image aptly named the NUDET Subsphere Detector (NSD). Each of the parameters discussed in this algorithm synopsis is described in detail. The NSD is broken into two primary parts: the learner, and the detector. The learner's function is to use the truth information and dimensionality reduction algorithms to determine which dimensions are best for the detector to use. The learner imports an image and applies a filter to the image. Iterating through each pixel in the image, the dimension extractor extracts 300 dimensions from the surrounding pixels based on the kernel size. It then applies a dimensionality reduction algorithm to the dimensions to determine the most relevant dimensions. Using the most relevant dimensions, a Mahalanobis-
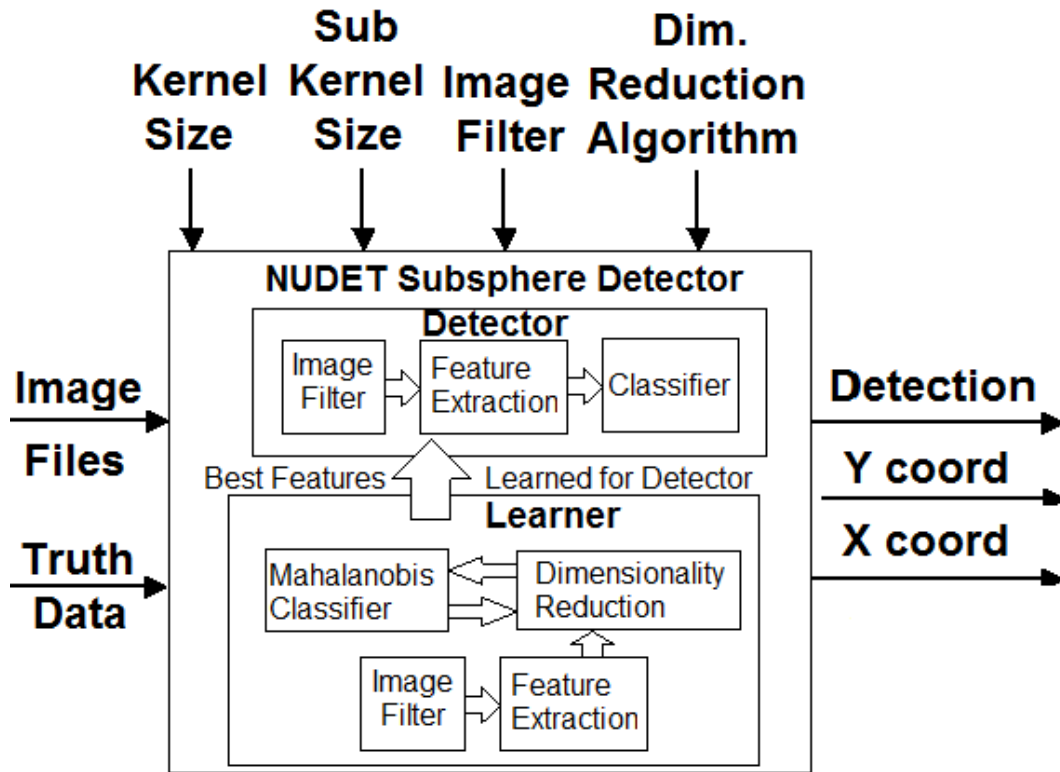
Figure 15. Block Diagram for Subsphere Detector.

based classifier determines if the pixel in question is a subsphere edge or not. Lastly, the detected pixels are clustered into neighboring detected pixels to create the list of subspheres with their corresponding locations. When the learner is complete, the best dimensions are then used as the basis of the detector to detect the subspheres. The detector then runs similar to the learner without the dimensionality reduction. It uses the dimensionality reduction's recommended dimensions to determine which pixels have subspheres in them.

Inputs.

Along the left side of the block diagram (Fig. 15) are the inputs, which are the subject image and a human interpretation of where subspheres exist in the image (i.e truth data). The truth data is used initially in the dimensionality reduction to "learn"

which dimensions are the best dimensions to use in detection. Later, in validation and testing, it is used to determine whether a detection is a true positive or false positive.

Parameters.

Along the top of the block diagram (Fig. 15) are the parameters that we will vary in the experiment. The kernel is the size of sub image that will be used. Kernels of 7×7, 15×15, 21×21, and 25×25 pixels were tested. The sub-kernel size defined the size of subsections within the kernel. Sub-kernel sizes included 1×1 pixels, 3×3 pixel, and 5×5 pixels related to the kernel size. These are defined in Table 6. The combination of the kernel and the sub-kernel sizes creates a patchwork of sub-kernels that are used to define dimensions. The image filter parameter is which filter is used to preprocess the image. Images were either preprocessed with a histogram equalization algorithm, a Wiener filter, a median filter, or were not filtered. The last parameter is which dimensionality reduction algorithm was used to select the best dimensions for classification. Two dimensionality reduction algorithms were tested: principal component analysis (PCA) and forward subset selection. The combination of four kernels, four filters, and two dimension reduction algorithms gives 32 (4 kernels ×4 filters ×2 feature selectors) separate configurations of the NUDET subsphere detector.

Table 6. Kernel sizes tested.

Kernel Size	Sub Kernel Size	Num. Sub Kernels
7×7	1×1	49
15×15	3×3	25
21×21	3×3	49
25×25	5×5	25

Outputs.

The outputs of the NSD include whether a subsphere edge detection occurred, and at what X and Y pixel.

3.2 Subsphere Detection Results

To analyze which algorithm/kernel/filter combination performed best, the data was analyzed using a Receiver Operating Characteristic (ROC) curve. A ROC curve plots the results of the Hit Rate (Eq. 4) along the y-axis and False Alarm Rate (Eq. 5) along the x-axis. Each algorithm/kernel/filter combination was plotted on a ROC curve for the top 50 dimensions according to either the PCA or sequential forward subset (SFS) algorithm. ROC curves provide a way to graphically determine what the maximum Hit Rate while minimizing the False Alarm Rate.

$$Hit\ Rate = \frac{True\ Positive}{True\ Positive + False\ Negative} \tag{4}$$

$$False\ Alarm\ Rate = \frac{False\ Positive}{False\ Positive + True\ Negative} \tag{5}$$

Sequential Forward Search.

The best performing SFS algorithm was a 15×15 kernel without a filter and is shown in Fig. 16. From this figure, the occurrence with 18 dimensions was chosen as a bend in the curve which had a 67% hit rate and 22% false alarm rate. Fig. 17 shows the results of a SFS, 15×15 kernel with the first 18 dimensions. The results plotted on the image are mixed. Many areas of interest are detected with wider areas than needed. There are also other areas that have similar characteristics that are detected. One attempt to clean up the results was to pass a 4×4 filter over the top of these results which eliminates the smaller detections, and thins the larger detections. the
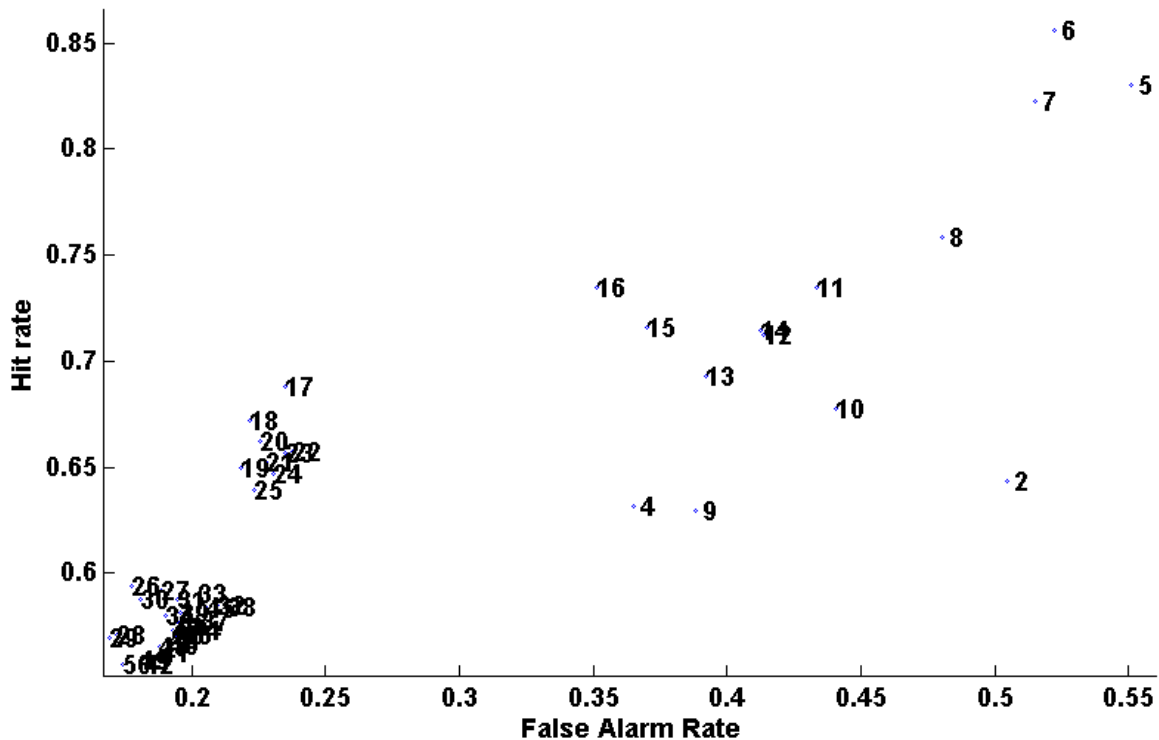
Figure 16. ROC curve for SFS 15×15, no filter. Each point is labeled with the number of dimensions representing the Top N dimensions that were used.

results of the 4×4 filter are shown in Fig. 18.

Sixteen ROC curves were generated in total for SFS which will not be listed here, however other examples of SFS ROC curves that did not perform as well for comparison was SFS 15×15 Wiener (Fig. 19) and SFS 15×15 Median (Fig. 20). SFS 15×15 Wiener was not chosen because its best comparable performance to SFS 15×15 was 66% hit rate with a 26% false alarm rate, underperforming SFS 15×15 by 1% in hit rate, and 4% in false alarm rate. SFS 15×15 Median was not chosen because its best comparable performance to SFS 15×15 was 64% hit rate with a 26% false alarm rate, underperforming SFS 15×15 by 3% in hit rate and 4% in false alarm rate.
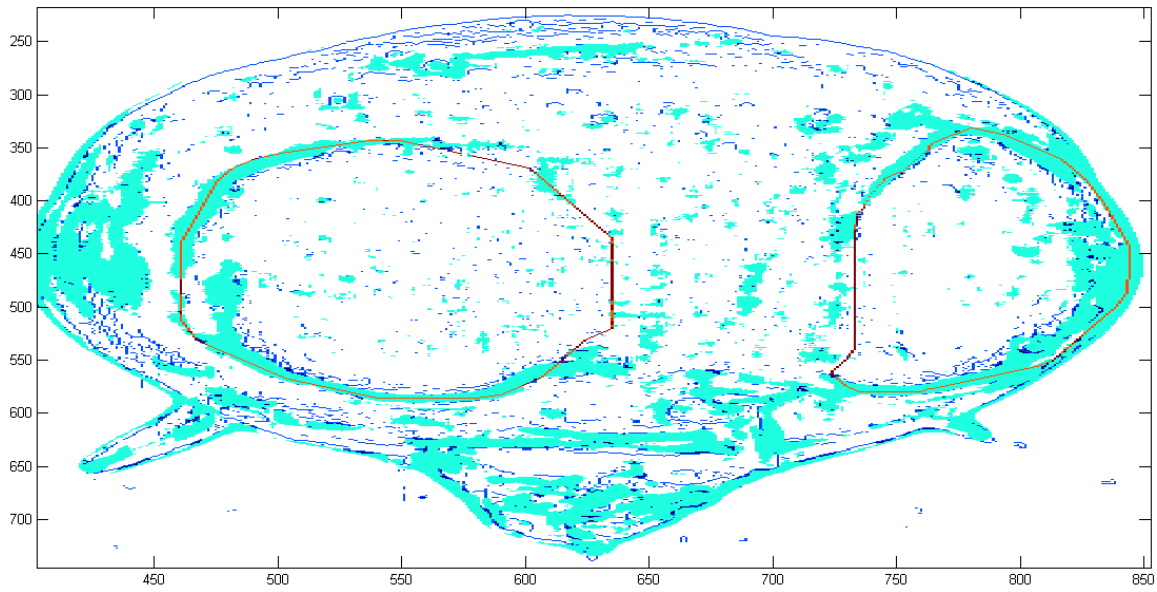
Figure 17. Image representation of detections for SFS 15×15, 18 dimensions, no filter. Areas in light blue are false detections. Each subsphere is traced in red. Overlapping light blue with red represents a true positive.
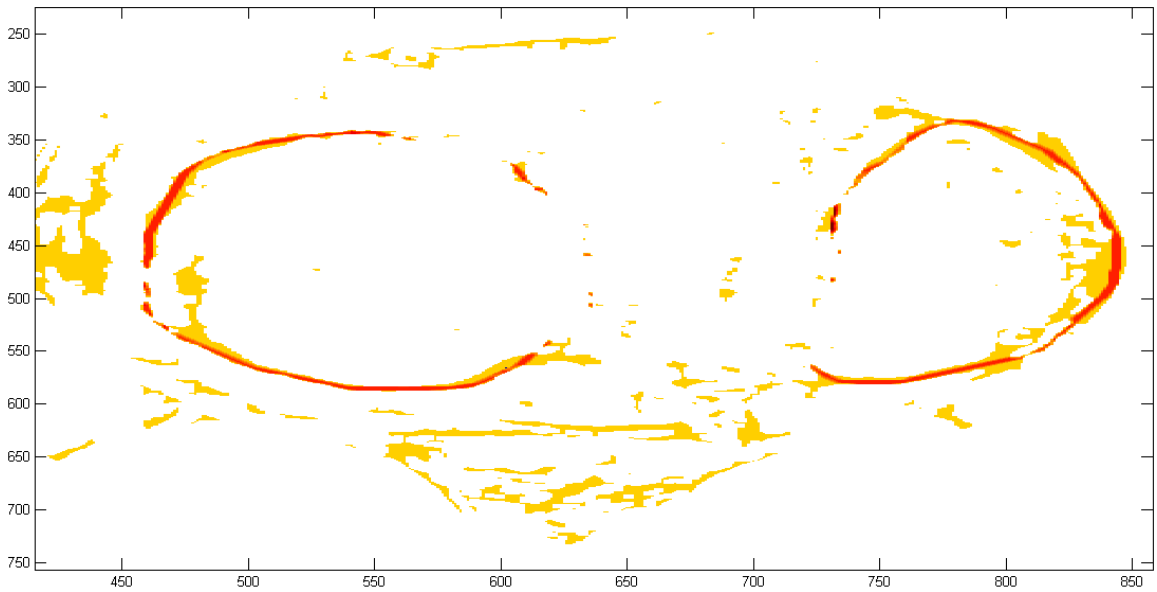
Figure 18. Image representation of detections for SFS 15×15, 18 dimensions, with a post-process 4×4 averaging filter. Areas in orange are false detections. Areas in red are true positives.
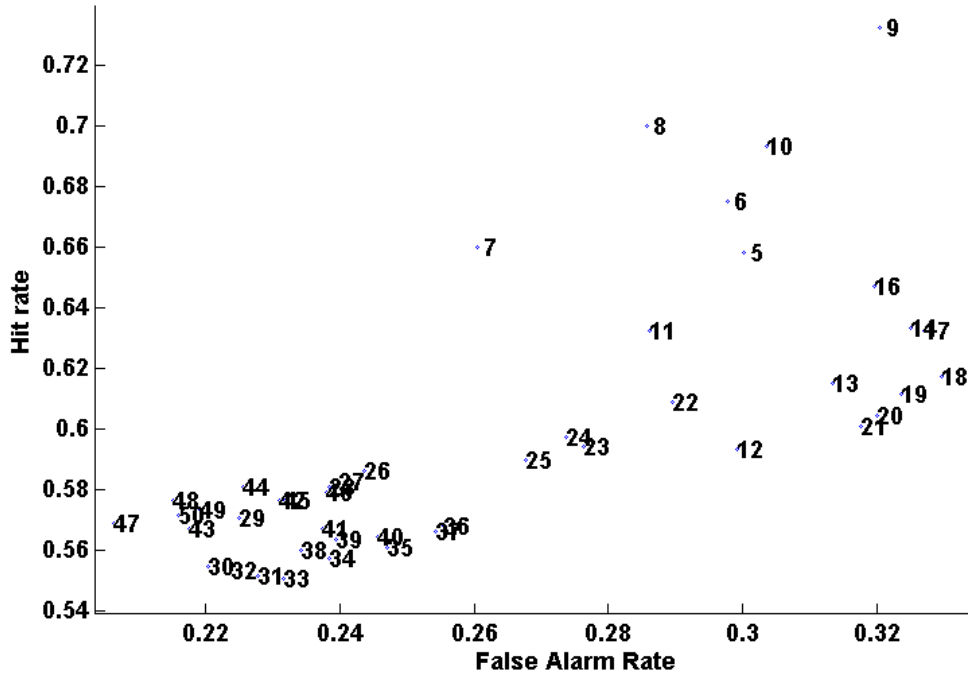
Figure 19. ROC curve for SFS 15×15, Weiner filter. Each point is labeled with the number of dimensions representing the Top N dimensions that were used.
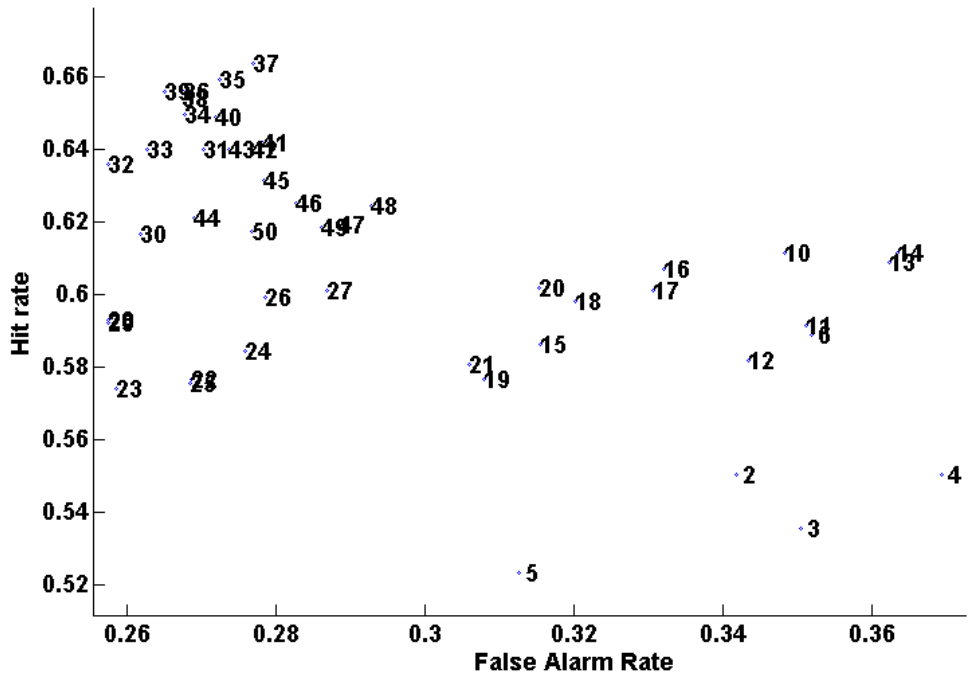
Figure 20. ROC curve for SFS 15×15, Median filter. Each point is labeled with the number of dimensions representing the Top N dimensions that were used.
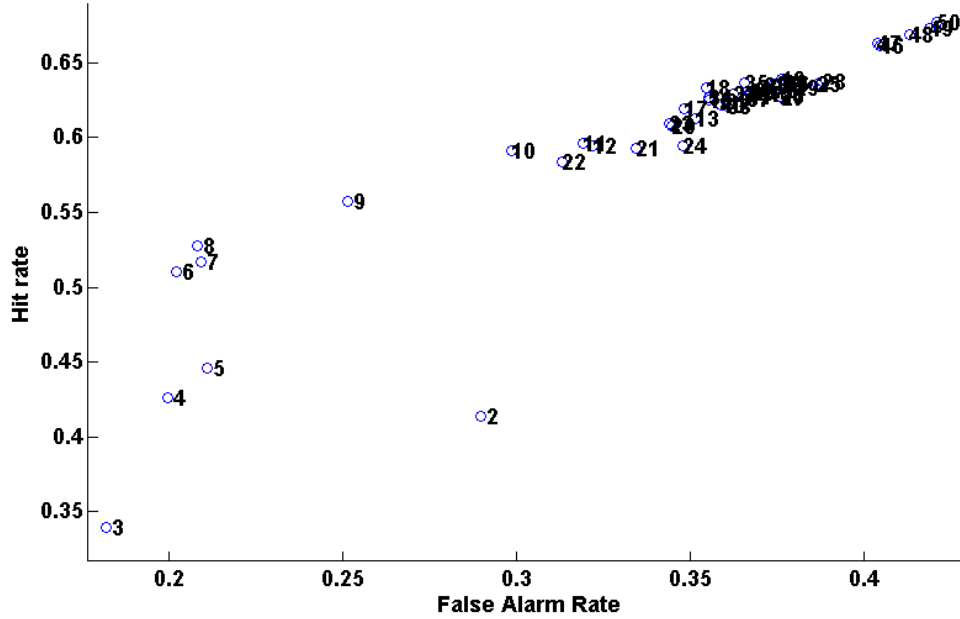
Figure 21. ROC curve for PCA 21×21, no filter. Each point is labeled with the number of dimensions representing the Top N dimensions that were used.

Principal Component Analysis Results.

Principal Component Analysis results were interesting. One item of note was that the median and Weiner filters performed exactly the same for all kernels. This is not particularly strange as both filters are designed to reduce noise, and with PCA focused on finding dimensions of maximum variance, it appears that both noise minimization filters affected the image in the same way that PCA perceives it. The best results for PCA were for the 21×21 kernel with no filter (ROC curve Fig. 21, image Fig. 22). Also, the 4×4 filtered image is shown in Fig. 23.

Best Filtering.

The best filtering approach was not to filter at all. Both the median filter and the Wiener filter behaved identically to the unsupervised PCA dimension reduction. And while the purpose of noise reduction for which the Wiener filter and median filter were used it appeared to be unnecessary with regard to subsphere feature detection.
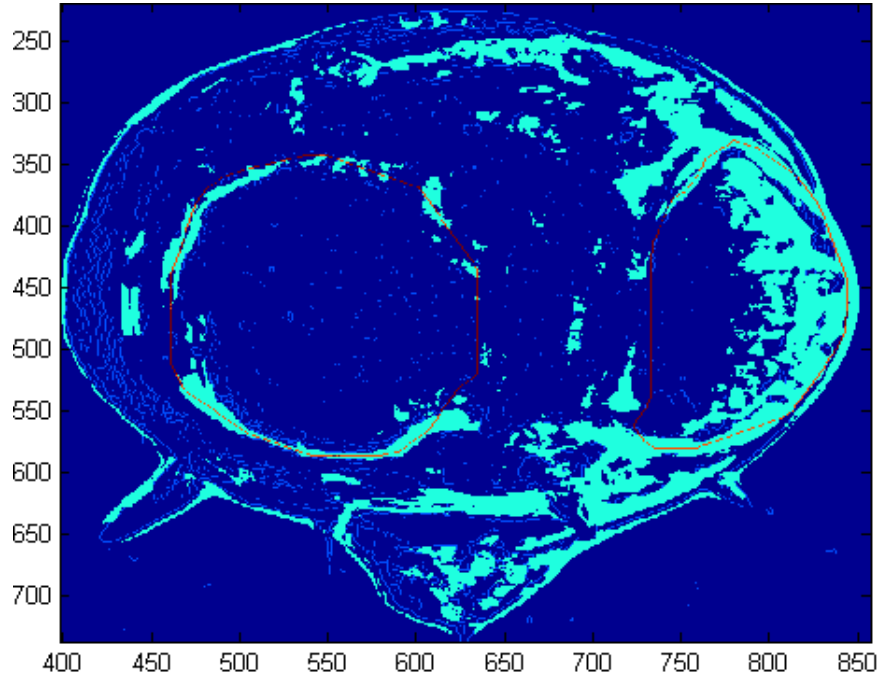
Figure 22. Image representation of detections for PCA 21×21, no filter. Areas in light blue are false detections. Each subsphere is traced in red. Overlapping light blue with red represents true positive detections.
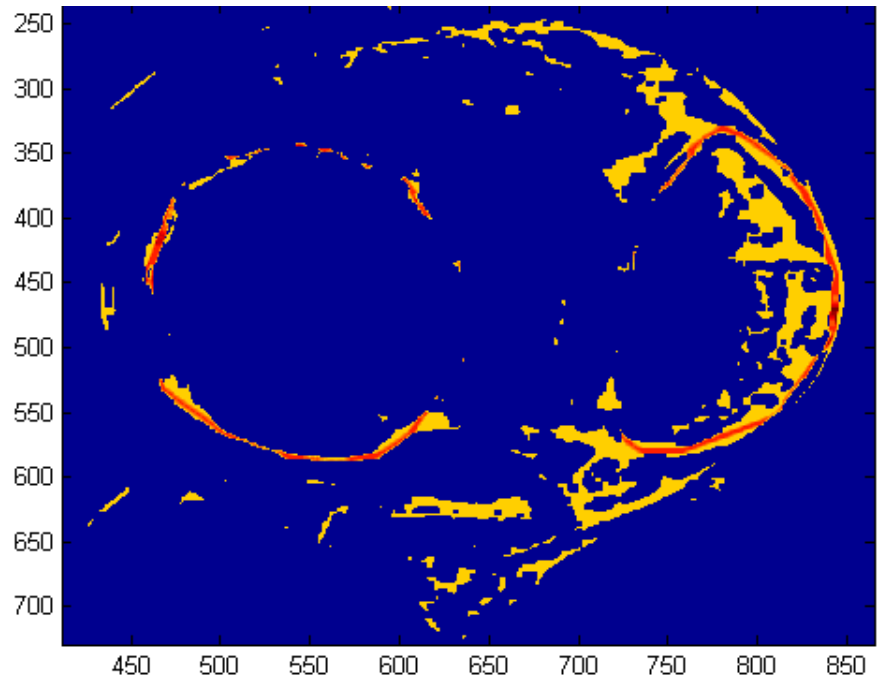
Figure 23. Image representation of detections for PCA 21×21, with a post-process 4×4 averaging filter. Areas in orange are false detections. Areas in red are true positives.

There are other images and videos in the NUDET data set that these filters may apply better to, but it appears that their application to images that are clear and relatively unaffected by noise are not beneficial in subsphere feature detection.

3.3 Conclusions

This chapter tested which combination of kernels (7×7, 15×15, 21×21, and 25×25 pixels), dimension reduction algorithms (SFS, PCA), and filters (no filter, histogram equalization, Wiener, and median) worked best to detect the edges of a subsphere in a nuclear detonation image. The best result had a 67% hit rate and 22% false alarm rate and was SFS 15×15 with no filter, with the top 18 dimensions. These results were further improved by applying a 4×4 averaging filter and is shown in Fig. 18. The location of subsphere features are used in estimating the volume of NUDETs which is discussed in Chapter VII.

IV. Hotspot Detection

The next feature to be detected are hotspots (Fig. 9). These are spots on the surface of the detonation that are at higher temperature relative to the local area around it that cause it to be brighter. This chapter discusses a process that is defined to detect hotspots. It describes an experiment used to determine whether a supervised learning tool like dimensionality reduction is effective in detecting hotspot features in the NUDETs. Furthermore, if it is effective, the experiment determines what combinations of parameters and dimensions produce the best results. This material appears in the IEEE Computer Society's Proceedings for the 43rd Applied Imagery Pattern Recognition Workshop [23].

This chapter is organized as follows. First, a block diagram with inputs, parameters, and outputs are discussed in Sec. 4.1. The results of applying hotspot detection to the films are depicted in Sec. 4.2. Applying the results of hotspot detection concludes the chapter in Sec. 4.3.

4.1   Nuclear Hotspot Detector

Fig. 24 shows a block diagram for the system that is designed to detect hotspots in a NUDET image aptly named the NUDET Hotspot Detector (NHD). Each of the parameters discussed in this algorithm synopsis is described in detail. The NHD is broken into two primary parts: the learner and the detector. The learner's function is to use the truth information and dimensionality reduction algorithms to determine which dimensions are best for the detector to use. The learner takes an image in and applies a filter to the image. Iterating through each pixel in the image, the dimension extractor extracts 300 dimensions from the surrounding pixels based on the kernel size. It then applies a dimensionality reduction algorithm to the dimensions to de-
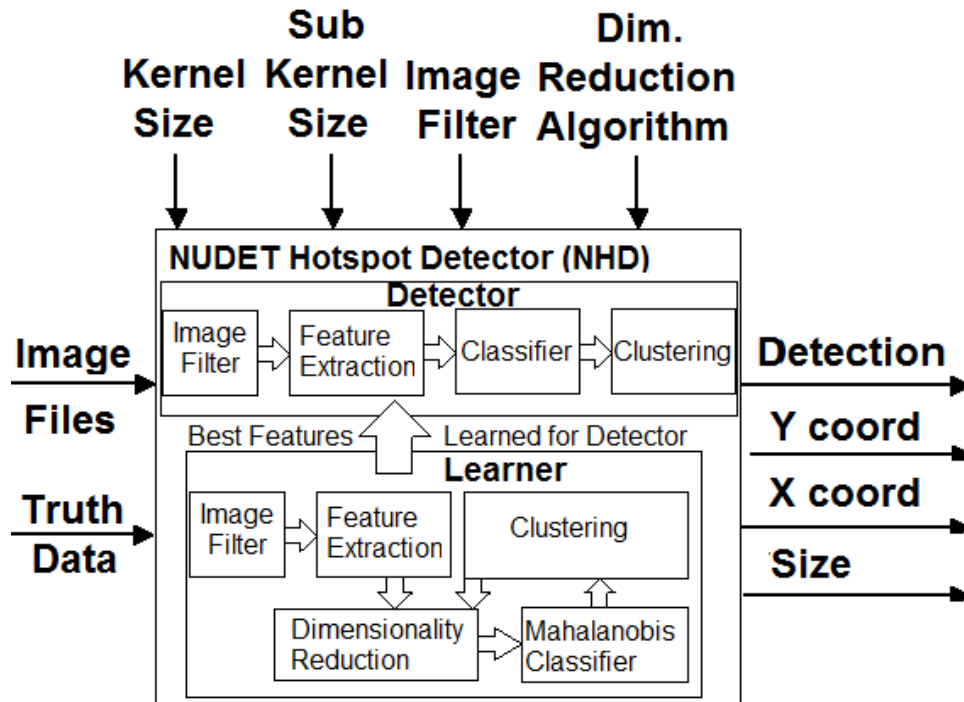
Figure 24. Block Diagram for Hotspot Detector

termine what the most relevant dimensions are. Using the most relevant dimensions, a Mahalanobis-based classifier determines if the pixel in question is a hotspot or not. Lastly, the detected pixels are clustered into neighborhoods of detected pixels to create the list of hotspots with corresponding locations and size. When the learner is complete, the best dimensions are then used to be the basis of the detector to detect the hotspots. The detector then runs detection with the results of the learner's dimensionality reduction. It uses the dimensionality reduction's recommended dimensions to determine which pixels have hotspots in them.

Inputs.

Along the left side of the block diagram (Fig. 24) are the inputs, which are the subject image and a human interpretation of where hotspots exist in the image (i.e. truth data). The truth data is used initially in the dimensionality reduction to "learn"

Table 7. Kernel sizes tested.

Kernel Size	Sub Kernel Size	Num. Sub Kernels
7×7	1×1	49
15×15	3×3	25
21×21	3×3	49
25×25	5×5	25

which dimensions are the best dimensions to use in detection. Later, in validation and testing, it is used to determine whether a detection is a true positive or false positive.

Parameters.

Along the top of the block diagram (Fig. 24) are the parameters that will be varied in the experiment. The kernel is the size of sub image that will be used. In exploration of the data, it appeared that hotspot size ranged from 5×5 pixels to 14×16 pixels in size. To accommodate the varied size kernels of 7×7, 15×15, 21×21, and 25×25 pixels were defined. The sub-kernel size defined the size of subsections within the kernel. Sub-kernel sizes included 1×1 pixels, 3×3 pixel, and 5×5 pixels related to the kernel size. These are shown in Table 7. The combination of the kernel and the sub-kernel sizes creates a patchwork of sub-kernels that are used to define dimensions. The image filter parameter is whether preprocessing is used to modify the image prior to dimension extraction. Images were either preprocessed with a histogram equalization algorithm or were not filtered. The last parameter is which dimensionality reduction algorithm was used to select the best dimensions for classification. Four dimensionality reduction algorithms were tested: principal component analysis (PCA) [1], forward subset selection [1], ReliefF [33], and FCBF(Fast Correlation-Based Filter) [14].

Table 8.   Number of dimensions per method.

Method Grouping	Number of Dimensions
Avg, Min, Max Pixel Values	43
Entropy	12
Prewitt Edge Detection	38
Sobel Edge Detection	38
Zero-cross Edge Detection	38
Canny Edge Detection	38
Gradient X direction	38
Gradient Y direction	38
2D Fourier Transform	17

Outputs.

The outputs of the NHD include whether a detection occurred, at what X and Y pixel, and the total clustered size of the detection (in pixels).

Dimensions.

Dimensions were defined based on the pixel intensity within a kernel-sized patch of pixels. The goal was to use a variety of methods that would be helpful in detecting hotspots as well as avoiding false detections. Dimensions were grouped by primary method of data source to include edge detection algorithms, the 2D Fourier Transform, entropy, gradient and sub-kernel pixel intensities. A breakout of the number of dimensions summarized by method is shown in Table 8. Since the algorithm needed to work in several stages of the detonation, it was believed that sub-kernel patches would need to be compared to one another. As a result, a series of differencing schemes were defined to compare sub-kernel patches within a kernel. An example of schemes that were used is shown in Fig. 25. Comparing Table 8 and Fig. 25 it can be noted that the same 38 schemes are used for different edge detections and gradient values. Those same 38 schemes are also a subset of the 43 that are used in the average pixel values.
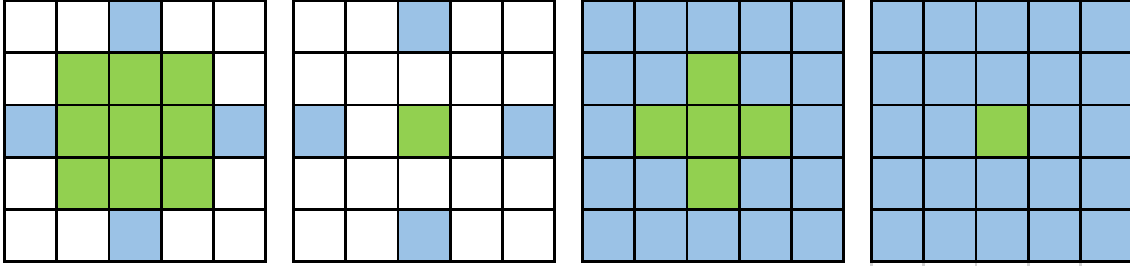
Figure 25. Four examples of sub-kernel schemes. The 5×5 grid represents 25 sub-kernels for a 25×25 or 15×15 kernel. In the 25×25 case, each square represents a 5×5 pixel area, while in the 15×15 case each square is a 3×3 pixel area. An averaging dimension value example would be, averaging the green pixels and subtracted them from an average of the blue pixels. A min/max dimension example would take an average of the max of the green sub-kernels minus an average of the min of the blue pixels.

4.2 Hotspot Detection Results

Early in testing it was apparent that the 7×7 kernel size was significantly under-performing with regard to maximizing true detections and minimizing false detections when compared the other three kernels, as a result it was removed. This makes sense because it is difficult to detect a 14×16 pixel sized hotspot when only looking at a 7×7 pixel subset of it. Also, FCBF results were discarded. While the speed of FCBF was fast (several seconds), the result was only one or two dimensions which was deemed to be too few to apply to validation and testing data sets.

Fig. 26 shows a hit rate summary, while Fig. 27 shows a summary of precision and Fig. 28 shows false alarms for all algorithms and kernels tested. Hit rate showed a good spread of capabilities with sequential forward subset (SFS) generally being on top. False alarm rates were very low because of a high number of true negative detections influencing the calculation. ReliefF showed higher precision than most other algorithms. These numbers alone do not tell the full story however.

One obstacle that needed to be overcome to evaluate the effectiveness of the learner and detector was reconciling the truth data. The truth data was designed with a human picking out the center pixel of a hotspot, however, the detector de-
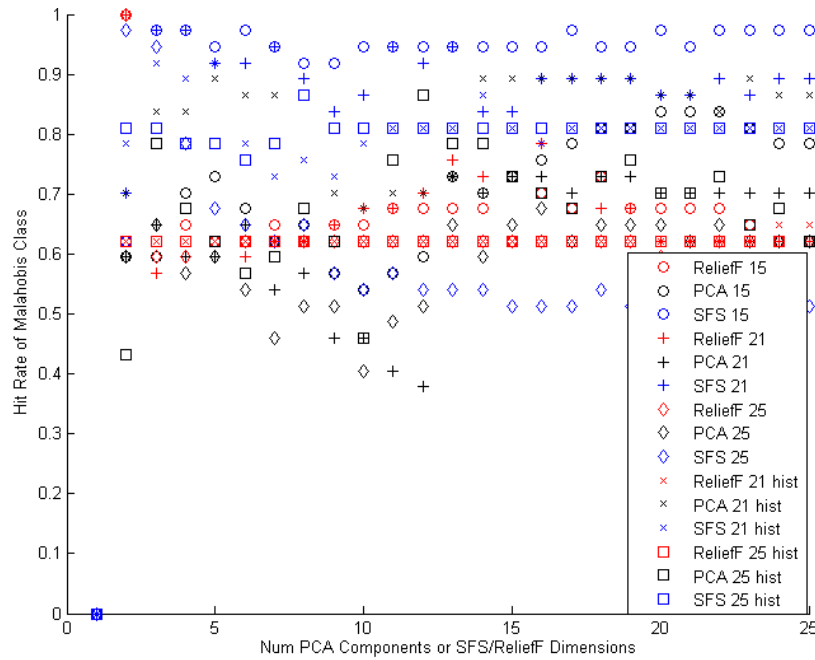
Figure 26. Hit rate by dimension reduction algorithm and number of dimensions. In general, the SFS algorithms performed best, with PCA algorithms improving as components were added.
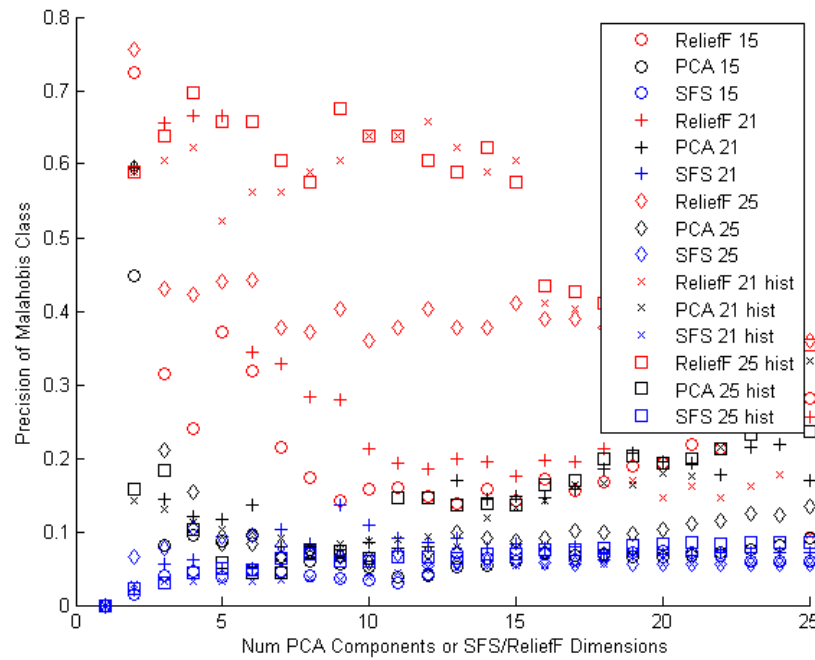
Figure 27. Precision by dimension reduction algorithm and number of dimensions.
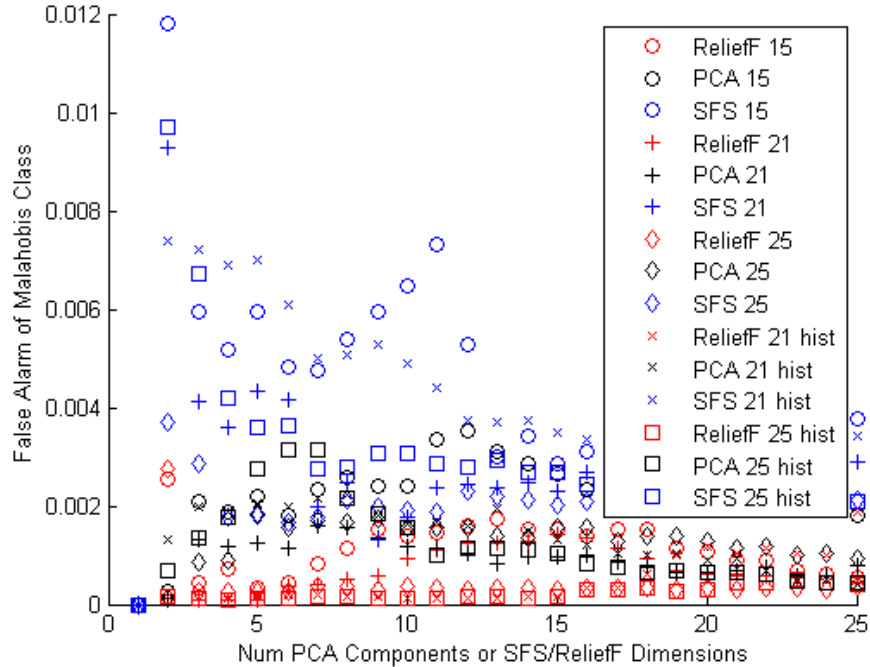
Figure 28. False alarm rate by dimension reduction algorithm and number of dimensions.

tected the entire hotspot. This required the detections to be clustered in order to accurately calculate detection probabilities. The effect of the impact of clustering is demonstrated in Fig. 29. In addition, there are some clusters that are rather large (500-1000 pixel area) that need to be rejected, as well as small hotspots (less than 5 pixels) that also need to be rejected. This combination of clustering and rejecting large clusters appears to work best with SFS.

ReliefF results differ greatly from SFS. Fig. 30 shows the unclustered results of ReliefF on a 25×25 kernel with the top 3 dimensions. Fig. 30 shows that the algorithm did not successfully detect individual hotspots, instead it detected the outer region of the explosion. When clustered, this combines several true positive detections together that are within the large boundary of the ReliefF detections. This is also the reason why ReliefF dominates the precision results (Fig. 27) because the number of occurrences are reduced skewing the precision results higher.

45
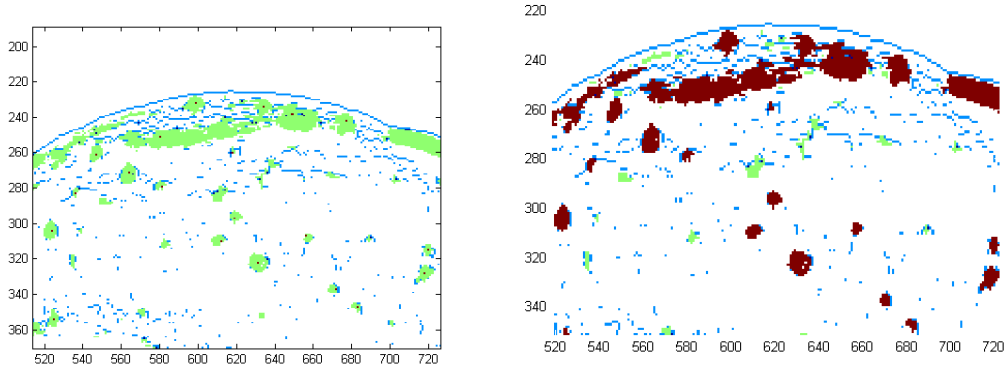
Figure 29. A comparison of truth clustering effects on the results of SFS 25×25. Red represents pixels that are true positives. Light green are pixels that are false positives. Without clustering, the left figure has true positives (red dots) surrounded by false positives that is corrected in the right figure.

Table 9. Summary of top performing algorithms.

Alg.	Kernel	feat.	Hit Rate	Prec.	F.A. Rate
SFS	15×15	3	97.3%	3.95%	0.59%
SFS	25×25	3	97.3%	5.5%	0.41%
PCA	25×25 hist	12	86.49%	14.68%	0.11%
PCA	21×21 hist	5	89.19%	10.25%	0.21%
PCA	21×21 hist	25	89.19%	29.73%	0.047%

PCA results show an improvement in both hit rate (Fig. 26) and precision (Fig. 27) as more dimensions are used. This makes sense for PCA as each additional dimension that is added is a finer tuning of the previous dimensions. Comparing 12 dimensions with 24 dimensions (Fig. **??**), while the 24 dimension PCA results have higher hit rate and precision than 12 dimensions, it is possible that it might fall victim to overtraining when applied in a larger scale. That overtraining would lead the detector's learning to become so specific to the particular characteristics of this detonation that it does not apply well to other detonations. The results also show that PCA performs well when paired with a histogram equalized 21×21 kernel. A summary of what is considered to be the top performing algorithms is shown in Table 9. A summary of the runtime performance is shown in Table 10.
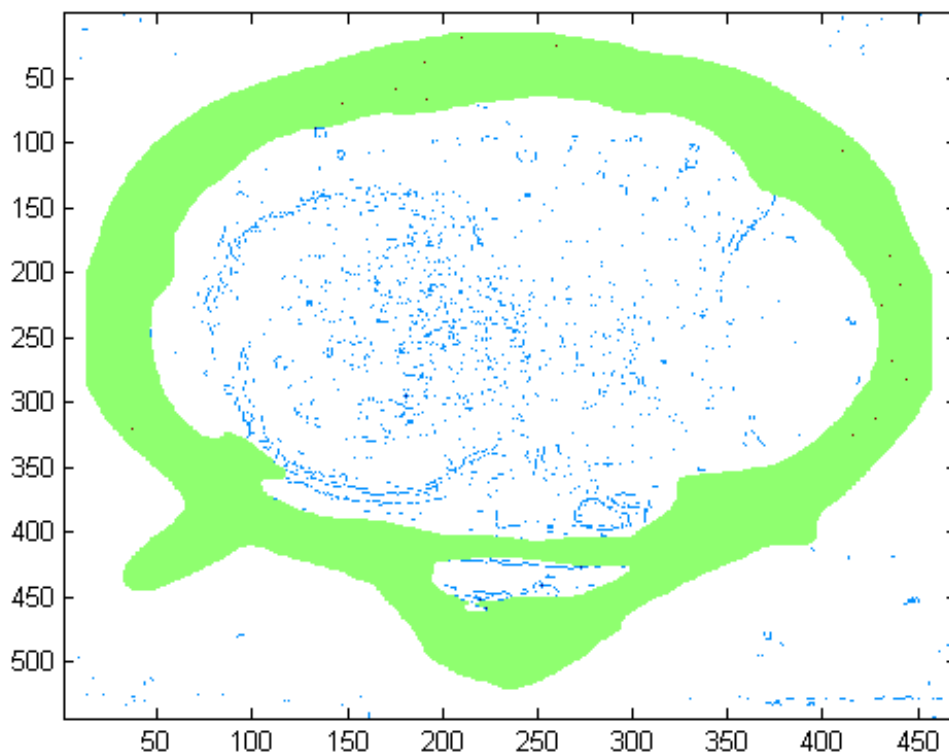
Figure 30. Results of detections for ReliefF, 25×25 kernel, top 3 dimensions plotted on an image. Red represents pixels that are true positives (visible inside the light green band). Light green are pixels that are false positives. Clustering turns all the false positives into one large true positive around the exterior of the explosion, and misses true positives in the center of the explosion.

Table 10. Runtime of algorithms.

Algorithm	Avg. Run time per image
Dimension Extraction	5.49 hrs
PCA	63 sec
SFS	8.1 hrs
ReliefF	33.2 hrs
Histogram equalization	17 sec
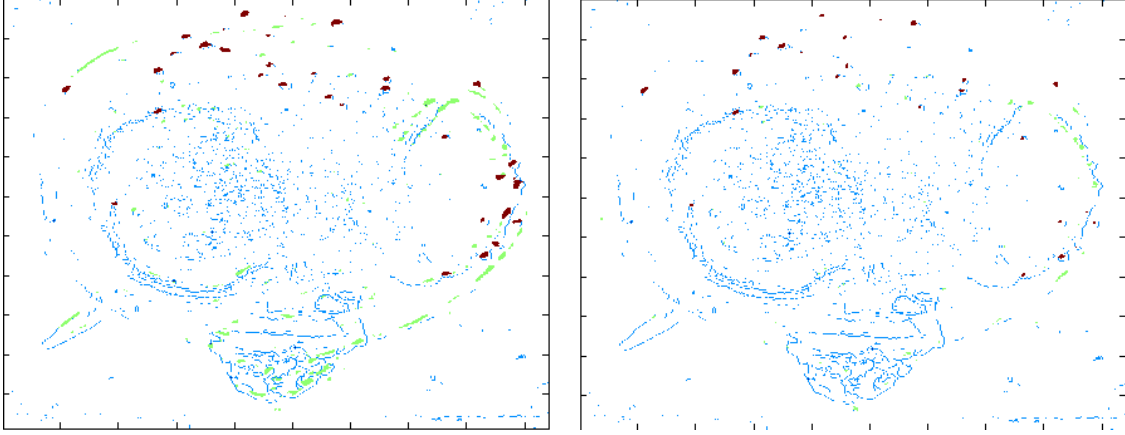
Figure 31. A comparison of truth clustering effects on the results of PCA 25×25 kernel with histogram equalization. The left image is 12 dimensions and the right image is 24 dimensions. Red represents pixels that are true positives. Light green are pixels that are false positives.

Weighing all combinations of kernels, histogram equalization and dimension reduction algorithms there is no clear top performer, but there is a group of good performers and bad performers. Bad performers include the 7×7 kernel, and the reliefF algorithm for this domain. Good performers include 15×15 and 25×25 kernels for SFS, and histogram equalization paired with PCA for 21×21 and 25×25 kernels. PCA was clearly the fastest algorithm of the dimension reduction algorithms, with SFS next and finally ReliefF (Table 10).

Overall, PCA with a histogram equalization filter was the fastest while also maintaining a 86-89% hit rate, 10-30% precision rates, and 0.047-0.11% false alarm rates. SFS, while not performing as quickly as PCA, also had 97.3% hit rate with a 0.5% false alarm rate.

4.3   Applying Hotspot Feature Detection

The next step in analyzing the NUDET films is to take the experiment results and to build and test an automated hotspot feature detector that works across multiple

detonations. The results indicated that the best dimension of the 300 dimensions studied was a 21×21 pixel kernel that took the average intensity of the center 3×3 pixel area and subtracted it from a 3 pixel border around the edge of the kernel. This dimension determined which locations of the image had the highest relative intensities to the area immediately around it. A hotspot detector was built using this dimension and detections for a hotspot were considered present when the dimensions value was larger than a threshold of the average intensity of the image + 2 standard deviations of the intensity of the overall image. The results of this simplified hotspot detector were then clustered based on whether they were adjacent to other positive detections and catalogued. Information about the hotspot cluster was further derived based on the cluster's size to include its width in the x- and y-direction, its center, and the total number of pixels in the cluster. Clusters that were too small (less than 10 pixels) or too large (greater than 100 pixels) were discarded, and those that were not balanced in x- and y-directions in span (within a 0.5 aspect ratio) were also discarded.

To determine the accuracy of this new approach to detecting hotspots, it was tested against six detonations (Grable, Climax, Boltzmann, MET, Turk, and Tesla), using at least two different viewpoints for each detonation, and 12 images for each detonation. Images selected from a detonation were balanced evenly between when detection was known to be difficult (when they are first visible in the detonation sequencing) and when it was suspected to be easiest (during t_{min} when the ambient light is lowest and the hotspots are most pronounced). Seventy-two images were analyzed in all, and the range of detonations included airdropped detonations and tower-based detonations. Statistics were collected to determine the hit rate (sensitivity), precision and false positive rate. Fig. 32 shows an example of results for the Boltzmann detonation. The hit rate for all the detonations was measured at 71.95%, with a 86.03% precision and a 0.015% false positive rate. The false positive rate was extremely low
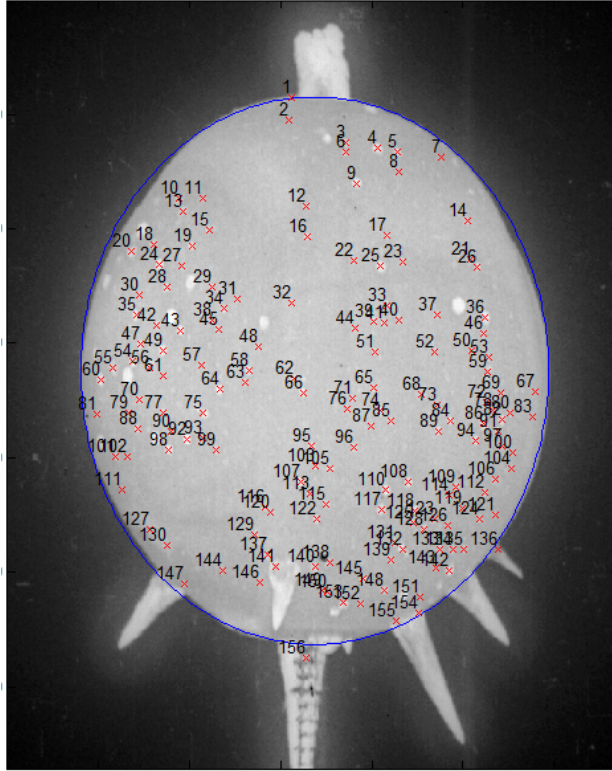
Figure 32. Results of hotspot detector for Boltzmann detonation. There were 141 true positive detections, 20 misses, and 15 false detections (1,67,83,111,120,127,129,130,136,141,146,151,154,155 and 156). Boundary of the detonation is highlighted in blue is the result of ellipse detection [39].

as influenced by the number of true negative pixels correctly identified. Hit rates were slightly lower than the smaller scale study discussed in Sec. 4.2 [23], precision was considerably higher, and the false positive rate was similar. The hit rates were likely lower because of the expansion to several detonations instead of just the one in the previous study. The precision improved because of added post-processing that removed small clusters, and non-rounded detections that were caused by folds or protrusions in the detonations which reduced the number of false positives increasing the precision rate.

V. Automated Hotspot Feature Matching

With an adequate hotspot detector from Chapter IV, the hotspots need to be matched across wide viewpoints. This chapter demonstrates that, using a spherical-based object model, hotspots can be described and matched across wide viewpoints of 58-110°, for multiple points in time and across multiple different detonations providing the means to model them in three spatial dimensions and temporally. Hotspots are matched to films from different viewpoints with 76.6% correctness and a σ of 16.4%. Hotspot descriptors are matched in time sequence with 99.6% correctness and a σ of 1.07%. This material appears in the Institute of Engineering and Technology (IET) Computer Vision Journal [25].

The rest of the chapter is organized as follows. An overall methodology of matching features is discussed in Sec. 5.1. Next, the processes used to align the films in time is discussed. Once the films are time-aligned, the frames are run through a hotspot detector to determine the pixel locations of the center of hotspots in the image. Next, the hotspots are described relative to their location within the larger detonation. Lastly, Matching hotspots from alternate viewpoints and in time sequence is discussed. The results are in Sec. 5.2 and the conclusion of the paper is in Sec. 5.3.

5.1 Methodology

Fig. 33 shows the steps in the hotspot matching technique. First, the frames are analyzed for timing markers and their timestamps for each frame are estimated and aligned (Chapter II). Next, hotspots are detected using a hotspot feature detector (Chapter IV). Each hotspot is then described by its relationship to the overall detonation and catalogued for the frame. The hotspots are then adjusted for viewpoint

angle or radial position to match different viewpoints or timestamps. Lastly, the hotspots are matched creating a feature correspondence that can be used to create 3D sparse point clouds or velocity vector fields. Each of these steps is discussed in detail.
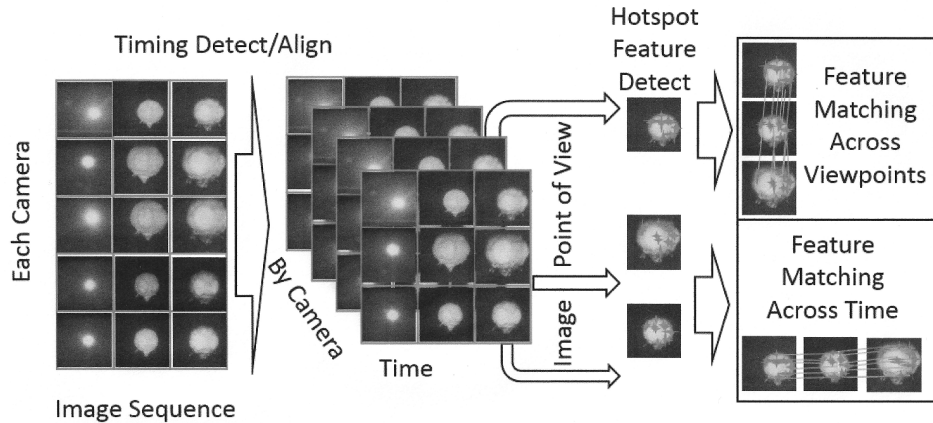
Figure 33. A flow chart of step-by-step processes resulting in hotspot feature correspondences from different viewpoints and points in time.

Hotspot Feature Descriptor.

The hotspot detector (Chapter IV) produces a catalogue of hotspots within an image. Once hotspots were detected and catalogued they were described with a feature descriptor. The feature descriptor is 13 values that describe the hotspots location relative to the larger detonation. A list of the values stored in the descriptor are:

1. Center of hotspot (y), horizontal-coordinate
2. Center of hotspot (z), vertical-coordinate
3. Center of hotspot (x), depth-coordinate
4. Width of hotspot, horizontal direction
5. Width of hotspot, vertical direction
6. Radius of detonation (a), horizontal direction

7. Radius of detonation (b), vertical direction

8. Inclination coordinate (θ) of hotspot relative to center of detonation

9. Azimuth coordinate (φ) of hotspot relative to center of detonation

10. Radius coordinate (r) of hotspot relative to center of detonation

11. Center of detonation (y_c), horizontal-coordinate

12. Center of detonation (z_c), vertical-coordinate

13. Number of pixels in hotspot

Several of the values (3, 6-12) are based on the overall detonation. To acquire that information, an ellipse detector [39] was applied to the detonation. The ellipse detection is highlighted in Fig. 32. Using the ellipse, an assumption is made that the detonation is an ellipsoid in 3D with equal depth and horizontal dimensions but potentially differing vertical dimensions. Using the location of the hotspot relative to the larger detonation, the horizontal and vertical coordinates are translated into polar coordinates. For polar coordinates, the reference frame assigned $\mathbf{z}$ to the vertical axis, $\mathbf{y}$ to the horizontal axis, and $\mathbf{x}$ to the depth axis. Eq. 6 through Eq. 9 show the equations for calculating the polar coordinates with a representing the radius of the larger detonation in the horizontal direction, and b representing the radius in the vertical direction. The center of the detonation is assumed to be at zero in the depth direction.

$$x = \sqrt{a^2 - (y - y_c)^2 - [\frac{a^2(z - z_c)^2}{b^2}]} \tag{6}$$

$$r = \sqrt{x^2 + (y - y_c)^2 + (z - z_c)^2} \tag{7}$$

$$\theta = cos^{-1}(\frac{z - z_c}{r}) \tag{8}$$

$$\varphi = tan^{-1}(\frac{y - y_c}{x}) \tag{9}$$
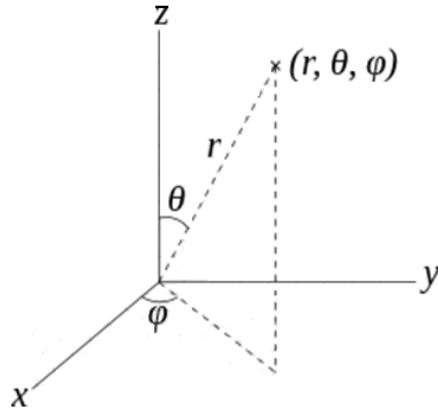
Figure 34. A depiction of 3-dimensional polar coordinates. Inclination angle from the vertical axis is θ. Azimuth angle from the depth axis(X-axis) is φ. The radius in the direction of θ and φ is r.

Feature Matching.

Once the hotspots features are described for an image they are matched to other viewpoints or points in time. To accomplish this, the second image (i.e. the image to be matched) is processed with the hotspot detector. To align the hotspots from different images, the descriptors are adjusted to account for the movement of hotspots between the images. Matching across viewpoints adjusts the θ and φ while matching in time sequence adjusts r.

Matching alternate viewpoints.

Matching across different viewpoints is accomplished by adjusting the azimuth angle (φ) from one of the viewpoints the same amount as the change in viewpoint angle. Using the survey sheets of each detonation and their recorded locations of collection sites and detonation sites, the angles between viewpoints were solved using trigonometry. In some cases, the elevation was different between collection sites also requiring a change in elevation angle (θ) of the descriptors. The radius (r) must also be adjusted proportionally for different focal lengths and distances from the camera to the detonation.

54

Once the hotspots are adjusted for azimuth angle, elevation angle, and radius they are matched as shown in Alg. 1. The first step in the matching process is to determine the potential bias that exists between the two frames. If the number of hotspots detected in the first frame is M, and the number of hotspots detected in the second frame is N, an $M \times N$ set of combinations is exhaustively compared to find all possible biases. For each $M \times N$ hotspot match, the differences between θ and φ are calculated and sorted descending. The combinations that have the least total θ and φ are then considered in order for matching, thus considering the smallest bias first. This is accomplished in the first double loop in Alg. 1.

Beginning with the smallest bias, the smaller group of hotspots is matched to the larger group. For this example, M will be assumed to be smaller than N. Each point (m_i) in the smallest group is matched in turn to the closest point in 3D space to a point in the larger group (n_j). A distance threshold is established to control how tight the matches are. It was found that a good threshold based on previous work with manual matches [26] yielded satisfactory results with the threshold set at the mean $+ 2\sigma$ of the distances of manual match statistics. If the distance calculated is less than the threshold then the match is kept. The point (n_j) that is matched is removed from future consideration for matching. The next point (m_{i+1}) is then matched to remaining points. While matching m_i with points in N, if no match is found that is less than the distance threshold then there is no match for m_i recorded and m_{i+1} is considered for matching. The iteration continues until all points in M have been considered for matching. The match correspondence, the total distance from all matched points, and the number of matches is recorded, and the next smallest bias is considered for all points. This process is repeated for the smallest 5% of biases, and the largest number of points, which minimize the total average distance that is kept as the best matching correspondence.

Algorithm 1: Hotspot matching algorithm.

Result: Matched correspondances between M and N hotspot sets.
$thresh = \bar{X} + 2\sigma$; (Stats of manual matches) $best\_dist = \infty$; $best\_num\_pts = 1$;
for $m\_bias = 1$ *to* $|M|$ **do**
    for $n = 1$ *to* $|N|$ **do**
        $bias\_phi(n) = \varphi(M(m\_bias)) - \varphi(N(n))$;
        $bias\_theta(n) = \theta(M(m\_bias)) - \theta(N(n))$;
        $bias\_total(n) = |bias\_phi(n)| + |bias\_theta(n)|$;
    end
end
Sort(N, $bias\_total$, ascending); // Sort the list of biases ascending
for $n\_bias = 1$ *to* $\lceil 0.05 \times |N| \rceil$ **do**
    Shift(N, $bias\_phi(n\_bias)$, $bias\_theta(n\_bias)$);
    for $m = 1$ *to* $|M|$ **do**
        for $n = 1$ *to* $|N|$ **do**
            $this\_dist(n) = distance(N(n), M(m))$;
        end
        Sort($this\_dist$, ascending); **if** $this\_dist(1) \leq thresh$ **then**
            $total\_dist = total\_dist + this\_dist(1)$; $matched(m, 1) = m$;
            $matched(m, 2) = unsorted\_index\_of(this\_dist(1))$;
        end
    end
    // Store a new best match if more points and less avg error
    if $|matched| \geq best\_num\_pts$ AND $\frac{total\_dist}{size(matched)} \leq \frac{best\_dist}{best\_num\_pts}$ **then**
        $best\_dist = total\_dist$; $best\_match = matched$;
        $best\_num\_pts = |matched|$;
    end
end
return $best\_match$

Matching in time sequence.

Matching in time sequence is less challenging as matching from the wide viewpoint angles. To match in time sequence, the azimuth and inclination values of the descriptor are the same, however the radius is increasing. The increase in the radius can be predicted using Taylor's equation shown in Eq. 1.

Assuming a constant yield for the given detonation, and a constant density, the equation can be arranged where $t^2 \sim R^5$. The time since detonation can then predict

the radius, and a Δt in small increments in t can be used to find a ΔR. Since the time since detonation is already estimated (see Sec. 2.4), it can be used to predict the change in radius from frame to frame.

The algorithm for matching in time sequence works exactly like that of matching alternate viewpoints (Alg. 1). The difference is the inputs are the hotspots from the original frame, adjusted by the ΔR and the hotspots from next frame in time sequence. The hotspots are only adjusted in radius, and not in azimuth (φ) or inclination (θ).

5.2   Results

At the time of testing, only twelve films were digitized and available for testing. Four of the twelve films did not show discernible hotspots. Of the eight remaining films, six had multiple films from the same viewpoints, which significantly increased the number of time aligned frames making them more useful for testing. The accuracy of matching alternate viewpoints was tested using the six detonations listed in Table 11. The accuracy was determined by verifying the correctness of each matched correspondence by visual inspection. Since the model that is used to describe and rotate hotspots is based on polar coordinates, the airdrop detonations were expected to perform better because they are more spherical, and have fewer disparities with that model. The tower detonations were included to challenge the model to see how accurate matching would be with non-elliptical shaped detonations and detonations with cone protrusions. The detonations listed in Table 11 are ordered from most spherical to least spherical. A variety of viewpoint angles were tested ranging from 58° to almost 110°.

Table 11. Detonations tested for viewpoints.

Detonation	ΔViewpoint angle	ΔElevation angle	Type
Climax	68.46°	0°	Airdrop
Grable	57.6°	0°	Airdrop
Boltzmann	109.5°	2°	Tower
MET	67.46°	0°	Tower
Turk	84.25°	3°	Tower
Tesla	71.48°	0°	Tower

Table 12. Viewpoint matching algorithm results.

Detonation	Avg. Correct Matches	σ Correct Matches	Avg. Num. Points	σ Num. Points	Type
Climax	82.6%	8.77%	45.6	14.54	Airdrop
Grable	92.5%	3.80%	58.23	9.32	Airdrop
Airdrop summary	86.75%	13.22%	52.5	13.5	
Boltzmann	68.28%	12.23%	19.6	5.1	Tower
MET	62.71%	17.65%	25.7	7.3	Tower
Turk	84.05%	14.69%	9.6	4.2	Tower
Tesla	66.23%	10.44%	28.4	20.2	Tower
Tower Summary	70.73%	16.17%	20.5	13.3	
All 6 detonations	76.63%	16.37%	31.6	20.2	
All 6 NUDETs SIFT	1.51%	8.20%	6.83	7.97	
All 6 NUDETs SURF	0.45%	1.85%	16.71	5.54	

Matched Viewpoint Results.

For each detonation, films from alternate viewpoints were time aligned and hotspot detection performed. Then matching was tested to determine how many of the matches were correct. Matching was done at several points in time in the detonation. Thirty matches were accomplished for each detonation. The results in Table 12 summarize the hotspot testing and a comparison with SIFT and SURF with a pictorial representation of the matching for Grable detonation (Fig. 35).

The hotspot descriptor and matching outperfoms both SIFT and SURF, most
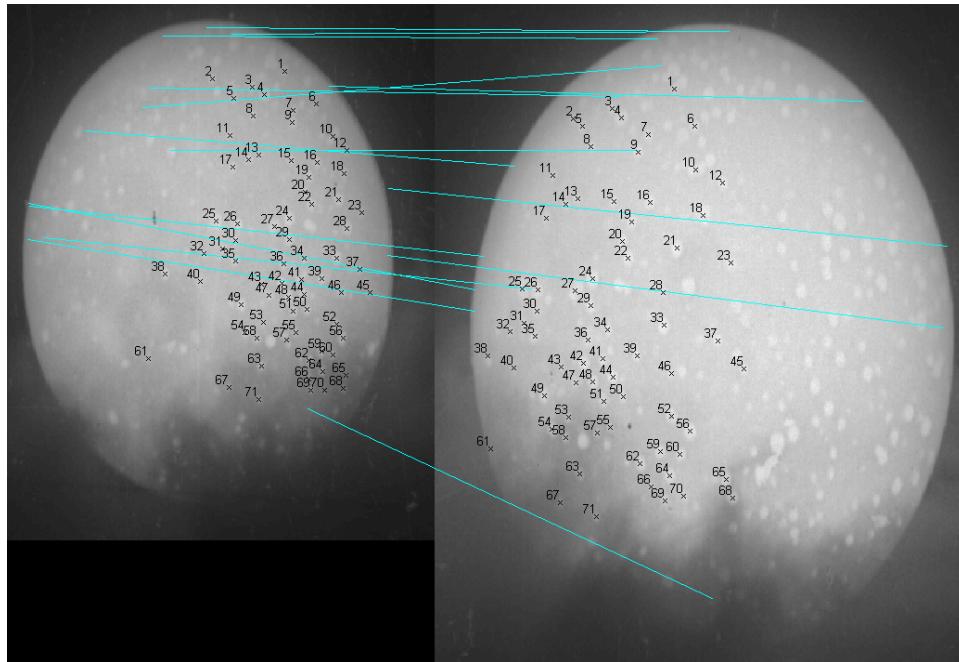
Figure 35. Results of viewpoint matching for hotspots are x's in the Grable detonation. There were 68 correct matches, and 3 incorrect matches (2, 28, 61). SURF matches are shown with lines with none of them being correct.

likely because the viewpoint angles are outside the viewpoint matching capabilities of those feature descriptors. As expected, the more spherical airdrop detonations performed better than the tower detonations because they conform more closely to the ellipsoid model inherent in the hotspot descriptor. This is evidenced by the higher average percentage of correct matches and the higher average number of matches. The high percentage of correct matches for the Turk detonation appears to stand out amongst the other tower detonations, but combined with the evidence of considerably fewer number of matches leads to the conclusion that the threshold for acceptance of a good match was likely too tight for that detonation. It does demonstrate that if more precise results are desired for a particular detonation, that a threshold can be adjusted to either increase the number of matches at the cost of them being correct or decrease the number of matches to improve the likelihood that they are correct. Individual tailoring can be accomplished for each detonation if it is desired. Overall, the results

are good as the percentage of correct matches is greater than 50%, thus opening the door to robust estimation approaches such as RANSAC [5] to remove outliers from the majority. The number of matches in most cases is also sufficient to attempt to estimate 3D positions and fit volume models (e.g. sphere, ellipsoid, others) to the 3D point cloud reconstruction that can be generated from these matched correspondence results.

Matched in Time Sequence Results.

A similar test as with viewpoint matching was run for time matching for the same six detonations and thirty frames per detonation. Table 13 shows the quantitative results and Fig. 36 shows a pictorial representation of the matching for the Turk detonation. The results show that the time matching is very accurate with 99.61% correct matches for all the detonations and a σ of 1.07%. SURF has similar capabilities with 98.67% correct matches with a σ of 1.07% while SIFT was correct 92.63% of the time with a σ of 12.42%. The hotspot detection and matching performs slightly better than the state-of-the-art techniques but without statistical significance.
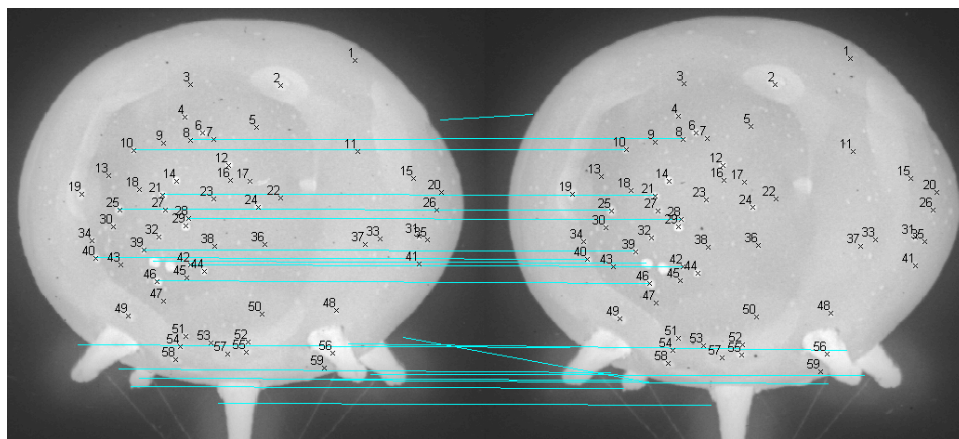
Figure 36. Results of time sequence matching for hotspots in the Turk detonation. The numbered x's are the hotspot matching results and the corresponding lines are SIFT matches. All matches for the hotspot matching were correct, while the SIFT matching has two mismatches and eighteen correct matches.

60

Table 13. Time Matching algorithm results.

Detonation	Avg. Correct Matches	σ Correct Matches	Avg. Num. matches	σ Num. Matches	Type
Climax	99.96%	0.20%	45.2	29.1	Airdrop
Grable	99.93%	0.21%	123.0	40.7	Airdrop
Airdrop summary	99.95%	0.20%	84.1	52.6	
Boltzmann	99.4%	0.80%	82.5	23.8	Tower
MET	99.89%	0.43%	52.7	10.4	Tower
Turk	99.74%	0.73%	46.5	19.4	Tower
Tesla	98.73%	2.11%	61.2	31.7	Tower
Tower Summary	99.44%	1.27%	60.7	26.2	
All 6 detonations	99.61%	1.07%	68.5	38.6	
All 6 NUDETs SIFT	92.63%	12.42%	17.87	15.06	
All 6 NUDETs SURF	98.67%	1.07%	174.1	66.34	

5.3   Conclusion

This chapter demonstrates a method to describe and match features from video of nuclear detonations with films traveling at different speeds and at wide viewpoints to enable 3D point cloud reconstruction and a volume-based nuclear yield model. A volume-based model requires feature correspondences, and the viewpoints are wider than SIFT-based techniques can match. The technique employed detects hotspot features and matches them across wide viewpoints using a spherical-based object model. Using a spherical object model, hotspots are described using their location relative to the overall detonation described in polar coordinates. Hotspot descriptors are then matched to films from different viewpoints with 76.6% correctness and a σ of 16.4%. Hotspot descriptors are also matched in time sequence with 99.6% correctness and a σ of 1.07%. These results demonstrate an automated feature detection, description, and matching combination that enables the matching of features from unsynchronized video across wide viewpoints of 58-110° where an automated process was before unavailable.

This chapter demonstrates that a spherical model can be used effectively as the basis for a feature descriptor for ellipsoid-like objects. This allows the comparison across wider viewpoints without the need of Harris [7] corners.

Next, the matched correspondences were used to generate 3D point clouds of differing viewpoints and tracking them through time. The discussion about how accurate the points in the point cloud continues in Chapter VI. Point locations were tracked in time as well as volumes inferred from the point clouds. The discussion about volumes continues in Chapter VII.

VI. Quantifying Accuracy of 3D Points Clouds

To evaluate the accuracy of the state-of-the-art multi-view geometry (MVG) methods for the NUDET domain relative to ground truth, multi-view geometry theory is applied to atmospheric nuclear tests films to estimate the three-dimensional locations of fixed structures and the radiological material during the detonation. The result is a quantitative measurement of how accurate the MVG methods are in the NUDET domain.

This chapter presents a MVG method that estimates the location of 3D points in atmospheric nuclear detonations films. To accomplish this, corresponding points were manually identified in three detonations at three different points in time on the support tower (Fig. 37) that the nuclear device was placed on. The corresponding points in multiple films and viewpoints were used to estimate the location of points in 3D-space using multi-view geometry theory [8]. The reconstructed points of the tower were then compared to the ground truth of the tower's location and dimensions to determine the reconstructive error otherwise known as the uncertainty of the points in space. This error was then inferred on other points in the reconstruction of the detonation where the ground truth is not known. A total of 69 reconstructions were built to collect the statistical error. The end result is the ability to estimate, with an average locational error of 0.62 meters with 0.35, 0.24, and 0.34 meters of locational error in x-, y-, and z-directions respectively, the position of radiological material during the detonation and post-detonation in the plume. This material appears in the American Nuclear Society's Journal of Nuclear Science and Engineering [26].

This chapter is organized in the following manner. Sec. 6.1 describes the MVG methods of 3D reconstruction and homography that are used to build the reconstructions. Sec. 6.2 discusses the methodology that is used to determine the error from ground truth and how homography is applied to the images. Sec. 6.3 presents the
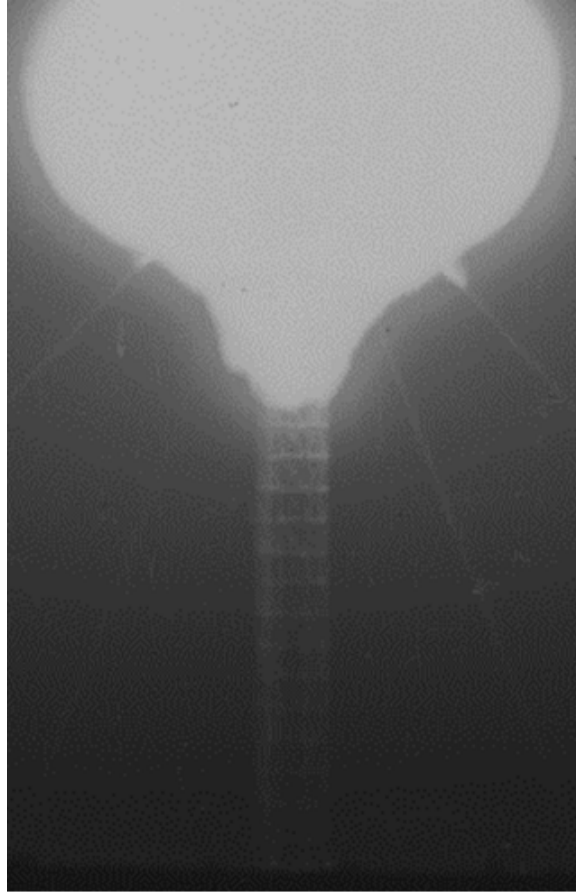
Figure 37.   An example NUDET image of Tesla detonation with tower visible below the detonation [30].

results with some discussion in Sec. 6.4 and conclusions in Sec. 6.5.

6.1   Background

This section describes the camera models and the processes of 3D reconstruction from images using triangulation and bundle adjustment. It also describes the process of registering images using homography.

Homogeneous coordinates.

In MVG, homogeneous coordinates are used so that points in the real world can be related to points in multiple images more easily [8]. A point in Euclidean 3-space is represented by an ordered pair of real numbers (x, y, z). To make the coordinate homogeneous, a fourth digit is added to create the homogeneous coordinate definition that $(x, y, z) = (x, y, z, 1)$. The definition also implies that $(x, y, z) = (x, y, z, 1) = (2x, 2y, 2z, 2) = (kx, ky, kz, k)$ for any non-zero value of k. The parameter k is then sometimes referred to as a scaling factor that facilities relating images together that have different scale.

Furthermore, we can use homogeneous coordinates to then define projective space. The Euclidean space $\mathbb{R}^n$ can be extended to projective space $\mathbb{P}^n$ by representing points as homogeneous vectors [8].

Camera Models.

To apply multi-view geometry to the NUDET films, information recorded at the time of detonation is interpreted using camera models. This section details the theory of the pinhole camera, which underpins the finite projective camera model. The finite projective camera is then used in Sec. 6.2 with information from the NUDET films with triangulation and bundle adjustment to create the 3D structure of the NUDET with points on the NUDET tower.

Pinhole Camera.

The pinhole camera model is a basic model of how images are captured by a camera. Fig. 38 shows a depiction of the pinhole camera model. Letting $\mathbf{X}$ represent a point in the 3-dimensional world represented by $\mathbf{X} = (X, Y, Z)^T \in \mathbb{R}^3$ in Euclidean space. The camera center (optical center), C is located at the origin of this Euclidean
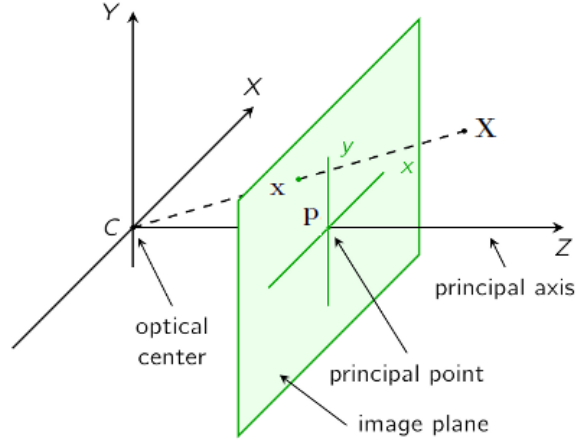
Figure 38. **The pinhole camera model.**

space. The image plane representing the image is in the positive Z direction. The principal axis intersects the image plane in the center of the image at point $\boldsymbol{p}_0$. The image plane has an $x-$ and $y-$axis orthogonal to each other and the principal axis. Point $\mathbf{X}$ is then projected on the image plane at point $\mathbf{x}$ which is on a ray from optical center C toward point $\mathbf{X}$.

Represented in homogeneous coordinates, $\mathbf{X} = (X, Y, Z)^T = (fX/Z, fY/Z, f)^T$ where f is the focal length of the image. Another way to consider this is the captured 2D image of the 3D world is a transform from $\mathbb{R}^3 \mapsto \mathbb{R}^2$ which can also be written as a matrix multiplication in Eq. 10.

$$\begin{pmatrix} X \\ Y \\ Z \\ 1 \end{pmatrix} \mapsto \begin{pmatrix} fX \\ fY \\ Z \end{pmatrix} = \begin{bmatrix} f & & & 0 \\ & f & & 0 \\ & & 1 & 0 \end{bmatrix} \begin{pmatrix} X \\ Y \\ Z \\ 1 \end{pmatrix} \tag{10}$$

Now, the bracket matrix in Eq. 10 is given a name, $\mathbf{P}$, to represent the 3×4 camera projection matrix. With $\mathbf{x}$ representing the 2D image point, and $\mathbf{X}$ representing the

3D world point, the equation is then defined as in Eq. 11.

$$\mathbf{x} = \mathbf{PX} \tag{11}$$

The expression in Eq. 10 assumes that the origin of the image plane is the principal point ($\mathbf{p_0}$), which may not always be the case. As a result, it is generalized that a shift (translation) can occur to set the principal point in the middle resulting in the mapping

$$(X, Y, Z)^T \mapsto (fX/Z + p_x, fY/Z + p_y)^T$$

where (p_x, p_y) is the coordinates of the principal point. The resulting change to Eq. 10 is then expressed in Eq. 12.

$$\begin{pmatrix} X \\ Y \\ Z \\ 1 \end{pmatrix} \mapsto \begin{pmatrix} fX + Zp_x \\ fY + Zp_y \\ Z \end{pmatrix} = \begin{bmatrix} f & & p_x & 0 \\ & f & p_y & 0 \\ & & 1 & 0 \end{bmatrix} \begin{pmatrix} X \\ Y \\ Z \\ 1 \end{pmatrix} \tag{12}$$

Next, the camera calibration matrix ($\mathbf{K}$) is established where

$$\mathbf{K} = \begin{bmatrix} f & & p_x \\ & f & p_y \\ & & 1 \end{bmatrix}. \tag{13}$$

Eq. 10 can be rewritten as shown in Eq. 14 as the definition of $\mathbf{P}$ is expanded since $\mathbf{P} = \mathbf{K}[\mathbf{I}|\mathbf{0}]$. In this case, $\mathbf{I}$ is the identity matrix and $\mathbf{0}$ is the zero vector as the last column in the $\mathbf{P}$ matrix. $\mathbf{X}_{cam}$ is the same $\mathbf{X}$ in world coordinates with the emphasis that it is expressed in the camera coordinate frame. The difference between $\mathbf{X}_{cam}$ and $\mathbf{X}$ is the orientation of the camera which can be defined in terms of rotation and
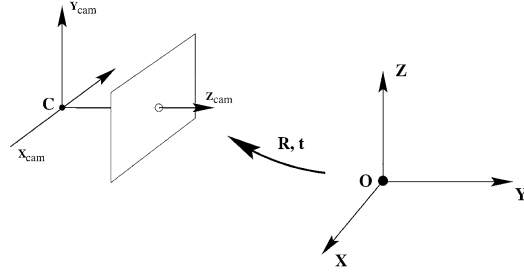
Figure 39. **The Euclidean transformation between world and camera coordinate frames is comprised of rotation (R) and translation (t) [8].**

translation. When the $\mathbf{K}$ matrix of a camera is known, it is said to be calibrated.

$$\mathbf{x} = \mathbf{K}[\mathbf{I}|\mathbf{0}]\mathbf{X}_{cam} \tag{14}$$

Rotation and Translation.

Fig. 39 shows the transformation from $\mathbf{X}_{cam}$ to $\mathbf{X}$ world coordinates. Letting $\tilde{\mathbf{X}}$ represent a 3-vector of the coordinates of a point in the world coordinate frame, and $\tilde{\mathbf{X}}_{cam}$ represent that point in the camera coordinate frame, the relationship $\tilde{\mathbf{X}}_{cam} = \mathbf{R}(\tilde{\mathbf{X}} - \tilde{\mathbf{C}})$ is asserted where $\tilde{\mathbf{C}}$ is the coordinates of the camera center in the world coordinate frame. $\mathbf{R}$ is then a 3×3 rotation matrix. This relationship can be stated verbosely as in Eq. 15, or concisely as in Eq. 16.

$$\mathbf{X}_{cam} = \begin{bmatrix} \mathbf{R} & -\mathbf{R}\tilde{\mathbf{C}} \\ 0 & 1 \end{bmatrix} \begin{pmatrix} X \\ Y \\ Z \\ 1 \end{pmatrix} = \begin{bmatrix} \mathbf{R} & -\mathbf{R}\tilde{\mathbf{C}} \\ 0 & 1 \end{bmatrix} \mathbf{X} \tag{15}$$

$$\mathbf{x} = \mathbf{K}\mathbf{R}[\mathbf{I}|\tilde{\mathbf{C}}]\mathbf{X} \tag{16}$$

It is also apparent that the definition of $\mathbf{P}$ has expanded where $\mathbf{P} = \mathbf{K}\mathbf{R}[\mathbf{I}|\tilde{\mathbf{C}}]$.

Looking inside of $\mathbf{P}$ we can see that it has 9 degrees of freedom: 3 for elements in $\mathbf{K}$ (f, p_x, p_y), 3 for $\mathbf{R}$, and 3 for $\tilde{\mathbf{C}}$. $\mathbf{K}$ values are determined by the camera and are referred to as internal camera parameters or intrinsics, while $\mathbf{R}$ and $\tilde{\mathbf{C}}$ refer to the camera's orientation and position in the world coordinate system and are referred to as the external parameters or extrinsics.

CCD camera model.

The CCD (Charged Coupled Device) camera is an extension from the pinhole camera that allows for different scales in each axial direction. The CCD camera model applies to the digitized images of the NUDET data because the images are digitized using a scanner that interprets information like a CCD camera. With image coordinates often measured in pixels, this can have the effect of unequal scale factors in each direction. As a result, it is necessary to expand the pinhole model. If the number of pixels per unit distance in image coordinates are m_x and m_y in the x and y directions, then the transformation from world coordinates to pixel coordinates is found by multiplying by a factor of $\text{diag}(m_x, m_y, 1)$. This changes the formula for the camera intrinsics ($\mathbf{K}$) as shown in Eq. 17. The new values are defined in the following manner: $\alpha_x = fm_x$, $\alpha_y = fm_y$, $x_0 = m_x p_x$, and $y_0 = m_y p_y$.

$$
\mathbf{K} = \begin{bmatrix} \alpha_x & & x_0 \\ & \alpha_y & y_0 \\ & & 1 \end{bmatrix}
\tag{17}
$$

Finite projective camera.

Further generalizing the CCD camera, the parameter s for skew can be added to the CCD model for camera intrinsics.

$$\mathbf{K} = \begin{bmatrix} \alpha_x & s & x_0 \\ & \alpha_y & y_0 \\ & & 1 \end{bmatrix} \qquad (18)$$

In most cases s is zero for normal cameras. The cases where $s \neq 0$ occur when pixel elements are skewed in the CCD array. This can occur with the $x-$ and $y-$axis are not perpendicular. It can also occur when an image is taken of an image, like when a photograph is re-photographed, or a negative of an image is enlarged.

Triangulation.

Triangulation is the process of determining a point's 3D position from a set of corresponding image locations and known camera positions. Two processes are described here, the mid-point method and the direct linear transform method. These methods, as well as other methods, are discussed and compared in [9].

Mid-point Method.

Fig. 40 shows a diagram of the triangulation point estimation [34]. For a given image, $\mathbf{R}$ represents the rotational matrix of the image pose, $\mathbf{c}$ represents the camera center, $\mathbf{x}$ represents the 2D image location of the feature, $\hat{\mathbf{v}}$ is the direction of the ray from $\mathbf{c}$ to $\mathbf{x}$, and finally $\mathbf{q}$ is the point along $\hat{\mathbf{v}}$ that is closest to $\mathbf{p}$ and is d distance away from $\mathbf{x}$. Assuming that there are i cameras that have correspondence matches for feature $\mathbf{x}$, results in a set of $\mathbf{x}_i$ for that feature. Based on the discussion in Sec. 6.1, there is then a set of cameras $\mathbf{P}_i = \mathbf{K}_i[\mathbf{R}_i|\mathbf{t}_i]$, where $\mathbf{t}_i = -\mathbf{R}_i\mathbf{c}_i$ and $\mathbf{c}_i$ is the i-th
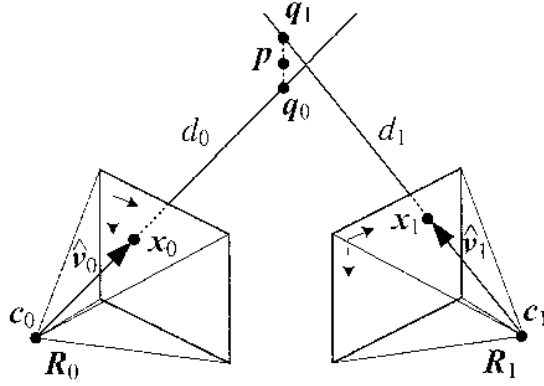
Figure 40. 3D point triangulation [34]. Point p is estimated using rays traced from the centers of camera at $R_1 c_1$ and $R_2 c_2$.

camera center. In Fig. 40, the rays originate at $\mathbf{c}_i$ in the direction $\hat{\mathbf{v}}_i = N(\mathbf{R}_i^{-1}\mathbf{K}_i^{-1}\mathbf{x}_i)$ where N represents the unit norm function. The nearest point to $\mathbf{p}$ on the ray is $\mathbf{q}_i$ which exists at $\|\mathbf{c}_i + d_i\hat{\mathbf{v}}_i - \mathbf{p}\|^2$ where d_i is the geometric distance and therefore has a minimum at $d_i = \hat{\mathbf{v}}_i \cdot (\mathbf{p}\text{-}\mathbf{c}_i)$. It follows that

$$\boldsymbol{q}_i = \boldsymbol{c}_i + (\hat{\boldsymbol{v}}_i\hat{\boldsymbol{v}}_i^T)(\boldsymbol{p} - \boldsymbol{c}_i) = \boldsymbol{c}_i + (\boldsymbol{p} - \boldsymbol{c}_i)_{\parallel},$$

and the squared distance (r_j^2) between $\mathbf{p}$ and $\mathbf{q}_i$ is

$$r_i^2 = \|(\boldsymbol{I} - \hat{\boldsymbol{v}}_i\hat{\boldsymbol{v}}_i^T)(\boldsymbol{p} - \boldsymbol{c}_i)\|^2 = \|(\boldsymbol{p} - \boldsymbol{c}_i)_{\perp}\|^2.$$

The optimal value for $\mathbf{p}$, is computed as a regular least squares problem by summing over all the r_i^2 and finding the optimal $\mathbf{p}$ using Eq. 19.

$$\mathbf{p} = \left[\sum_i (\boldsymbol{I} - \hat{\boldsymbol{v}}_i\hat{\boldsymbol{v}}_i^T)\right]^{-1}\left[\sum_i (\boldsymbol{I} - \hat{\boldsymbol{v}}_i\hat{\boldsymbol{v}}_i^T)\boldsymbol{c}_i\right] \tag{19}$$

While the mid-point method is straight-forward to comprehend, it is just one method of triangulation and is criticized for being inaccurate [9]. The direct linear

transform method is considered to be more statistically optimal [34] and is discussed next.

Direct Linear Transform method.

Consider two images $\mathbf{x}$ and $\mathbf{x}'$ and their camera matrices $\mathbf{P}$ and $\mathbf{P}'$. Written in homogeneous coordinates, $\mathbf{x} = w(x, y, 1)^T$ where (x, y) are observed point coordinates and w is an unknown scale factor. We also have the case by Eq. 10 where $\mathbf{x} = \mathbf{PX}$ and $\mathbf{x}' = \mathbf{P}'\mathbf{X}$. Calling $\mathbf{p}^{iT}$ the rows of $\mathbf{P}$, then $\mathbf{x} = \mathbf{PX}$ can be rewritten as

$$wx = \mathbf{p}^{1T}\mathbf{X}, wy = \mathbf{p}^{2T}\mathbf{X}, w = \mathbf{p}^{3T}\mathbf{X}.$$

Using the third equation, the value of w is substituted in the first two equations arriving at

$$\begin{aligned} x\mathbf{p}^{3T}\mathbf{X} &= \mathbf{p}^{1T}\mathbf{X} \\ y\mathbf{p}^{3T}\mathbf{X} &= \mathbf{p}^{2T}\mathbf{X}. \end{aligned} \tag{20}$$

Repeating this for $\mathbf{x}' = \mathbf{P}'\mathbf{X}$ similar equations are arrived at for $\mathbf{x}'$ and $\mathbf{P}'$

$$\begin{aligned} x'\mathbf{p}'^{3T}\mathbf{X} &= \mathbf{p}'^{1T}\mathbf{X} \\ y'\mathbf{p}'^{3T}\mathbf{X} &= \mathbf{p}'^{2T}\mathbf{X}. \end{aligned} \tag{21}$$

Eq. 20 and 21 are then solved for 0 arriving at

$$x(\mathbf{p}^{3T}\mathbf{X}) - (\mathbf{p}^{1T}\mathbf{X}) = 0$$

$$y(\mathbf{p}^{3T}\mathbf{X}) - (\mathbf{p}^{2T}\mathbf{X}) = 0$$

$$x'(\mathbf{p}'^{3T}\mathbf{X}) - (\mathbf{p}'^{1T}\mathbf{X}) = 0$$

$$y'(\mathbf{p'}^{3T}\mathbf{X}) - (\mathbf{p'}^{2T}\mathbf{X}) = 0.$$

These equations can be combined into a form $\mathbf{AX} = \mathbf{0}$ by factoring out $\mathbf{X}$ with $\mathbf{A}$ shown in Eq. 22 [9].

$$\mathbf{A} = \begin{bmatrix} x\mathbf{p}^{3T} - \mathbf{p}^{1T} \\ y\mathbf{p}^{3T} - \mathbf{p}^{2T} \\ x'\mathbf{p'}^{3T} - \mathbf{p'}^{1T} \\ y'\mathbf{p'}^{3T} - \mathbf{p'}^{2T} \end{bmatrix} \tag{22}$$

This solution of equations can be solved using Singular Value Decomposition that relates to the smallest singular value of $\mathbf{A}$. The solution to $\mathbf{A}$ with known $\mathbf{P}$ then gives the 3D points in $\mathbf{X}$.

Bundle Adjustment.

Bundle adjustment is an accurate way to recover structure and motion simultaneously for a three-dimensional reconstruction [34]. Bundle adjustment achieves these improvements by simultaneously calculating structure and camera poses. It can also scale for large data sets of tens of thousands of images [29].

Bundle adjustment performs the 3D triangulation from a set of three-dimensional points $\mathbf{X}_j$ which is in view by a set of cameras with matrices $\mathbf{P}^i$. Denoting $\mathbf{x}_j^i$ as the coordinates of the j-th point seen by the i-th camera. By Eq. 10, $\mathbf{P}^i\mathbf{X}_j = \mathbf{x}_j^i$ is stated. If measurements in the image are noisy then it is not likely that $\mathbf{P}^i\mathbf{X}_j = \mathbf{x}_j^i$ has an exact solution.

A Maximum Likelihood solution is then sought after assuming the noise is Gaussian with the goal of estimating projection matrices $\hat{\mathbf{P}}^i$ and points $\hat{\mathbf{X}}_j$ which project exactly to the image points $\hat{\mathbf{x}}_j^i$ which also minimizes the distance between the reprojected point and measured image points $\mathbf{x}_j^i$ for every view in which the point appears. The reprojection used in Eq. 23 [8] where $d(\mathbf{x}, \mathbf{y})$ is the geometric image distance

between homogeneous points $\mathbf{x}$ and $\mathbf{y}$.

$$\min_{\hat{\mathbf{P}}^i, \hat{\mathbf{X}}_j} \sum_{ij} d(\hat{\mathbf{P}}^i \hat{\mathbf{X}}_j, \hat{\mathbf{x}}_j^i)^2 \tag{23}$$

Minimizing the reprojection error is not without uncertainty. Past work [19] [35] has narrowed the uncertainty to be associated with the 3D depth of a scene and the camera motion. While bundle adjustment can be used without knowing the locations of cameras, the uncertainty is minimized when the initial estimate of camera positions is as correct as possible. Using the recorded camera positions in the NUDET films as initial camera pose positions, minimizes the negative effect of improper initialization which is the largest contributor to uncertainty in reconstructions. From the initial pose projection, the structure and pose parameters are then improved iteratively with bundle adjustment using the multiple point correspondences. To accomplish bundle adjustment, existing software packages are available [37].

2D Homography and Image Registration.

A homography is the relationship between two planar surfaces. Homography is used to relate two images, which are planar surfaces, of the same subjects. A common use of homography is then registering images to one another. Defined mathematically, given a set of points $\mathbf{x}$ in the projective space $\mathbb{P}^2$ and a corresponding set of points $\mathbf{x}'$ in $\mathbb{P}^2$ the relationship $\mathbf{x} \leftrightarrow \mathbf{x}'$ is represented by a 3×3 matrix $\mathbf{H}$ such that $\mathbf{H}\mathbf{x} = \mathbf{x}'$. Given a set of corresponding points $\mathbf{x} \leftrightarrow \mathbf{x}'$, $\mathbf{H}$ can be solved for using the direct linear transform method that was discussed in Section 6.1 using $\mathbf{H}$ instead of $\mathbf{P}$.

To use the homography relationship to register images requires a set of corresponding points. When points are not known a priori, corresponding points are discovered using feature descriptors and matching algorithms like SIFT [15] or Speeded-Up Robust Features (SURF) [2]. While viewpoint angles across points of view are too

large to have reliable matched repeatability within the same point of view, angles are near zero and past work [28] has demonstrated that automated methods do work effectively.

6.2   Methodology

The determination of the uncertainty of points in 3D space generated from triangulation and bundle adjustment using the NUDET films provides a baseline by which other three-dimensional models of the detonation can be measured. To accomplish this, two reconstructions were generated for each combination of two points of view. One reconstruction used the triangulation method that solved for 3D points using singular value decomposition as described in Sec. 6.1. The second reconstruction was run through a bundle adjustment algorithm to refine the camera intrinsics and extrinsics and create a bundle adjusted reconstruction.

To quantify the error, 3D reconstructions were accomplished on tower detonations. Points were manually selected to be on different floors of the tower. The locations and size of the towers was known, so the reconstruction was compared to ground truth. The error was then the difference between the reconstructed point and the ground truth.

Ground truth was established by the survey sheets of the detonation which depicted ground zero within a foot's accuracy. Total tower height was also known for each detonation (Table 14), and by counting the number of floors, the height per floor was determined for each detonation. The width of the tower was documented as well. Once the reconstruction was complete, the reconstruction was rotated to match that of the ground truth. Each reconstruction yielded ten points on the tower that were used to calculate the error as the differences between the point and the ground truth. In addition to the total distance, the distance in x, y, and z dimensions was

Table 14. Height of tower detonations [30].

Detonation	Tower Height (ft)	Floors
Tesla	308	25
Turk	508	35
MET	408	30

calculated. The mean and variance was then calculated from the collection of points for all the reconstructions. The process was repeated three times for three different points in time on each detonation.

Applying Homography.

In addition to reconstructions using triangulation and bundle adjustment, reconstructions were also created using homography to register images from the same point of view. Considering the locations of cameras within a collection site (Fig. 3), it was unknown which films correspond to which positions of the camera racks, and that could be a source of error that could be reduced using homography to register the images from the same point of view. Fig. 41 shows a flow chart of how applying homography to register images from the same point of view is applied. Each point of view is taken separately and homography matrices are determined using SURF features. The manual point correspondences are then transformed using the homography relationship to one coordinate system where they are averaged together. The averaging reduces any human error from the manual points. The result of the averaged points is then transformed back to the original film coordinates. The process is repeated for the second point of view. The pairwise comparison across points of view then occurs exactly as if the homography registration did not occur and triangulation and bundle adjustment reconstructions are created. The end result is an ability to
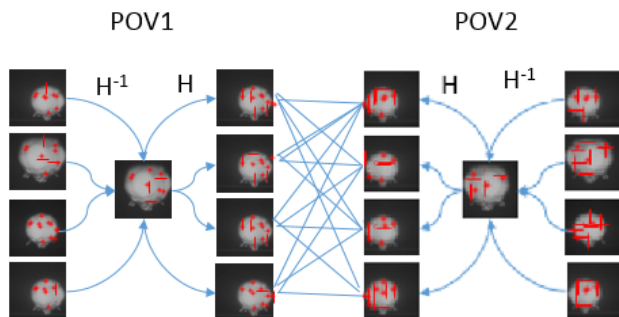
Figure 41. Applying homography to register images prior to pairwise comparison. Each point of view uses SURF derived correspondences to calculate H. The manual points are then transformed to one coordinate system and averaged. The average is then transformed back into the original coordinate systems and are then compared pairwise and measured with triangulation and bundle adjustment with the alternate point of view.

compare the process of homography both with triangulation and bundle adjustment to see if applying homography to either of those processes further reduces the error.

Workload.

The requirements for the workload for this test were that the films had to be of a tower detonation, with multiple camera angles, and have already been digitized. At the time of testing for this project, six detonations met this criteria, three from Operation Teapot (Tesla, Turk, and MET), and three from Operation Plumbbob (Boltzmann, Galileo, Kepler). The number of films and potential reconstructions of the films are shown in Table 15. To select the source data for this experiment, the digitized films and viewpoints were analyzed. Reliable matching tower correspondences could not be found in Boltzmann because of the 110° viewpoint change between points of view. Detonations Tesla, Turk, and MET were chosen because of the larger number of films and combinations of reconstructions that could be made. By selecting these three detonations, 77% of the available reconstructions were tested on 65% of the available films. With the workload chosen as three detonations (Tesla, Turk, and MET), at three different points in time, all available films were tested pair-wise across

Table 15. Available digitized tower detonations [30].

Operation	Detonation	Films Loc. 1	Films Loc. 2	Num. Recon-str.
Teapot	Tesla	3	3	9
Teapot	Turk	2	5	10
Teapot	MET	2	2	4
Plumbbob	Boltzmann	2	2	4
Plumbbob	Galileo	1	2	2
Plumbbob	Kepler	1	1	1

two locations for a total of 69 ($Tesla(9) + Turk(10) + MET(4)) \times 3\ timestamps$) tests accomplished for both triangulation and bundle adjustment. Applying homography to the process creates another 69 tests for both triangulation and bundle adjustment with homography.

Estimating Camera Intrinsics (K).

To apply triangulation and bundle adjustment, the films must be calibrated using the information that was documented when they were recorded. To calculate the camera intrinsic values (**K**) for the NUDET data, each of the parameters of **K** must be determined. To accomplish this the CCD model described in Sec. 6.1 was used and the size of the physical films were analyzed. Details of this process and its results can be found in Appendix A.

6.3 Results

Fig. 42 shows one example of manual point correspondences between two images of Tesla which has a 72° angle between viewpoints. This can be compared to the reconstruction shown in Fig. 43. The number of points on the tower were similar to the number of points on the detonation. This was deliberate so the reconstruction

would be equally weighted by both points on the tower and on the detonation. The points that were chosen on the detonation were chosen for their ability to be accurately matched from alternate points of view, and provided a variety of features including bright spots, folds in the detonation, and endpoints of cone protrusions.
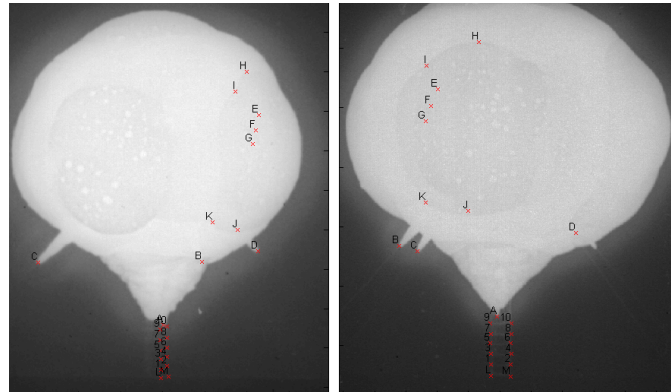
Figure 42. Matched correspondences of Film 04 with Film 10 of Tesla.
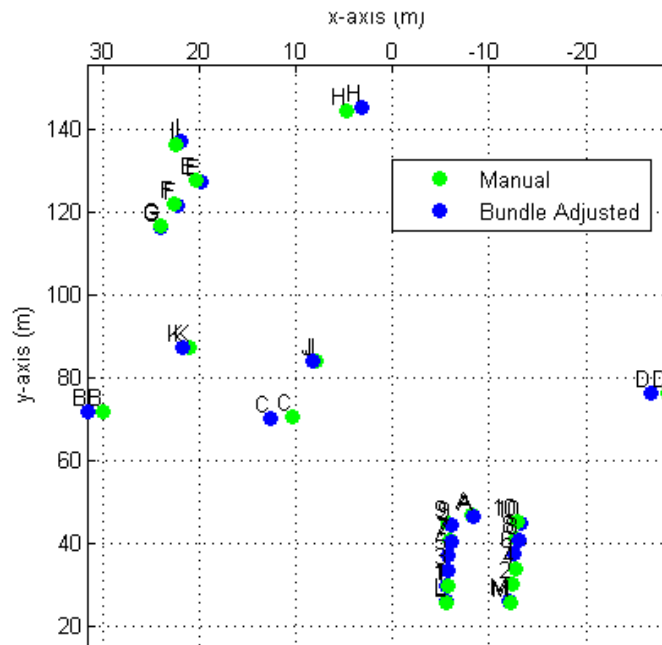
Figure 43. 3D Reconstruction of Film 04 with Film 10 of Tesla.

Ten points were reconstructed of the tower for each triangulation and bundle adjusted reconstruction. Each point was then compared to the ground truth location of

Table 16. Average Error of point cloud reconstruction without homography.

Detonation	Triangulation (m)		Bundle Adj. (m)		N
	AVG	σ	AVG	σ	
Tesla	0.56	0.65	0.54	0.59	270
Turk	0.76	0.35	0.68	0.29	300
Met	1.62	0.93	0.98	0.59	120
Total	0.83	0.71	0.68	0.51	690

where the point should be. The error of each point is the Euclidean distance between the ground truth location of the points of the tower and their estimated position in the reconstruction. The error was then analyzed by detonation and isolating the x-, y-, and z-dimensions.

Table 16 shows the average error using triangulation and bundle adjustment without homography with N representing the number of points. The average error using triangulation was 0.83 meters and the average error using bundle adjustment was 0.68 meters. The expectation was that bundle adjustment would improve (decrease) the error of reconstruction and that was demonstrated in each case, but without statistical significance. A 95% confidence interval on triangulation has the true mean in the range of $(0 \ldots 2.25)$ meters. A 95% confidence interval on bundle adjustment has the true mean in the range of $(0 \ldots 1.7)$ meters.

Table 17 shows the average error using triangulation and bundle adjustment with homography. The average error using homography and triangulation was 0.76 meters and the average error using bundle adjustment and homography was 0.62 meters. A 95% confidence interval on triangulation and homography has the true mean in the range of $(0 \ldots 2.22)$ meters. A 95% confidence interval on bundle adjustment and homography has the true mean in the range of $(0 \ldots 1.66)$ meters.

Table 18 shows the error with regard to $x-$, $y-$, and $z-$dimension without homography while Table 19 shows the dimensional results with homography. The dimension-

Table 17. Average Error of point cloud reconstruction with homography.

Detonation	Triangulation (m)		Bundle Adj. (m)		N
	AVG	σ	AVG	σ	
Tesla	0.51	0.71	0.49	0.62	270
Turk	0.64	0.28	0.60	0.27	300
Met	1.61	0.93	0.96	0.60	120
Total	0.76	0.73	0.62	0.52	690

Table 18. Dimension of error of point cloud reconstruction without homography.

Dimension	Triangulation (m)		Bundle Adj. (m)	
	AVG	σ	AVG	σ
x	0.46	0.65	0.36	0.38
y	0.27	0.24	0.28	0.25
z	0.44	0.49	0.37	0.42
Total	0.83	0.71	0.68	0.51

ality of the error is evenly spread between dimensions. This is expected because the viewpoint angles of the detonations are close to 90° (Tesla 72°, Turk 63°, MET 68°). If the angles were smaller than 45°, the expectation would be that the $z-$dimension would dominate the error. On the bundle adjustment results without homography, a 95% confidence interval is $(0 \ldots 1.12)$ meters in the x-direction, $(0 \ldots 0.78)$ meters in the y-direction, and $(0 \ldots 1.21)$ in the z-direction. On the bundle adjustment results with homography, a 95% confidence interval is $(0 \ldots 1.11)$ meters in the x-direction, $(0 \ldots 0.66)$ meters in the y-direction, and $(0 \ldots 1.18)$ in the z-direction.

Table 19. Dimension of error of point cloud reconstruction with homography.

Dimension	Triangulation (m)		Bundle Adj. (m)	
	AVG	σ	AVG	σ
x	0.45	0.65	0.35	0.38
y	0.22	0.18	0.24	0.21
z	0.40	0.51	0.34	0.42
Total	0.76	0.73	0.62	0.52

Ground truth of the locations of points on the detonations are not known. To estimate the locations of points on detonations the techniques of triangulation and bundle adjustment were applied to points on a detonation and points on the detonation's tower where ground truth was known. Since the process of choosing points and the technique applied in reconstruction are consistent for the reconstruction, the error associated with the points with known ground truth can be inferred on the points where ground truth is not known. The locational error of the points of the tower then become the locational error of the points on the detonation.

6.4   Discussion

The results shown in Tables 18 and 19 provides the information necessary to estimate the spacial accuracy of points in an atmospheric nuclear detonation. With this new information, 3D point correspondences can be generated over a period or region of interest in a detonation enabling the study of regional areas of a detonation whose behavior is different than existing models. These point correspondences can be used to test the accuracy of other models by comparing the models to the point correspondence during that period in time.

One example of using this information for further research would be to track how points on the detonation change over time (Chapter VII).The change of location of the same points over time can be used to model how the detonation propagates in complex areas of the detonation, where the detonation interacts with objects or changes in atmospheric density. Using data assimilation [13] to fuse established mathematical models with the nuclear images and how they change over time would be a logical way to improve the accuracy of estimating the positional accuracy.

Another example would be to verify an estimate of volume generated from a single image. An assumption could be made that since the edges of a detonation

appear spherical, then the entire detonation is spherical. The results of a bundle adjusted reconstruction can generate points on the detonation recreating the depth component of the detonation at those points. The points can then be compared to a spherical rendering of the detonation to determine how accurate the spherical assumption is. If the edges of the sphere are within the error of reconstruction, the assumption would be confirmed as acceptable. Further assumptions could be made that the detonation is not spherical, but rather an ellipsoid with symmetric horizontal and depth components, but a differing vertical component. The differences between 3D point reconstructions and sphere could be compared to that of a 3D point reconstructions and an ellipsoid leading to conclusions that one model is more accurate than another. These comparisons are not possible without the understanding of the accuracy of the point correspondence grounded in truth locations that this process establishes.

6.5 Conclusions

This chapter presents a method to quantify the positional error of points in a 3D point cloud generated from triangulation and bundle adjusted reconstructions of nuclear material in a nuclear detonation. To quantify the positional error, 276 reconstructions were accomplished on 50% of applicable digitized detonations to estimate the positions of the support tower used in detonations. Ten points in each reconstruction were then compared to location information recorded at the time of detonation to estimate the positional error of a point. Reconstruction via triangulation was compared to reconstruction using bundle adjustment. Reconstructions using homography were compared to reconstructions not using homography. Using homography to register films from the same point of view and using bundle adjustment produces the best results. The error of a given point using homography and bundle adjustment can

be estimated with an average positional error of 0.62 meters with 0.35, 0.24, and 0.34 meters of uncertainty in x-, y-, and z-directions respectively. The three dimensional data sets created and the quantified error associated with 3D point reconstructions provides a method to verify volume-based models of nuclear detonations.

VII. Estimating Atmospheric Nuclear Detonation Volume

With the ability to determine 3D point clouds on the surface of the detonation, and the ability to detect subsphere features, the focus now turns to using that information to estimate volume of a detonation over time. Four detonations were analyzed with six volume generation methods: 1) sphere from 2D image, 2) ellipsoid from 2D image, 3) ellipsoid from 2D image augmented by subspheres, 4) sphere from 3D point cloud, 5) ellipsoid from 3D point cloud, and 6) space silhouette carving. Results show that 3D point cloud models are accurate in modeling detonation behavior in 3D space, but 2D models have the lowest variability when applied to estimate nuclear yields. Space carve models have low enough uncertainty to improve on radius-based models, but suffer from over estimation if there are not enough viewpoints.

The remainder of this chapter is organized as follows. Sec. 7.1 discusses the processes that were used to generate volume from the images and Sec. 7.2 discusses the detonations that were analyzed. Sec. 7.3 presents the results and Sec. 7.4 concludes the chapter.

7.1 Volume Estimation Processes

Six processes were used in estimating the volume of an explosion and the results were compared. The first assumes that the explosion is spherical and the estimates for the radius of the sphere are determined by a 2D image. The second assumes that the explosion is a 3D ellipsoid. The third assumes that the big explosion is a 3D ellipsoid with spherical subspheres protruding from it. The fourth volume estimation process generates a sphere from a 3D point cloud of points on the surface of the detonation. The fifth process generates an ellipsoid that is symmetric about the depth and horizontal axis from the same 3D point cloud. The sixth and final process
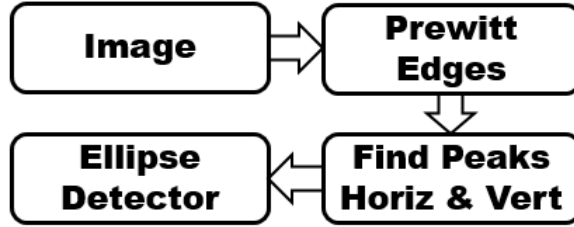
Figure 44. Flow diagram of estimating the radius of an explosion.

carves the volume using the projection matrices and the silhouettes of the detonations. For comparison purposes, a volume is also derived from documented yields for the detonations.

Sphere estimation from 2D image.

The first volume estimation is based on the volume equation of a sphere (Eq. 24). To determine the volume based on the spherical assumption, the only parameter that needs to be estimated is the radius (r). Fig. 44 shows a flow diagram to estimate the radius of the larger explosion. Referring to Fig. 44, the image is processed with Prewitt edge detection [21], and the first and last edges vertically and horizontally are used to estimate the boundary of the explosion. The ellipse detector then fits an ellipse to the boundary of the explosion. The major axis and minor axis are then averaged to find the radius.

$$V = \frac{4\pi}{3}r^3 \qquad (24)$$

This estimation of volume is analogous to one that would be used in a yield equation based solely on radius (Eq. 1).

Ellipsoid estimation from 2D image.

The volume of an ellipsoid that is symmetric about the x- and z-axis is shown in Eq. 25. Estimating the volume from an ellipsoid is similar to that of the process described for the sphere estimation. Instead of averaging the major axis (a) and minor axis (b), the values will be used directly in Eq. 25.

$$V = \frac{4\pi}{3} a^2 b \tag{25}$$

Subsphere Volume estimation from 2D images.

The third estimation of volume that was tested is based on the detection of subspheres that was discussed in Chapter III. The concept is to detect the subspheres, estimate their center and radius and add the additional volume to that of the main explosion to improve the overall estimate of volume.

As discussed in Chapter III, to detect the subspheres, images were processed with histogram equalization and features were defined and extracted on pixels in the image. These features were reduced with PCA, fit with ellipse detection, and projected on to a 3D space based on the interaction between the subsphere and the larger detonation.

Deriving the volume of a ellipsoid intersecting a sphere begins with the equation for the intersection of two spheres. Eq. 26 is the equation for the volume of two intersecting spheres where d is the distance between the two centers, r_1 is the radius of the first circle, and r_2 is the radius of the second circle [38]. Applying this to the current problem of intersecting a ellipsoid and a sphere, one of the radii must be stated in terms of an ellipsoid.

$$V = \frac{\pi}{12d}(r_1 + r_2 - d)^2(d^2 + 2d(r_1 + r_2) - 3(r_1 - r_2)^2) \tag{26}$$

Beginning with the equation of an ellipsoid (Eq. 27), and with the assumption

that the ellipsoid is symmetric about the x- and z-axis (i.e. $a = c$), the equation is solved for r (Eq. 28). Also, since the values of θ and ϕ depend on the direction in which the sphere intersects the ellipsoid they are dependent also on parameters of the intersecting subsphere. These are shown in Eq. 29 and Eq. 30 where (x_1, y_1, z_1) is the center of the ellipsoid and (x_2, y_2, z_2) is the center of the subsphere.

$$\frac{r^2 \cos^2 \theta \sin^2 \phi}{a^2} + \frac{r^2 \sin^2 \theta \sin^2 \phi}{b^2} + \frac{r^2 \cos^2 \phi}{c^2} = 1 \tag{27}$$

$$r = \frac{a^2 b}{\sqrt{a^2 b^2 \cos^2 \theta \sin^2 \phi + a^4 \sin^2 \theta \sin^2 \phi + a^2 b^2 \cos^2 \phi}} \tag{28}$$

$$\theta = \tan^{-1}\left(\frac{y_1 - y_2}{x_1 - x_2}\right) \tag{29}$$

$$\phi = \tan^{-1}\left(\frac{\sqrt{(y_1 - y_2)^2 + (x_1 - x_2)^2}}{z_1 - z_2}\right) \tag{30}$$

Now that the equations are available to determine the volume of a sphere intersecting with an ellipsoid, the focus shifts to estimating the location of the sphere relative to the ellipsoid. Fig. 45 shows a flow diagram to determine the location of subspheres.

Referring to Fig. 45, the process begins in step 1 by performing a histogram equalization on the image. Then, principal components analysis is used to classify pixels as subsphere or not. In step 3, the PCA raw results are simplified to the horizontal and vertical centerlines of the subsphere pixel detections. In step 4, the PCA subsphere edges are input into an ellipse detector. In Step 5, the intersection of the subsphere edges and the 10-pixel neighborhood of the ellipse create an output that represents the ellipse edges. In step 6, each of these ellipse edge pixels is given a z-coordinated based on its x and y location within the larger ellipsoid. Step 7 fits a minimum mean squared error sphere to these ellipse edge points. The result is the required center and radius of the subsphere. The location of the sphere interacting with the ellipsoid then determines the volume of the ellipse augmented with the
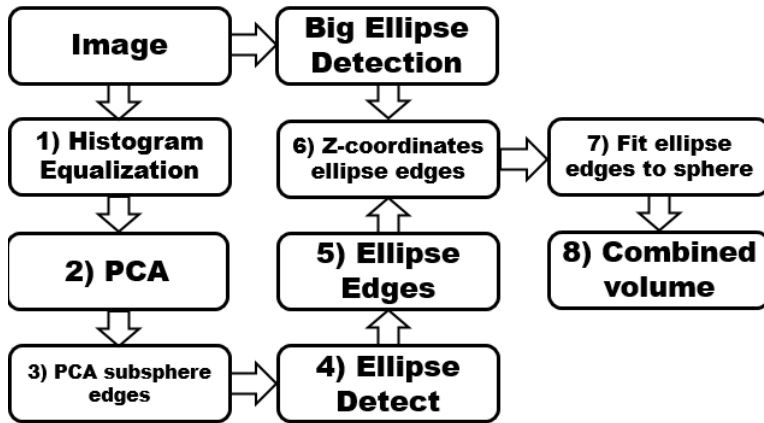
Figure 45. Flow diagram of estimating the subsphere location.

subspheres.

Sphere from 3D point cloud.

The next volume estimate was based on a least squares fit of a sphere [11] to a 3D point cloud of points on the surface of a detonation. Point clouds were generated using triangulation that were improved with bundle adjustment using point correspondences from an automated hotspot detection process (Fig. 46) [25]. The result is a 3D point cloud based on hotspots on the surface of the detonation. A least squares sphere is then fit to the point cloud (Fig. 47).

Ellipsoid from 3D point cloud.

The next volume estimate was based on a least squares fit of an ellipsoid [10] symmetric about the depth and horizontal axis to a 3D point cloud of surface points of a detonation. This volume estimate uses the same 3D point cloud generated as the least squares sphere fit.

89
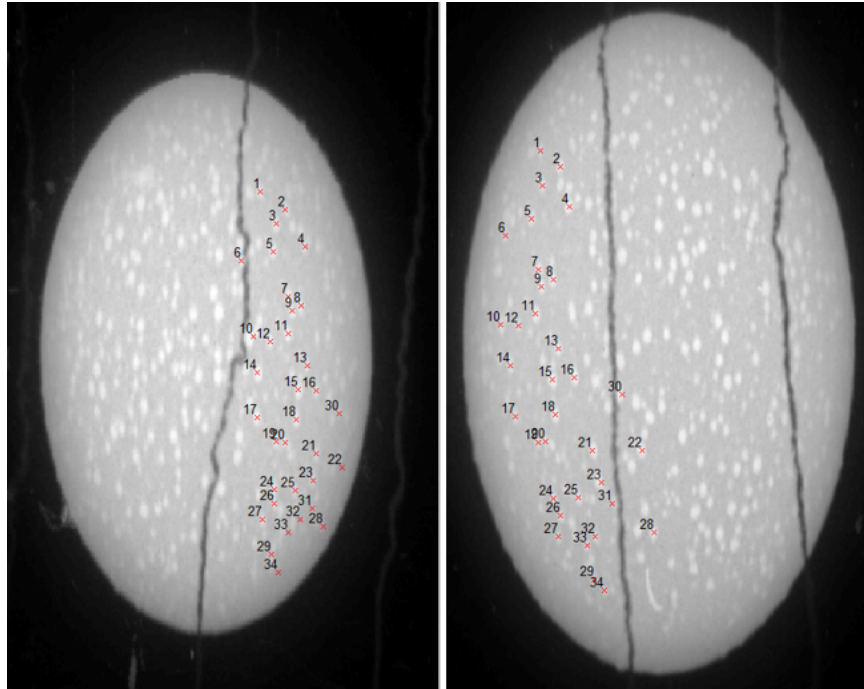
Figure 46. Hotspot detection and matching [25] results on Climax detonation.
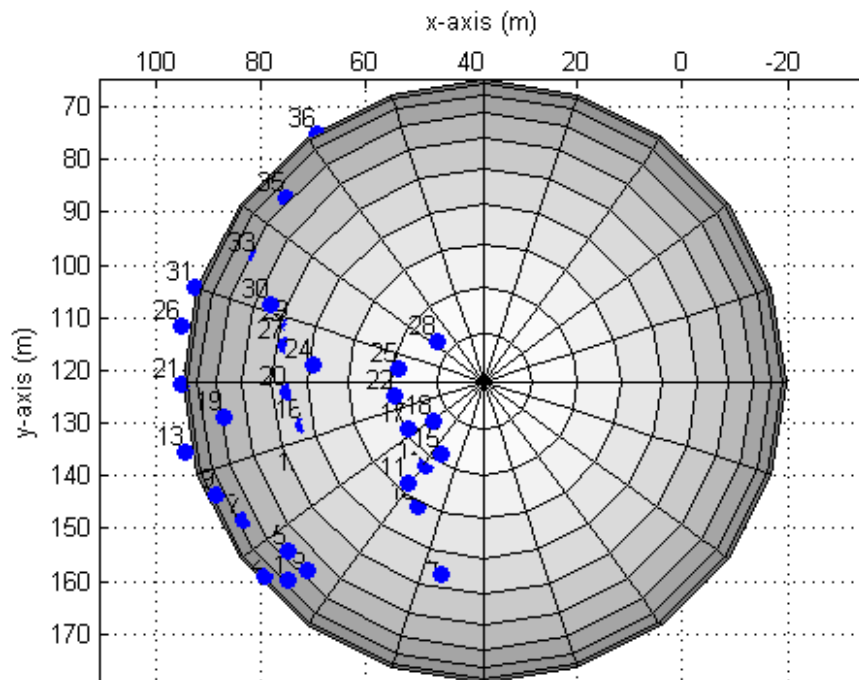
Figure 47. 3D point cloud and least squares sphere fit to Tesla detonation hotspots.

Space Carving Volume.

The final volume estimate was based on space carving theory [12]. Images are converted to silhouettes by detecting the edges of the detonation. Then, using the refined projection matrices from bundle adjustment, the silhouettes are used to carve out the volume of the detonation (Fig. 48).

Volume models using Homography.

Two additional volumes were generated using Homography (see Sec. 6.1) versions of the 3D point clouds. The processes that were used in earlier testing (Sec. 6.2) that saw reduction in errors and uncertainty were also used in volume estimation. This results in models Sphere3D, and Ellipse3D with Homography.

Volume based on documented yields.

For comparison purposes, a volume was generated from the documented yields [6]. The equation used for this was the same as Taylor's equation [36] in Eq. 2, just solved for V resulting in

$$V = [\frac{Yield \times t^2}{p_o}]^{\frac{3}{5}}.$$

The documented estimate of volumes are not ground truth, but are derived from documented yields. For example, the documented yield [6] of Climax is 61 kT, but recent research [30] has more accurately estimated it at 58.74 ± 0.19 kT. Even if the documented values are not without error, they do provide a baseline for comparison.
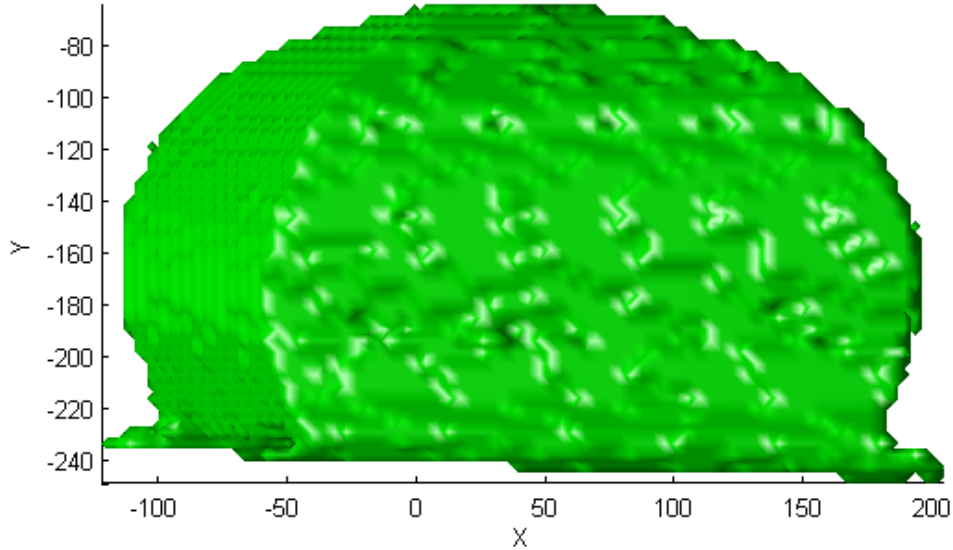
Figure 48. Rendering of space carving results from two cameras of the MET detonation.

Table 20. Detonations tested.

Detonation	Test Series	Type	Yield (kT)
Climax [6]	Upshot-Knothole	Airdrop	58.74 [30]
Grable [6]	Upshot-Knothole	Airdrop	15 [6]
MET [6]	Teapot	Tower	22 [6]
Tesla [6]	Teapot	Tower	7 [6]

7.2 Workload

Table 20 shows the detonations that were used for volume estimation. Two detonations (Climax and Grable) were chosen that were airdrops because they tend to be more uniform in shape as a result of not having any obstructions to interfere with the nuclear shock wave. An additional two detonations (MET and Tesla) were chosen because they were tower detonations that demonstrated the subsphere features. The ellipse plus subsphere approach was not attempted on the airdrop detonations because of the lack of subspheres.

7.3 Results

The results of volume estimations for Climax, Grable, Tesla, and MET are shown in Figs. 49, 50, 51, and 52 respectively. Table 21 shows the average residuals as compared to the documented estimate of volume normalized using the average volume. Table 22 shows the standard deviation of the models resulting from a bisquare weighted regression [3]. In all figures, it is apparent that the ellipsoid fit to a 3D point cloud is the most unstable estimate as there are cases that are both significantly over and under the documented estimate. Ellipsoid 3D volume instability is also evident in Table 22 as the Ellipsoid 3D volume has the highest standard deviation (SD) of all the volume estimates for every detonation. It is also clear that despite wide ranging assumptions in the different volume methodologies, the estimates are all generally consistent with each other and follow the same trend as the documented estimate.

The analysis here will focus on the SD of the results. The average difference between the documented estimate is less important because it is based on a documented yield that may be incorrect. Overall, the 2D estimates have the least amount of variability. The volumes consistently climb as time increases, with the exception of small drops caused by incorrect ellipse detections. The variance decreases slightly as the method changes from 2D sphere to 2D ellipsoid to 2D ellipsoid + subsphere.

Considering the 3D volume estimates, the variance is higher than the 2D estimates. For yield models to be improved by a volume-based model, the SD of the volume models must be no more than three times the SD of the radius models. This can be analyzed by comparing the 2D SDs to the 3D SDs. Considering the Grable estimate with Sphere 2D volume SD of $20,928m^3 \times 3 = 62,784m^3$ this is still smaller than the Sphere 3D and Ellipse 3D with Homography with SD of 158,320 and 214,140 m^3 respectively. This means that the Sphere 3D and Ellipse 3D models have too large an uncertainty to improve over 2D models for the purpose of yield estimation. The

space carve model, however has SD of 44,917 m^3 which is less than three times the SD of radius models. The space carve model SD also has less uncertainty than three times the Sphere 2D models in the Climax and Tesla detonations, but not the MET detonation.

It is also notable that the volume estimates from space carving tended to run consistently high. The reason for this is because of the lack of viewpoints applied to the space carving model. The space carve model is designed for objects that are photographed on a turntable with about 24 viewpoints evenly spread out every 15°. The object is then carved from a cube depending on the viewpoints. In the estimates for detonation volume, viewpoints were limited and only two viewpoints were used leaving a considerable volume uncarved from the original cube. While the estimates run consistently high, it is, however, within expectations as estimates are no more than twice the expected volume. This expectation is established by comparing the volume of a sphere inscribed inside a cube. A sphere with radius r has volume $\frac{4}{3}\pi r^3 \cong 4r^3$ while a cube has volume $(2r)^3 = 8r^3$. The statistics in Table 21 show this over estimation between 13.96% and 51.47% for the detonations analyzed. Applying more viewpoints would further reduce this over estimation of volume.

The assertion that adding additional viewpoints would reduce the over-estimation problem was tested with an available third point of view for the Grable detonation. Adding a third point of view has challenges in aligning three films with frames that have similar time stamps. The result is a reduction in the number of available data points that meet the time match criteria. Fig. 50 shows the results of a space carve with three points of view. Table 23 compares the results of two points of view and three points of view for space carving and Sphere 2D volume models. Referring to Table 23, the over-estimation of volume using space carving is reduced from over-estimating by 32.45% to under-estimating by 1.7 % as compared to the documented

94

Table 21. Average Volume Bias, Normalized as percentage.

Vol. Method	Climax	Grable	MET	Tesla
Sphere 3D	-5.65	-11.56	10.25	-17.47
Sphere 3D w/ H	-5.95	-12.3	8.28	-17.47
Ellipsoid 3D	-3.49	-6.57	7.23	1.09
Ellipsoid 3D w/ H	-3.26	-8.15	5.63	1.09
Space Carve	39.7	32.45	51.47	13.97
Sphere 2D	-1.41	-5.19	3.04	12.07
Ellipsoid 2D	-1.08	-4.8	3.53	12.86
Subsphere 2D	N/A	N/A	3.69	12.92

Table 22. Standard deviations of Volume estimates in cubic meters.

Vol. Method	Climax	Grable	MET	Tesla
Sphere 3D	3,190,400	160,110	901,340	71,473
Sphere 3D w/ H	1,222,700	158,320	804,000	71,473
Ellipsoid 3D	3,579,900	211,520	1,024,300	95,061
Ellipsoid 3D w/ H	2,673,800	214,140	1,012,300	95,061
Space Carve	556,260	44,917	406,820	5,001
Sphere 2D	196,840	20,928	46,810	5,172
Ellipsoid 2D	190,140	20,095	47,547	8,186
Subsphere 2D	N/A	N/A	46,542	7,982

estimate of yield. The SD on the three points of view of the space carve is greater than three times the Sphere 2D model which is a result of the fewer points caused by timing restrictions on aligning three films together. This would be expected to fall back in line with more data tested as was the case with the two points of view.

In summarizing the results, the volume estimates are consistent with each other. This consistency validates the 3D point clouds that were used to generate the 3D volume estimates. The 2D models are still the most reliable for predicting yield. For the 3D Sphere and 3D Ellipse models to improve upon the 2D models for yield estimation, the SD in estimates must be reduced. The space carving model has a small enough SD to improve over 2D models, and its over estimation could be improved with more viewpoints if sufficient time aligned frames exist.

Table 23. Statistics comparing two points of view with three points of view for space carve and Sphere 2D for Grable.

	2 POV		3 POV	
Vol. Method	SD (m^3)	AVG % error	SD (m^3)	AVG % error
Space Carve	44,917	32.45 %	65,768	-1.7 %
Sphere 2D	20,928	-5.19 %	14,162	-5.45 %
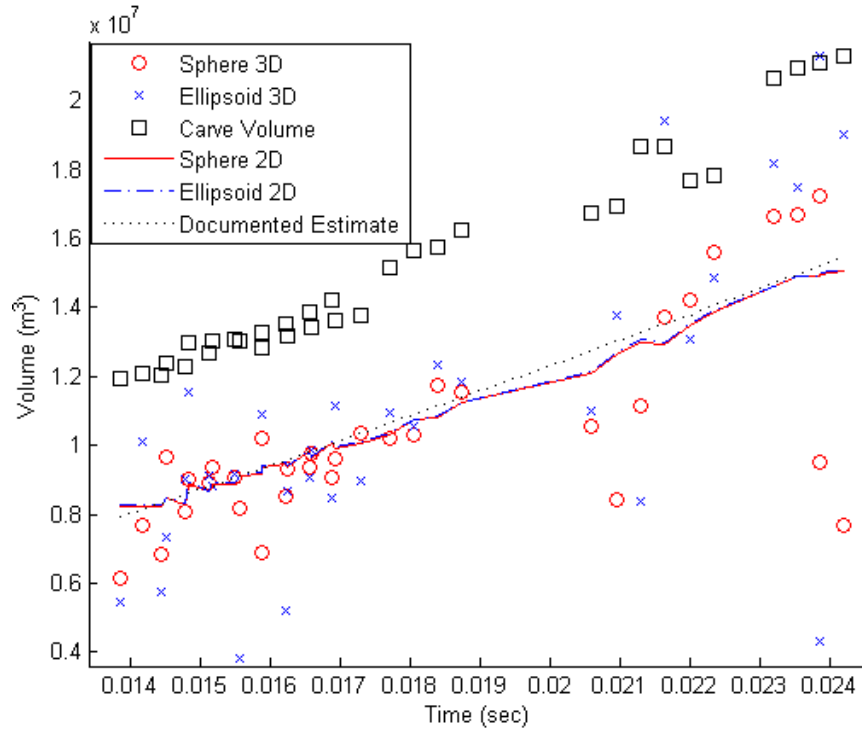
Figure 49.   Volume estimates of Climax.

7.4   Conclusions

The estimates of volumes generated for the four detonations are all consistent with each other and the documented estimates of volume adding credibility to the models that were used to generate them. The 3D volume estimates also validate the position locations of the 3D point clouds that are used to generate them, although their variability needs to improve for them to have higher reliability in estimating yields than radius-based methods. The space carve model has low enough SD to
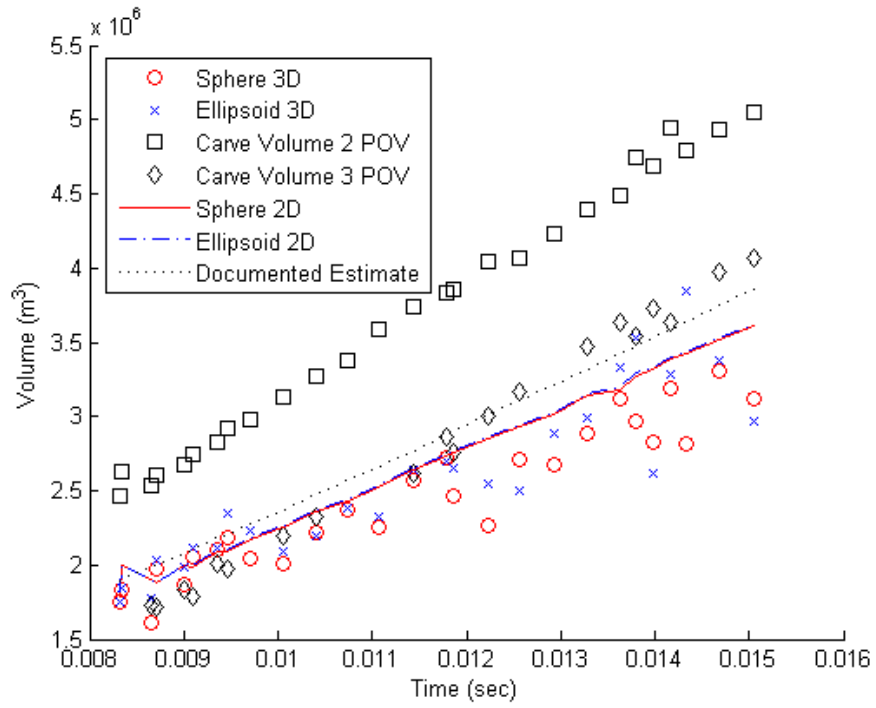
Figure 50.   Volume estimates of Grable.

improve on radius models, and its over-estimates in volume can be reduced by using
at least three points of view.

97
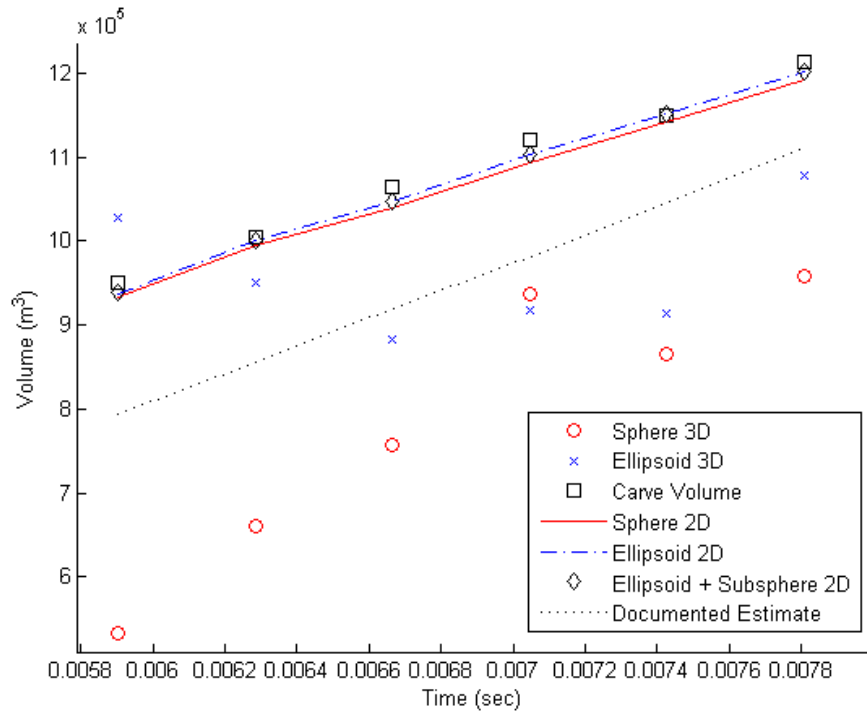
Figure 51. Volume estimates of Tesla.
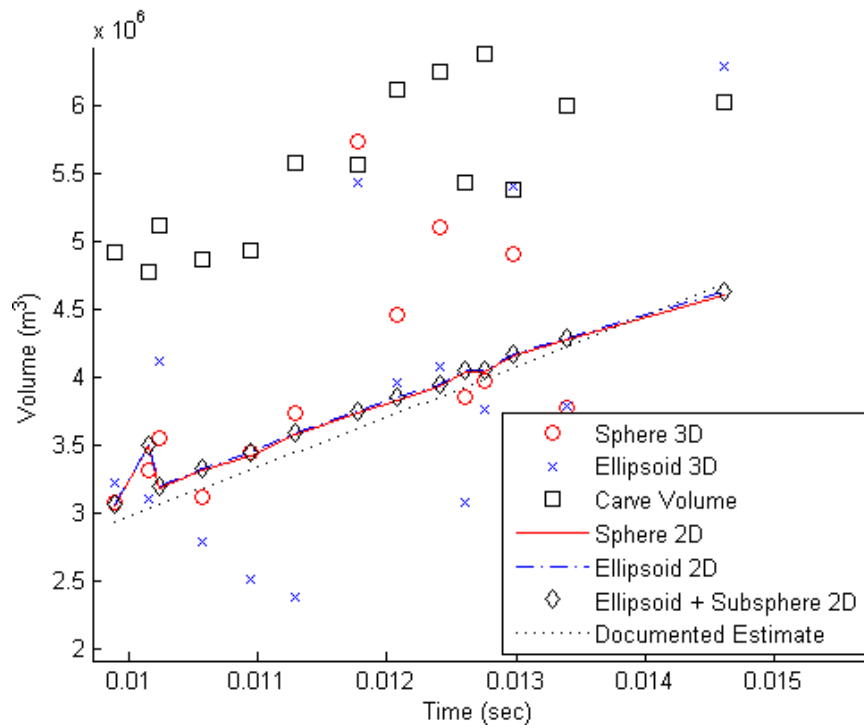
Figure 52. Volume estimates of MET.

98

VIII. Conclusion and Future Work

The primary goal of this research was to provide an automated means to perform three-dimensional analysis for atmospheric nuclear detonation films. It was hypothesized that this could be accomplished by applying multi-view geometry and computer vision techniques to the films in order to determine 3D positional information and volume estimation over time. To accomplish this required alignment of the films in time, detection of features in the images, matching of features, and multi-view reconstruction. Sub-explosion features were detected with 67% hit rate and 22% false alarm rate. Hotspot features were detected with 71.95% hit rate, 86.03% precision and a 0.015% false positive rate. Detected hotspots were matched across 57-109° viewpoints with 76.63% average correct matching by defining their location relative to the center of the explosion, rotating them to the alternative viewpoint, and matching them collectively. When 3D reconstruction was applied to the hotspot matching it completed an automated process that was used to create 168 3D point clouds with 31.6 points per reconstruction with each point having an accuracy of 0.62 meters with 0.35, 0.24, and 0.34 meters of accuracy in the x-, y- and z-direction respectively. As a demonstration of using the point clouds for analysis, volumes were estimated and shown to be consistent with radius-based models and in some cases improve on the level of uncertainty in the yield calculation.

8.1 Contributions

This document proposes the following contributions to the scientific community.

- The production of 3D sparse point clouds to track and study features of detonations over time.

- An automated process to detect and match of hotspot features across wide viewpoints.

In Chapter IV and V an automated hotspot feature detector and matching algorithm was tested that matches hotspots across wide viewpoints using a spherical-based object model. Hotspots can be detected with a 71.95% hit rate and 86.03% precision. Hotspots are matched to films from wide viewpoints with 76.6% correctness and a σ of 16.4% where the state-of-the-art matching techniques of SIFT and SURF fail. Viewpoints were tested up to 109.5° significantly extending the viewpoint matching capability. The addition of an automated techniques generated 168 3D reconstructions across four detonations where manual reconstructions only were able to generate nine 3D reconstructions during the same period of time. Within the NUDET domain, the new automated technique provides the ability to study the NUDET in three-dimensions. Outside the NUDET film domain, this demonstrates that a sphere and polar coordinates can effectively be used to extend viewpoint matching when objects in the image are spherical.

With regard to 3D positional estimation, the results of Chapter VI show that using Homography and bundle adjustment that manually chosen points can be reconstructed in three-dimensions with an average positional error of 0.62 meters with 0.35, 0.24, and 0.34 meters of uncertainty in x-, y-, and z-directions respectively. This establishes a baseline of ground truth using the triangulation and bundle adjustment techniques for the NUDET 3D point clouds. This improves the historical record of the films by providing reliable, three-dimensional positional estimates of features within a NUDET.

Lastly, volume estimations were derived from the films using six different volume models. Yields estimated from these volumes were found to be consistent with radius-based models. The space carve model did show low enough uncertainty to replace

radius-based models, but it needs at least three viewpoints to counteract the over-estimation of volume.

8.2   Future Work

One item of future work would be to apply the automated hotspot matching technique to more detonations. Other types of detonations like balloon suspended detonations, surface detonations, and water surface detonations could be studied in three-dimensions with greater accuracy and speed using the automated model. An individual with expertise in physics could take the 3D point cloud results and interpret them to see if it models can be defined that account for the changes in detonation type from airdrop, balloon, tower and surface.

Another item of future work is to improve the techniques applied for volume estimation to reduce the STD of volume estimations.

Another item that could be studied is another NUDET feature. This dissertation showed that hotspots could be detected as well as subspheres, but cone features or other features could be detected and fed into the automated viewpoint matching model to match just like hotspots were. The hotspot feature detector could be replaced with a more generic detector that doesn't only consider hotspots, but all features whether their light or dark contrasting with areas around it. This would likely merge some capabilities of SIFT and SURF with the sphere-based wide-viewpoint model making it more accessible outside the NUDET domain.

Another item that could be used to improve on the models presented would be to correlate more than two views at a time. This dissertation focused on two points of view because it was the most common case with availabe data that was of similar distances which helped detection and matching of hotspots. But it is possible that other data sets exist that either have a third site that is of similar distance to two

other sites, or could be correlated using features that are visible at varying distances. With each additional viewpoints needing to be correlated in time with the others, this is likely more difficult to find time aligned frames, but is quite possible.

Other future work could look into current day applications to build a system using multiple cameras with atomic timing that could record non-nuclear detonations and estimate their volumes using space carving. If such a system could accurately estimate the volume of non-nuclear detonations, then it could provide the baseline for a camera-only system for determining the yield of rogue devices.

Other work could test the feature detector and descriptor on other spherical based objects to see how well it applies in the current day image domain of spherical objects needing wide viewpoint matching capabilities.

Lastly, a study could characterize how accurate the current time models are by using the 3D time sequenced hotspots with the inverse of the nuclear growth model to determine time and compare it to the time estimated using the timing marks. There are areas of certain films where the speed of the camera changes abruptly between timing marks and this analysis would likely determine within a frame or two where the anomaly occurs, instead of the current method that can only tell when the next timing mark occurs (approx. 10-15 frames).

Appendix A. Camera Calibration

This section discusses how the finite projective camera model is applied to the NUDET data set.

1.1   Estimating Camera Intrinsics (K)

To calculate the camera intrinsic values ($\mathbf{K}$) for the NUDET data, each of the parameters of K must be determined. The definition of $\mathbf{K}$ from the finite projective camera model is

$$\mathbf{K} = \begin{bmatrix} \alpha_x & s & x_0 \\ & \alpha_y & y_0 \\ & & 1 \end{bmatrix}$$

and that $\alpha_x = fm_x$, $\alpha_y = fm_y$, $x_0 = m_x p_x$, and $y_0 = m_y p_y$ where f is the focal length, m_x and m_y are the pixels per unit distance in image coordinates in the x- and y-directions, and p_x and p_y are the coordinates of the principal point, and s is the skew.

For now, the assumption will be made that the skew is zero ($s = 0$). The focal length is also recorded in the original documentation [30]. This leaves four parameters that need to be determined (m_x, m_y, x_0, and y_0).

Estimating m_x and m_y.

To estimate m_x and m_y, it must be determined how many pixels/mm exist in the image in the x- and y-directions. This must be done relating the pixel dimensions of the scanned film to the original 16mm film. The type of film used most commonly was Microfile (MF) [30]. MF was developed by Kodak for the nuclear testing program and was used because of its ability to retain its chemical properties in high radiation environments and because of its high resolution. In addition, the majority

103

of recordings were acrylate or polyethylene based black and white films which have an expected lifespan of 100-500 years according to ANSI Standard IT9.11-1992. Fig. 53 shows the dimensions of the film that was used in filming [30]. All of the images used were perforated two edges with Eastman Kodak long perforation (2R-3000). The dimensions between perforations width-wise (distance F in Fig. 53) determines the x dimensions. The dimensions between each perforation vertically (distance B in Fig. 53) determines the y dimensions. Samples of each video were taken, and the distance measured in the images in pixel length and related to the pixel lengths in the x- and y-direction (10.49 mm and 7.62 mm respectively). As a result, an equation is set for m_x and m_y.

$$m_x = \frac{horizontal\ pixel\ length\ between\ perforations}{10.49mm}$$

$$m_y = \frac{vertical\ pixel\ length\ between\ perforations}{7.62mm}$$

Measurements of at least 4 images were taken in the x- and y-direction and the pixel difference was averaged for each film. To determine the vertical distance, subsequent frames were stacked vertically to recreate the continuous feel of the original film. When this was accomplished it was determined that there was some overlap between subsequent images of 10 pixels which could be visually determined by repetition in the pixel pattern. After this 10 pixel overlap was removed from the y-distance the results were accurately computed and are shown in Table 24.

Referring to Table 24, it is apparent that there was very little variation in the measurement of x-distance. The maximum error was calculated based on the worse case scenario that both the measurement error (σ) and the tolerance of the perforation of the film were additive when in fact the error is likely that it is the larger of these two errors. With this in consideration, all the variance in measurement is within

Perforated one edge

Perforated two edges
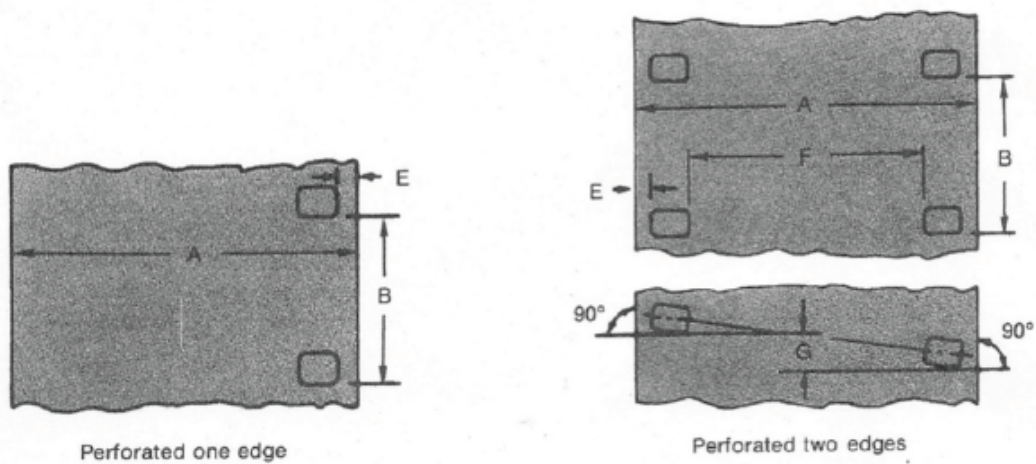
Perforation Type and ANSI Number										
Dimension	1R-2994 (PH22.109)		1R-3000 (PH22.12)		2R-2994 (PH22.110)		2R-3000 (PH22.5)		Tolerances ±	
	Inches	mm	Inches	mm	Inches	mm	Inches	mm	Inches	mm
A*	0.628	15.95	0.628	15.95	0.628	15.95	0.628	15.95	0.001	0.03
B	0.2994	7.605	0.3000	7.620	0.2994	7.605	0.3000	7.620	0.0005	0.013
E	0.0355	0.902	0.0355	0.902	0.0355	0.902	0.0355	0.902	0.0020	0.051
F					0.413	10.49	0.413	10.49	0.001	0.03
G (max)					0.001	0.03	0.001	0.03	—	—
L†	29.94	760.5	30.00	762.0	29.94	760.5	30.00	762.0	0.03	0.8

*This dimension also represents the unperforated width.
†This dimension represents the length of any 100 consecutive perforation intervals.

Figure 53. Dimensions of the 16mm film[30].

Table 24.   Results of estimating m_x and m_y.

Film	m_x $(\frac{pixels}{mm})$				m_y $(\frac{pixels}{mm})$			
	$\bar{m}_x$	2σ	Tolerance	Max Err.	$\bar{m}_y$	2σ	Tolerance	Max Err.
02	114.585	0	0.328	0.328	114.436	0.131	0.195	0.326
03	114.681	0	0.328	0.328	113.71	0.151	0.194	0.345
04	114.49	0	0.327	0.327	113.65	0	0.194	0.194
06	114.49	0	0.327	0.327	113.58	0.151	0.194	0.345
07	114.68	0	0.328	0.328	113.58	0.151	0.194	0.345
08	114.49	0	0.327	0.327	114.04	0	0.194	0.194
09	114.49	0	0.327	0.327	113.583	0.151	0.194	0.345
10	114.49	0	0.327	0.327	114.04	0	0.194	0.194
11	114.49	0	0.327	0.327	114.04	0	0.194	0.194
12	114.49	0	0.327	0.327	113.61	0.151	0.194	0.345
16	114.49	0	0.327	0.327	114.04	0	0.194	0.194
17	114.49	0	0.327	0.327	113.583	0.151	0.194	0.345
18	114.82	0.14	0.327	0.462	113.58	0	0.194	0.194

tolerance of the production of the film perforations.

On the other hand, there appears to be evidence of skew. The 95% confidence interval of m_x is (144.347, 114.772) while the 95% confidence interval of m_y is (113.238, 114.337). The fact that these two intervals don't overlap on a value that should be equal likely means that something in the digitization process of these image is shortening them vertically, or lengthening them horizontally. Regardless, values for m_x and m_y are now known.

Estimating x_0 and y_0.

Estimating x_0 and y_0 is preferable above estimating p_x and p_y because x_0 and y_0 units are in terms of pixels and can be determined from the scanned image, while p_x and p_y units are in terms of mm, and would require analyzing the films exactly, or first estimating x_0 and y_0 and extracting p_x and p_y from their m_x and m_y relationships.

Estimating x_0 and y_0 can be accomplished in one of several methods. The parameters x_0 and y_0 are intended to represent the center of the image plane. The

question then is, what is the image plane in this case? Three possible image planes are considered with different definitions of the image plane. Also, Fig. 54 shows the description of these different centers pictorially. Each of these are considered in turn.

1. Center of the resolution of the image

2. Center of the viewable portion of the image

3. Center of the emulsion layer of the image

Center of image. The center of the image is the most straight forward. It takes the resolution of the image, and divides by 2 to get the center of the image. The drawback is that some of the films are misaligned from left to right when they were scanned.

Center of viewable area. The center of the viewable area on the image is also straight forward. The film has borders on the left and right for the perforation of the film. By removing the perforated areas, the actual area that contains images can be isolated. This can remove any error that would result in misalignment of the film when they were scanned.

Center of emulsion layer of film. Within the film itself there is a layer that is intended to be exposed and collect the light particles. This layer is not always centered with the film itself. It is ultimately the collector of photons. An argument could be made that the emulsion layer represents the portion that was actually exposed to light, and as a result the center of the of that area is truly the center of the image.

Prior to determining a center, a standard image crop was determined that removed the left and right side perforated edges. To accomplish this, all the pixel values of all the images of Tesla were summed column-wise. Then the local minimums on either side of the plot was used as the cropping in the x-direction. This plot is shown in Fig. 55. The end result is that cropping the image at 352, 1490 would be the best

107
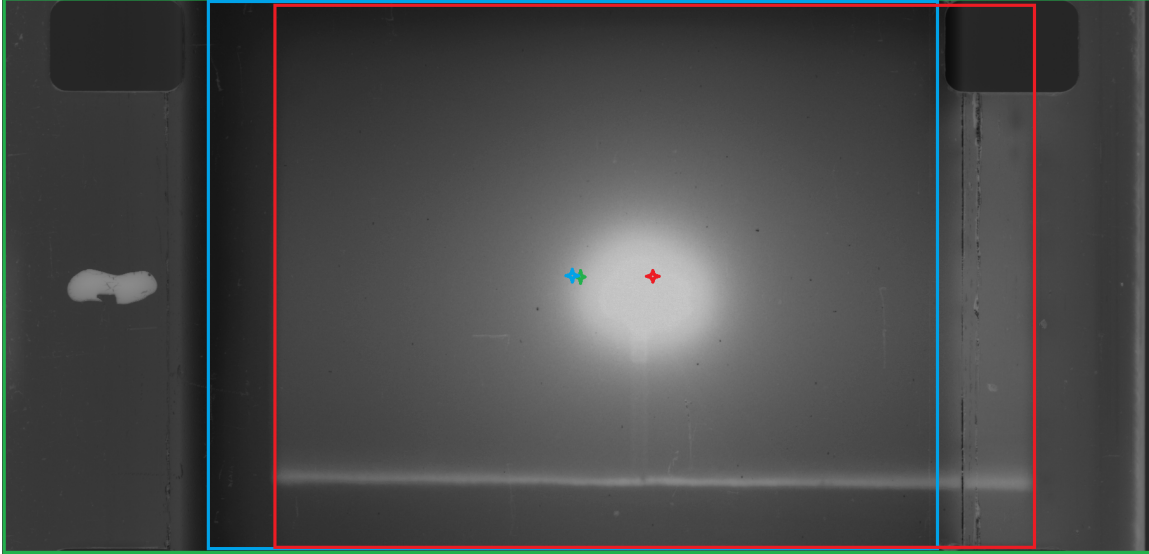
Figure 54. A pictorial example of different principal points. The boundaries of different methods are outlined with their center principal point. Green is based on the overall image, Blue is based on the viewable area, Red is based on the emulsion layer reacting with the light.

standard cropping dimensions for Tesla.

Table 25 shows what these measurements are for the Tesla [30] fireball films.

Estimating (K).

All the parameters are in place to estimate $\mathbf{K}$, the camera intrinsic matrix. The unit values of $\mathbf{K}$ are in terms of pixels. Referring to Table 24 and Table 25, and the focal lengths in the load sheets [30], $\mathbf{K}$ can now be estimated. Eq. 31 shows $\mathbf{K}$ for
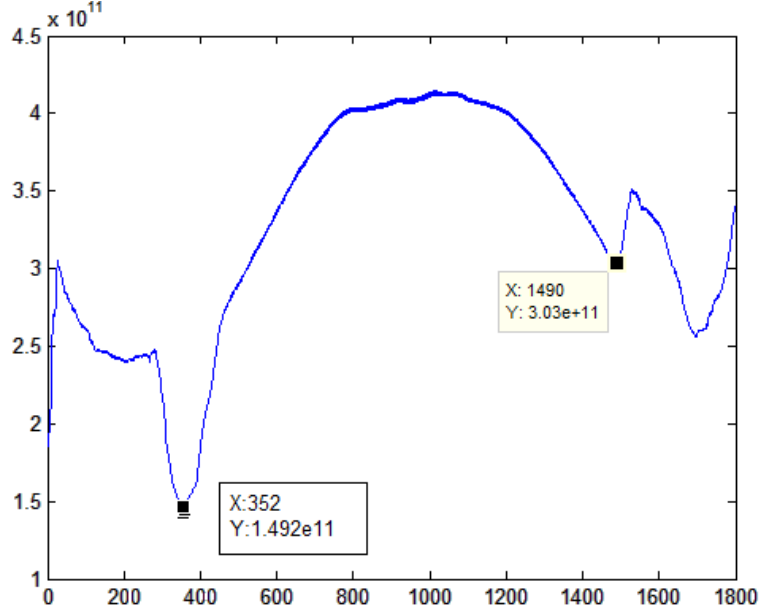
Figure 55. A summary of pixel intensities by column. The low points on either side represent where the best area to crop the images would be.

Tesla camera 2 [30] using the center of the viewable area as the principal point.

$$
\mathbf{K} = \begin{bmatrix} \alpha_x & s & x_0 \\ & \alpha_y & y_0 \\ & & 1 \end{bmatrix} = \begin{bmatrix} f*m_x & s & x_0 \\ & f*m_y & y_0 \\ & & 1 \end{bmatrix}
$$

$$
= \begin{bmatrix} 102.1*114.585 & 0 & 561 \\ & 102.1*114.436 & 441.5 \\ & & 1 \end{bmatrix} = \begin{bmatrix} 11699 & 0 & 561 \\ & 11683 & 441.5 \\ & & 1 \end{bmatrix} \tag{31}
$$

1.2 Estimating P

With $\mathbf{K}$ estimated, $\mathbf{P}$ can be estimated. Recalling that $\mathbf{P} = \mathbf{KR}[\mathbf{I}|\tilde{\mathbf{C}}]$, $\mathbf{K}$ is known, $\mathbf{I}$ is identity, only $\mathbf{R}$ and $\tilde{\mathbf{C}}$ need to be identified. $\mathbf{R}$ is the rotation of the camera that can be defined from the bearing (azimuth) from the ground zero location and the camera locations. $\tilde{\mathbf{C}}$ can be determined from the camera locations relative to ground

109

Table 25. Principal point by camera and method.

Camera No.	Center image x_0	y_0	Center viewable x_0	y_0	Center Emulsion x_0	y_0
02	564	441.5	561	441.5	675.5	441.5
03	558	438.5	546.5	438.5	648.5	438.5
04	558	438.5	559	438.5	689.5	438.5
05	558	438.5	567.5	438.5	678.5	438.5
06	558	438.5	539.5	438.5	648.5	438.5
07	561	440	584.5	440	690	440
09	558	438.5	545	438.5	655	438.5
10	561	440	572.5	440	708	440
11	561	440	579.5	440	706.5	440
12	558	438.5	567.5	438.5	665.5	438.5
16	558	438.5	560.5	438.5	706.5	438.5
17	558	438.5	561	438.5	681	438.5
18	558	438.5	549	438.5	675	438.5

zero in world coordinate space.

Both $\mathbf{R}$ and $\tilde{\mathbf{C}}$ and can come from data recorded at the time that the NUDET tests were accomplished. Fig. 56 shows an example of some of the survey data that was recorded at the time of the NUDET test. Since cameras 2, 3,4, and 6 were located on truck 2-355, the relative coordinates $(\Delta N, \Delta E, \Delta Z)$ from ground zero (in this case site T-9B) can be used for $\tilde{\mathbf{C}}$. $\mathbf{R}$ can be determined by using the angles (bearing and tilt). With θ representing bearing, ϕ representing tilt, and $\psi = 0$ the rotation matrix can be represented using a directional cosine matrix as show in Eq. 32.

$$
\mathbf{R} \;=\; \begin{bmatrix} \cos\theta\cos\psi & \cos\phi\sin\psi + \sin\phi\sin\theta\cos\psi & \sin\phi\sin\psi - \cos\phi\sin\theta\cos\psi \\ -\cos\theta\sin\psi & \cos\phi\cos\psi - \sin\phi\sin\theta\sin\psi & \sin\phi\cos\psi + \cos\phi\sin\theta\sin\psi \\ \sin\theta & -\sin\phi\cos\theta & \cos\phi\cos\theta \end{bmatrix}
$$
$$(32)$$

STA.	COORDINATES			FROM T-9B			DIST. HOR.		TANGENTS		ANGLES	
	N	E	Z	ΔN	ΔE	ΔZ*	FT.	M.	ΔN/ΔE	ΔZ/DIST*	BRG	TILT*
T-9B	865221	680506	4210 +308									
2-365 Truck I	863879	668771	4287 +3	-1342	-11735	-228	11811	3600	0.114360	-0.01930	163°18'34"	-1°-06'
7-357 Trailer II	853109	677969	4149 +3	-12112	-2537	-366	12375	3772	4.77414	-0.02958	191-49-49	0-42
7-357 6x6 III	853101	677981	4149 +3	-12120	-2525	-366	12380	3773	4.80000	-0.02966	191-46-10	0-42
372	795955	674971	4798 +3	-69266	-5535	+283	69487	21180	12.51418	+0.00407	184-34-07	+0-14
9.4a CHR's	572728	821735	8884 +4	-292493	+141229	+4370	324800	99000	-2.07105	+0.01345	154-13-36	+0-46
9.4b AM'G'A	594671	566126	2158 +4	-270560	-114380	-2356	293790	89530	2.36536	-0.008021	202-55-02	0-28
* FROM	HEIGHT	OF	BURST									

FORM E17(1-55 500)   NAME _RJB_   EDGERTON, GERMESHAUSEN & GRIER INC.

Figure 56. An example of survey data collected for Tesla [30].

1.3   Conclusion

This appendix provides the details of how the camera intrinsics and extrinsics were estimated using the available survey data and the films.

Bibliography

1. Alpaydin, Ethem. *Introduction to Machine Learning, 2nd edition.* The MIT Press, Cambridge, MA, 2010.

2. Bay, Herbert, Andreas Ess, Tinne Tuytelaars, and Luc Van Gool. "Speeded-Up Robust Features (SURF)". *Computer Vision Image Understanding*, 110(3):346–359, June 2008. ISSN 1077-3142. URL `http://dx.doi.org/10.1016/j.cviu.2007.09.014`.

3. Cleveland, William S. "Robust locally weighted regression and smoothing scatterplots". *Journal of the American Statistical Association*, 74(368):829–836, 1979.

4. Duda, R.O. and P.E. Hart. *Use of the Hough Transformation to Detect Lines and Curves in Pictures.* Technical Report 36, AI Center, SRI International, 333 Ravenswood Ave, Menlo Park, CA 94025, Apr 1971.

5. Fischler, Martin A. and Robert C. Bolles. "Random Sample Consensus: A Paradigm for Model Fitting with Applications to Image Analysis and Automated Cartography". *Communications of the ACM*, 24(6):381–395, June 1981. ISSN 0001-0782. URL `http://doi.acm.org/10.1145/358669.358692`.

6. Gladeck, F. and A. Johnson. "For the Record - A History of the Nuclear Test Personnel Review Program, 1978-1993", March 1996.

7. Harris, Chris and Mike Stephens. "A combined corner and edge detector". *In Proceedings of Fourth Alvey Vision Conference*, 147–151. 1988.

8. Hartley, Richard and Andrew Zisserman. *Multiple View Geometry in Computer Vision.* Cambridge University Press, New York, NY, USA, 2 edition, 2003. ISBN 0521540518.

9. Hartley, Richard I and Peter Sturm. "Triangulation". *Computer Vision and Image Understanding*, 68(2):146–157, 1997.

10. Hunyadi, Levente. "Fitting ellipses, ellipsoids and other quadratic curves and surfaces", 2014. Matlab File Exchange. http://www.mathworks.com/matlabcentral/fileexchange/45356-fitting-quadratic-curves-and-surfaces.

11. Jennings, Alan. "Sphere Fit (least squared)". MATLAB Central. [Online.] Available: http://www.mathworks.in/matlabcentral/fileexchange/34129-sphere-fit–least-squared- .

12. Kutulakos, Kiriakos N. and Steven M. Seitz. "A Theory of Shape by Space Carving". *International Journal Computer Vision*, 38(3):199–218, July 2000. ISSN 0920-5691. URL `http://dx.doi.org/10.1023/A:1008191222954`.

13. Le Dimet, F.-X., I. Souopgui, O. Titaud, V. Shutyaev, and M. Y. Hussaini. "Toward the assimilation of images". *Nonlinear Processes in Geophysics*, 22(1):15–32, 2015. URL `http://www.nonlin-processes-geophys.net/22/15/2015/`.

14. Liu, H. and L. Yu. "Feature Selection for High-Dimensional Data: A Fast Correlation-Based Filter Solution". *In Proceedings of The Twentieth International Conference on Machine Leaning (ICML-03)*, 856–863. ICM, Washington, D.C., 2003.

15. Lowe, David G. "Distinctive Image Features from Scale-Invariant Keypoints". *International Journal of Computer Vision*, 60(2):91–110, January 2004.

16. Lynes, David. "An analysis of methods to determine nuclear weapon yield using digital fireball films", Masters Thesis. March 2013. Air Force Institute of Technology.

17. McKinney, Joseph. "Nuclear Test Films Timing Marks", Oct 2013. Air Force Institute of Technology. Presentation.

18. Morel, Jean-Michel and Guoshen Yu. "ASIFT: A new framework for fully affine invariant image comparison". *SIAM Journal on Imaging Sciences*, 2(2):438–469, 2009.

19. Oliensis, John. "The Least-Squares Error for Structure from Infinitesimal Motion." *International Journal of Computer Vision*, 61(3):259–299, 2005. URL `http://dblp.uni-trier.de/db/journals/ijcv/ijcv61.html/Oliensis05`.

20. Pacleb, Curtis W. "Analysis of the Nuclear Thermal Pulse using Digitized Scientific Test Films", Masters Thesis. March 2013. Air Force Institute of Technology.

21. Prewitt, J.M.S. "Object Enhancement and Extraction". *Picture Processing and Psychopictorics*, 75–149. Academic Press, 1970.

22. Reinsch, Christian H. "Smoothing by spline functions". *Numerische mathematik*, 10(3):177–183, 1967.

23. Schmitt, Daniel T. and Gilbert L. Peterson. "Machine learning nuclear detonation features". *Applied Imagery Pattern Recognition Workshop (AIPR), 2014 IEEE*, 1–7. Oct 2014.

24. Schmitt, Daniel T. and Gilbert L. Peterson. "Timing mark detection on nuclear detonation video". *Applied Imagery Pattern Recognition Workshop (AIPR), 2014 IEEE*, 1–5. Oct 2014.

25. Schmitt, Daniel T. and Gilbert L. Peterson. "Feature Detection and Matching on Atmospheric Nuclear Detonation Video". *IET Computer Vision Journal*. Apr 2016. 'To appear'.

26. Schmitt, Daniel T., Gibert L. Peterson, Robert Slaughter. "Quantifying 3D Positional Uncertainty of Radiological Material From Nuclear Detonation Video". *Journal of Nuclear Science and Engineering*, 181(2).

27. Seitz, Curless B. Diebel J. Scharstein D. Szeliski R., S. M. "A comparison and evaluation of multi-view stereo reconstruction algorithms". *IEEE Computer Society Conference on Computer Vision and Pattern Recognition*, 519–526, 2006.

28. Slaughter, Robert C., John W. McClory, Daniel T. Schmitt, Matthew D. Sambora, and Karl C. Walli. "3D sparse point reconstructions of atmospheric nuclear detonations". *Applied Imagery Pattern Recognition Workshop (AIPR), 2014 IEEE*, 1–9. Oct 2014.

29. Snavely, Noah, Steven M. Seitz, and Richard Szeliski. "Photo Tourism: Exploring Photo Collections in 3D". *ACM Transactions on Graphics*, 25(3):835–846, July 2006. ISSN 0730-0301. URL `http://doi.acm.org/10.1145/1141911.1141964`.

30. Spriggs, Gregory D. "Film Scanning Project", Aug 2011. Lawrence Livermore National Laboratory. Presentation.

31. Spriggs, Gregory D. "Nuclear Weapon Effects Laboratory Class", Sept 2013. Lawrence Livermore National Laboratory. Presentation.

32. Spriggs Gregory D., Ben Kowash, Kelianne Roberts. "Fireball Yield for Bee", Sept 2014. Lawrence Livermore National Laboratory. Presentation.

33. Sun, Yijun and Jian Li. "Iterative Relief for Feature Weighting". *Proceedings of the 23rd International Conferene on Machine Learning*, 913–920, 2006.

34. Szeliski, Richard. *Computer Vision: Algorithms and Applications.* Springer-Verlag, London, 2011.

35. Szeliski, Richard and Sing Bing Kang. "Shape Ambiguities in Structure from Motion". *IEEE Transactions on Pattern Analysis and Machine Intelligence*, 19(5):506–512, May 1997. URL `http://research.microsoft.com/apps/pubs/default.aspx?id=75675`.

36. Taylor, Geoffrey. "The Formation of a Blast Wave by a Very Intense Explosion". *Proceedings of the Royal Society of London*, volume 201, 159–174. Series A, Mathematical and Physical Sciences, 1950.

37. Vedaldi, Andrea and Brian Fulkerson. "Vlfeat: An Open and Portable Library of Computer Vision Algorithms". *Proceedings of the International Conference on Multimedia*, MM '10, 1469–1472. ACM, New York, NY, USA, 2010. ISBN 978-1-60558-933-6. URL `http://doi.acm.org/10.1145/1873951.1874249`.

38. Weisstein, Eric W. "Sphere-Sphere Intersection". From MathWorld–A Wolfram Web Resource. http://mathworld.wolfram.com/Sphere-SphereIntersection.html.

39. Xie, Yonghong and Qiang Ji. "A New Efficient Ellipse Detection Method". *Internation Conference on Pattern Recognition*, 957–960. 2002.

40. Zeldovich, Y. B. *Physics of Shock Waves and High-Temperature Hydrodynamic Phenomena*. Foreign Technology Division, 1965.

REPORT DOCUMENTATION PAGE

Form Approved
OMB No. 0704–0188

1. REPORT DATE (DD–MM–YYYY)	2. REPORT TYPE	3. DATES COVERED (From — To)
24-03-2016	Dissertation	August 2013 – March 2016

4. TITLE AND SUBTITLE	5a. CONTRACT NUMBER
Position and Volume Estimation of Atmospheric Nuclear Detonations from Video Reconstruction	
	5b. GRANT NUMBER
	5c. PROGRAM ELEMENT NUMBER

6. AUTHOR(S)	5d. PROJECT NUMBER
Schmitt, Daniel T., Lt Col, USAF	16P300
	5e. TASK NUMBER
	5f. WORK UNIT NUMBER

7. PERFORMING ORGANIZATION NAME(S) AND ADDRESS(ES)	8. PERFORMING ORGANIZATION REPORT NUMBER
Air Force Institute of Technology Graduate School of Engineering and Management (AFIT/EN) 2950 Hobson Way WPAFB OH 45433-7765	AFIT-ENG-DS-16-M-254

9. SPONSORING / MONITORING AGENCY NAME(S) AND ADDRESS(ES)	10. SPONSOR/MONITOR'S ACRONYM(S)
Defense Threat Reduction Agency ATTN: Maj Andrew Decker 8725 John J Kingman Rd Stop 6201 Fort Belvoir, VA 2206-6201 andrew.w.decker.mil@mail.mil	DTRA
	11. SPONSOR/MONITOR'S REPORT NUMBER(S)

12. DISTRIBUTION / AVAILABILITY STATEMENT

DISTRIBUTION STATEMENT A: Approved for Public Release; Distribution Unlimited.

13. SUPPLEMENTARY NOTES

This material is declared a work of the U.S. Government and is not subject to copyright protection in the United States

14. ABSTRACT

Recent work in digitizing films of foundational atmospheric nuclear detonations from the 1950s provides an opportunity to perform deeper analysis on these historical tests. This work leverages multi-view geometry and computer vision techniques to provide an automated means to perform three-dimensional analysis of the blasts for several points in time. The accomplishment of this requires careful alignment of the films in time, detection of features in the images, matching of features, and multi-view reconstruction. Sub-explosion features can be detected with a 67% hit rate and 22% false alarm rate. Hotspot features can be detected with a 71.95% hit rate, 86.03% precision and a 0.015% false positive rate. Detected hotspots are matched across 57-109° viewpoints with 76.63% average correct matching by defining their location relative to the center of the explosion, rotating them to the alternative viewpoint, and matching them collectively. When 3D reconstruction is applied to the hotspot matching it completes an automated process that has been used to create 168 3D point clouds with 31.6 points per reconstruction with each point having an accuracy of 0.62 meters with 0.35, 0.24, and 0.34 meters of accuracy in the x-, y- and z-direction respectively. As a demonstration of using the point clouds for analysis, volumes are estimated and shown to be consistent with radius-based models and in some cases improve on the level of uncertainty in the yield calculation.

15. SUBJECT TERMS

Multi-view Geometry, Nuclear Detonations, Nuclear Fireballs, Nuclear Effects, 3D Reconstruction, Feature Detection, Feature Matching, Computer Vision

16. SECURITY CLASSIFICATION OF:			17. LIMITATION OF ABSTRACT	18. NUMBER OF PAGES	19a. NAME OF RESPONSIBLE PERSON Dr. Gilbert L. Peterson, AFIT/ENG
a. REPORT U	b. ABSTRACT U	c. THIS PAGE U	UU	134	19b. TELEPHONE NUMBER (Include Area Code) (937) 255-3636 x 4281; gilbert.peterson@afit.edu

Standard Form 298 (Rev. 8–98)
Prescribed by ANSI Std. Z39.18